

An Experimental Investigation of Critical Heat Flux on a  
Vertical Surface Abutting a Coarse Porous Medium



# An Experimental Investigation of Critical Heat Flux on a Vertical Surface Abutting a Coarse Porous Medium

By Justin Spencer, B.A., M.A.Sc.

A Thesis Submitted to the School of Graduate Studies in Partial Fulfillment of the Requirements for the Degree Doctor of Philosophy

## Descriptive Note

McMaster University DOCTOR OF PHILOSOPHY (2023) Hamilton, Ontario (Engineering Physics)

TITLE: An Experimental Investigation of Critical Heat Flux on a Vertical Surface Abutting a Coarse Porous Medium

## Lay Abstract

Modern nuclear power reactors are designed with robust and redundant safety features, rendering a severe accident improbable. Nevertheless, it behooves safety analysts to consider extreme scenarios, such as one in which the fuel and other contents of the reactor core collapse to the bottom of the reactor vessel. Further escalation of accident severity could be arrested in this state by retaining the core materials within the reactor vessel.

Successful retention requires efficient transport of radioactive decay heat produced by the core materials to the vessel's surroundings. In a CANDU reactor, the vessel is partly surrounded by end shield cavities filled with steel balls and water, constituting a coarse porous medium. The conditions under which heat transfer to the end shields would degrade in these locations are poorly understood.

The primary goal accomplished by this thesis is to provide safety analysts with quantification of the limits of efficient cooling in the end shield geometry, permitting improved assessments of severe accidents. Progress toward this goal constitutes a contribution to the more broadly-defined subject of externally-heated coarse porous media.



## Abstract

A postulated severe accident in a CANDU reactor may involve the collapse of core materials to the bottom of the calandria vessel. Avoidance of further degradation of the reactor state would require retention of these materials within the vessel. Successful retention depends upon transport of radioactive decay heat produced inside the vessel to its surroundings, without undue escalation of the vessel shell's temperature. Near the bottom of the vessel, this is only possible if nucleate boiling of water is maintained on the vessel's outer surfaces. The maximum heat flux removable by nucleate boiling is referred to as the Critical Heat Flux (CHF), and depends strongly on the geometry in question.

At each end of a CANDU reactor, the vertical calandria tubesheets abut an end shield cavity filled with steel shielding balls and water, constituting a coarse porous medium. Predictions of CHF in this geometry prior to the work presented in this thesis were subject to large uncertainties; an undesirable situation given the potentially significant impact of CHF on accident outcomes. The primary goal of the thesis is the quantification of CHF in this geometry, permitting improved assessments of severe accidents. Progress toward this goal constitutes a contribution to the more broadly-defined subject of externally-heated coarse porous media.

Experiments were performed, quantifying CHF and its dependence on key variables (location on the calandria tubesheet and shielding ball diameter). Investigation of potential mechanisms led to insights into the nature of the CHF phenomenon in this geometry, and its dependence on relevant variables (shielding ball thermal conductivity, and calandria tubesheet surface conditions).

Similarities to and differences from existing literature pertaining to externally-heated porous media are noted. Finally, future work is proposed, that is expected to yield a semi-mechanistic model of CHF accounting for the additional parameter of spatial heat flux variation.

The contents of this thesis represent significant progress in the understanding of CHF on the surface of a calandria tubesheet facing the end shield cavity, and more generally, externally-heated coarse porous media.

## Acknowledgements

I would like to thank the dozens of people who, either directly or indirectly, helped me complete this thesis.

## Table of Contents

Descriptive Note .....	ii
Lay Abstract.....	iii
Abstract.....	v
Acknowledgements.....	vi
List of Figures .....	x
List of Tables .....	xi
List of Abbreviations and Symbols.....	xii
Declaration of Academic Achievement.....	xv
1. Introduction .....	16
1.1. CANDU Nuclear Reactors.....	16
1.2. Severe Accidents.....	18
1.2.1. Severe Accident Progression in a CANDU Reactor .....	19
1.2.2. In Vessel Retention .....	24
1.3. Objectives.....	28
1.4. General Notes .....	29
2. Literature Review and Background.....	30
2.1. Pool Boiling .....	30
2.1.1. Horizontal Surfaces .....	33
2.1.2. Vertical Surfaces.....	37
2.1.3. Porous Media .....	41
2.2. Single-Phase Flow .....	42
2.2.1. Single-Phase Flow in Pipes and over Flat Surfaces .....	42
2.2.2. Single-Phase Flow in Porous Media .....	45
2.3. Two-Phase Adiabatic Flow .....	47
2.3.1. Two-Phase Flow in Pipes and over Flat Surfaces .....	47
2.3.2. Two-Phase Flow in Porous Media.....	48
2.3.3. Two-Phase Flow in Minichannels.....	49
2.4. Two-Phase Boiling Flow .....	49
2.4.1. Two-Phase Boiling Flow in Pipes and over Flat Surfaces .....	49
2.4.2. Two-Phase Boiling Flow over Obstructions .....	50
2.4.3. Two-Phase Boiling Flow in Internally-Heated Porous Media.....	50
3. Experimental and Analytical Methods.....	51

3.1.	Heated Experiments.....	51
3.1.1.	Heating Plate.....	52
3.1.2.	Secondary Design Features.....	53
3.1.3.	Instrumentation .....	54
3.1.4.	Experimental Procedure .....	55
3.1.5.	Repeatability of Results .....	55
3.2.	Air Barbotage .....	56
4.	Measurement of Critical Heat Flux in a CANDU End Shield Consisting of a Vertical Surface Abutting a Packed Bed of Steel Shielding Balls.....	58
4.1.	Preface .....	58
4.1.1.	Citation.....	58
4.1.2.	Contribution to Knowledge.....	58
4.1.3.	Author’s Contribution to Paper .....	59
4.2.	Publication .....	60
4.2.1.	Abstract.....	60
4.2.2.	Nomenclature .....	60
4.2.3.	Introduction .....	61
4.2.4.	Pre-Existing Knowledge Base .....	62
4.2.5.	Experimental Apparatus and Procedure.....	64
4.2.6.	Results.....	66
4.2.7.	Summary .....	68
4.2.8.	References .....	68
4.2.9.	List of Figures .....	71
4.2.10.	List of Tables.....	77
5.	Results of Air Barbotage Experiments Simulating Two-Phase Flow in a CANDU End Shield during In-Vessel Retention .....	80
5.1.	Preface .....	80
5.1.1.	Citation.....	80
5.1.2.	Contribution to Knowledge.....	80
5.1.3.	Author’s Contribution to Paper .....	81
5.2.	Publication .....	82
5.2.1.	Abstract.....	82
5.2.2.	Introduction .....	82
5.2.3.	Background .....	83

5.2.4.	Experimental Apparatus and Procedure.....	84
5.2.5.	Results.....	86
5.2.6.	Discussion.....	88
5.2.7.	Summary.....	89
5.2.8.	Nomenclature.....	90
5.2.9.	References.....	90
5.2.10.	List of Figures.....	92
6.	Critical Heat Flux in a CANDU End Shield – Influence of Shielding Ball Diameter.....	100
6.1.	Preface.....	100
6.1.1.	Citation.....	100
6.1.2.	Contribution to Knowledge.....	100
6.1.3.	Author’s Contribution to Paper.....	101
6.2.	Publication.....	102
6.2.1.	Abstract.....	102
6.2.2.	Introduction.....	102
6.2.3.	Literature.....	103
6.2.4.	Experimental Apparatus and Procedure.....	104
6.2.5.	Results.....	106
6.2.6.	Discussion.....	109
6.2.7.	Summary.....	112
6.2.8.	Nomenclature.....	112
6.2.9.	References.....	114
6.2.10.	Figures.....	115
7.	Conclusions.....	123
7.1.	Summary of Work and Contributions to Knowledge.....	123
7.2.	Recommendations for Safety Analysis.....	126
7.3.	Recommendations for Future Work.....	127
8.	Works Cited.....	130

## List of Figures

Figure 1. Schematic of CANDU Reactor Core under Normal Operating Conditions (L – Section View from Side, R – Section View from End) .....	17
Figure 2. Schematic of CANDU Reactor Core during Moderator Depletion (L – Section View from Side, R – Section View from End).....	22
Figure 3. Schematic of CANDU Reactor Core during Core Collapse (L – Section View from Side, R – Section View from End).....	23
Figure 4. Schematic of CANDU Reactor Core during In Vessel Retention Core Damage State (L – Section View from Side, R – Section View from End) .....	24
Figure 5. Schematic One-Dimensional Representation of Temperature Field and Exiting Heat Flux at Calandria Tubesheet during IVR.....	27
Figure 6. Pool Boiling Curve Schematic.....	31
Figure 7. Schematic of Void Fraction Profile for Boiling of Saturated Water at 1 Bar [29] .....	32
Figure 8. Schematic of Hydrodynamic Theory of Critical Heat Flux.....	34
Figure 9. Schematic of Vapour Cutback Mechanism [43] .....	37
Figure 10. Wetting Front Propagation along Vertical Heated Surface [45] .....	38
Figure 11. Representative Velocity Profiles for Forced Flow in a Round Pipe.....	43

## List of Tables

Table 1. Barriers to Fission Product Release.....	18
Table 2. Severe Accidents in Power Reactors.....	19
Table 3. Sequence of Key Events during an Unmitigated CANDU Station Blackout.....	20
Table 4. Conditions Necessary to the Success of In Vessel Retention.....	25
Table 5. Subordinate Objectives of Research Presented in this Thesis.....	28

## List of Abbreviations and Symbols

### Latin Script

A''	Volumetric air flux
AECL	Atomic Energy of Canada Limited
Bo	Bond number
Bq	Becquerel
BWR	Boiling Water Reactor
C	Constant
CANDU	CANada Deuterium Uranium
CNL	Canadian Nuclear Laboratories
CV	Calandria Vessel
d	Diameter
FP	Fission Product
g	Gravity
h	Heat transfer coefficient
$h_g$	Latent heat of vaporization
IAEA	International Atomic Energy Agency
INES	International Nuclear and radiological Event Scale
IVR	In-Vessel Retention
Ja	Jakob number
k	Thermal conductivity
K	Absolute permeability
Ku	Kutateladze number
L	Length or height of heated surface
MAAP	Modular Accident Analysis Program
MCCI	Molten Corium Concrete Interaction
n	Exponent
NAMS	Nuclear Accident Magnitude Scale
Nu	Nusselt number

Oh	Ohnesorge number
PIRT	Phenomena Identification and Ranking Table
Pr	Prandtl number
PWR	Pressurized Water Reactor
R	Off-site atmospheric release of radioactivity / Radius
Ra	Rayleigh number
RBMK	Reaktor Bolshoy Moshchnosti Kanalnyy <sup>1</sup>
q	Thermal power
q''	Heat flux
Sh	Sherwood number
T	Temperature
TBq	Terabecquerel
TDB	Terminal Debris Bed
v	Specific volume of water
x,y,z	Spatial variables in a Cartesian coordinate system

*Subscripts*

c	Condensate
e	Electrical / excess
eff	Effective
f	Fluid
g	Gas
l	Liquid
sat	Saturation
s,f	Surface, fluid
th	Thermal
v	Vapour
w	Wall

---

<sup>1</sup> The English translation of Reaktor Bolshoy Moshchnosti Kanalnyy (Russian) is 'high-power channel-type reactor'.

1,2,3 Unique identifiers of constants

**Greek Script**

$\alpha$  Thermal diffusivity

$\varepsilon$  Porosity

$\lambda$  Wavelength

$\mu$  Dynamic viscosity

$\nu$  Kinematic viscosity

$\rho$  Density

$\sigma$  Surface tension

## Declaration of Academic Achievement

The primary supervisor of the author is Dr. David Novog. The author's supervisory committee includes three other members: Dr. Thambiayah Nitheanandan, Dr. John Luxat, and Dr. Nikola Popov. The experimental research presented in the thesis was carried out at Atomic Energy of Canada Limited (AECL) and Canadian Nuclear Laboratories (CNL) under the direct supervision of Dr. Nitheanandan.

The author led all of the work presented in this sandwich thesis from conception through execution, analysis, and publication, and performed the large majority of the work himself. Secondary contributions were made by various manufacturers, as well as colleagues at AECL and CNL. The most significant of these contributions were the manufacturing and assembly of components. Specific discussion of the contributions of others is included in the preambles to the results sections.

## 1. Introduction

Plentiful, affordable energy is crucial to the function of modern societies. Its availability is a necessary condition for the emancipation of humanity from excessive physical labour, and increases the standard of living accessible to society. Since the industrial revolution, the primary source of energy for much of the world has been fossil fuels, including coal, petroleum, and natural gas. Challenges have emerged to the continued use of energy generation systems dominated by fossil fuels, by factors such as increased global energy demands, finite sources of fossil fuels, and environmental considerations [1].

Nuclear power constitutes a non-fossil fuel source of energy [2]. Nuclear reactors feature several advantages over non-fossil alternatives, including stability of supply, a high power output in comparison to its footprint, and a favourable ratio of electrical output to lifecycle CO<sub>2</sub> emissions. Canada's most populous province (Ontario) benefits from an electrical grid that has received more than half of its electrical power from CANada Deuterium Uranium (CANDU) reactors since 2004 [3]. Aspirations for increased adoption of nuclear power are widespread, and include the World Nuclear Association's Harmony initiative, which targets tripling of 2015 nuclear generation by 2050, resulting in 25% of global electricity supplied [4].

The prospect of such broad implementation of nuclear power generation augments the importance of robust safety performance of the reactors, in both probable and improbable scenarios. The motivation of the research presented in this thesis is to improve understanding of a phenomenon of potential importance to the outcome of a postulated severe accident in a CANDU reactor. The advancement in the knowledge base presented by this research equips safety analysts with an improved ability to predict accident progression. Predictions of accident progression permit optimization of: the design of future reactors, actions taken by reactor operators during an accident to mitigate its severity, and actions taken offsite during a nuclear emergency to minimize public harm. More generally, the results presented constitute an extension of the knowledge base pertaining to externally-heated coarse porous media.

### 1.1. CANDU Nuclear Reactors

On September 5, 1945, the Zero-Energy Experimental Pile (ZEEP), located at Chalk River Laboratories, became the first reactor in Canada (and the first outside of the United States) to reach criticality. Amongst other applications, ZEEP permitted investigation of the characteristics of lattices composed of uranium in heavy water. The National Research Experimental (NRX) reactor, subsequently began operation in 1947. NRX exhibited many of the key elements of modern CANDU reactors, most notably a heavy water moderator and a fuel channel arrangement. The design of a significantly more advanced version of NRX was begun in 1949. The resulting National Research Universal (NRU) reactor began operation in 1957, and demonstrated additional features of CANDU reactors, including online refuelling and heavy water coolant (in addition to a heavy water moderator).

Canada's development of reactors used for electrical production began in earnest with the Nuclear Power Demonstration (NPD) reactor, which began operation in 1962 [5]. This was followed by the Douglas Point reactor, which was a larger-scale version of NPD (200 MW<sub>e</sub>, rather than NPD's 22 MW<sub>e</sub>), beginning operation in 1967. Following this developmental period, 22 CANDU reactors were commissioned in Canada between 1971 and 1993, with net power production ranging 515 MW<sub>e</sub>.

(Pickering A) and 822 MW<sub>e</sub> (Bruce B). Two of these reactors were of the CANDU 6 design, with net power output of 635 MW<sub>e</sub> (Point Lepreau and Gentilly-2). Internationally, nine CANDU-6 reactors were sold in Argentina, China, Romania, and South Korea, with the first beginning operation in 1984 (Embalse 1 in Argentina), and the last in 2007 (Cernavoda 2 in Romania).

Given the prevalence of the CANDU 6 design, its features are used as the default reference point throughout this thesis. A schematic of the reactor core is shown in Figure 1.

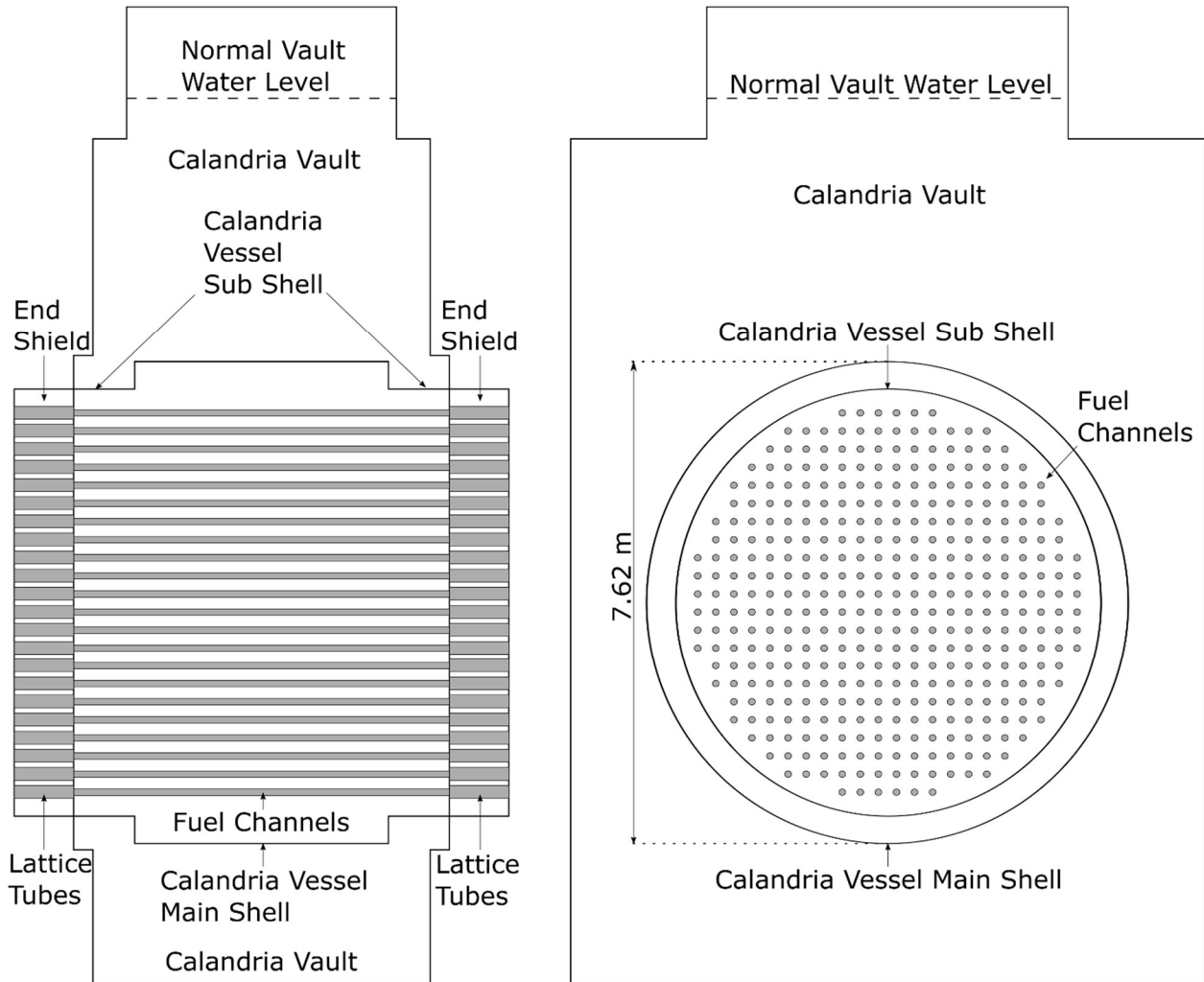


Figure 1. Schematic of CANDU Reactor Core under Normal Operating Conditions (L – Section View from Side, R – Section View from End)

The fuel used in CANDU reactors is natural uranium oxide (UO<sub>2</sub>), which has been sintered into ceramic pellets. These pellets are encapsulated in a metallic Zircaloy-4 (a zirconium alloy) sheath, to form a fuel element. Fuel elements (37 in CANDU 6) are structured into fuel bundles approximately 0.5 m in length. Fuel bundles are positioned within fuel channels (6 m long), which are composed of a pressure tube (zirconium niobium alloy, Zr-2.5% Nb) and a calandria tube (Zircaloy-2), separated by an annulus filled by gas and garter springs. The pressure tubes are filled with heavy water primary heat transport system (PHTS) coolant that is pumped over the fuel. The calandria tubes are surrounded by a heavy water moderator, which (aside from a small volume of cover gas) fills the stainless steel 304L calandria vessel.

The calandria vessel is surrounded radially by the calandria vault (or shield tank), which is filled with light water. The ends of the calandria vessel are enclosed by the stainless steel 304L calandria tubesheet. The outer surface of the calandria tubesheet abuts the end shield. Given that fuelling operations must take place via the end fittings that pass through the end shields, the end shield thickness is restricted to the point where light water alone would provide insufficient attenuation of gamma rays produced within the reactor core. Consequently, the end shield is filled with a packed bed of roughly-spherical carbon steel shielding balls, and light water.

## 1.2. Severe Accidents

The operation of nuclear reactors results in the production of a wide array of radionuclides. Most notable where the consequences of accidents are concerned are the atomic fragments produced through nuclear fission of heavy nuclei, referred to as fission products (FPs). The greatest impacts of potential accidents in reactors result from the release of radioactive FPs, which can adversely affect both people and the environment.

In a CANDU reactor, the large majority of the FPs remain within the fuel pellet ceramic under normal operating conditions. The five barriers to FP release are listed in Table 1.

Table 1. Barriers to Fission Product Release

	<b>Barrier to FP Release</b>	<b>Characterization</b>
<b>1</b>	Fuel pellet matrix	FP Retention
<b>2</b>	Fuel sheath	FP Containment
<b>3</b>	Heat transport system pressure boundary	FP Containment
<b>4</b>	Containment envelope	FP Containment
<b>5</b>	Site exclusion boundary	FP Dilution

Characterization of the magnitude of events with potential radiological implications simplifies communication of their severity. Perhaps the most commonly cited approach to this is the International Atomic Energy Agency's (IAEA's) International Nuclear and Radiological Event Scale (INES) [6]. This scale involves seven levels spread on a roughly logarithmic scale, with the severity of each level separated by approximately a factor of 10 (although quantification is complicated through the use of multiple contributing factors). Levels 1-3 referred to as 'incidents', while levels 4-7 are considered 'accidents'.

The Nuclear Accident Magnitude (NAMS) scale [7] was proposed in 2011 as an alternative to INES, intended to address its perceived deficiencies. NAMS represents the severity of a nuclear accident on a continuous scale (rather than the discrete representation used in INES), calculated as the logarithm of the atmospheric radioactive release<sup>2</sup>. It is noteworthy that releases to bodies of water are not accounted for by NAMS.

The term 'severe accident' is defined as one that involves a gross loss of core geometry. These are typically considered to have a low frequency, and would be classified as at least INES level 5. The radiological releases, and hence the classification on NAMS could vary widely, depending on the nature

---

<sup>2</sup> Specifically, the accident magnitude is calculated as  $\log(20R)$ , where  $R$  is the off-site atmospheric release of radioactivity, normalized to equivalent I-131 in units of TBq.

of the accident and factors such as the performance of the reactor containment. Events classified as severe accidents in power reactors are summarized in Table 2.

Table 2. Severe Accidents in Power Reactors

Facility Name	Reactor Type	Date	INES Classification [6]	NAMS Classification [7]
Three Mile Island Unit 2	Pressurized Water Reactor (PWR)	March 28, 1979	5	7.9
Chernobyl Unit 4	Reaktor Bolshoy Moshchnosti Kanalnyy (RBMK)	April 26, 1986	7	8
Fukushima Daiichi Units 1-4	Boiling Water Reactor (BWR)	March 11, 2011	7	7.5

In a CANDU reactor, a severe accident is considered to be a beyond design basis accident (BDDBA), and would involve the widespread disassembly of fuel channels within the calandria vessel. The CANDU fleet operating record is free of such events, and the probability of one in the future is very low; however, the possibility cannot be entirely discounted.

A widely-held notion in nuclear safety is that the safe operation of a reactor can be assured through the maintenance of the following basic safety functions:

1. Reactivity control,
2. Cooling of the fuel, and
3. Confinement of radioactive material.

A modern approach to reactor safety includes application of the concept of defence in depth [6] to each of these basic safety functions, through a combination of design conservatism, quality assurance, surveillance, mitigation measures, and safety culture. Defence in depth can also be viewed from the perspective of the number of systems that must fail in order for an undesirable outcome (e.g. the release of radioactive material to the environment) to occur. In this sense, the five barriers to FP release can be considered an example of defence in depth.

### 1.2.1. Severe Accident Progression in a CANDU Reactor

This section includes a description of the widely-held understanding of the progression of an unmitigated severe accident in a CANDU reactor from initiating event to final state [8][9][10][11], aligned with the position espoused by reactor operators. This progression is influenced by numerous coupled phenomena, many of which are subject to considerable uncertainties. Given this situation, some criticism of the dominant understanding of CANDU severe accidents has been expressed, and alternate predictions of the accident progression have been presented [12][13].

The most significant events occurring during an accident sequence described as a station blackout (SBO) are outlined in Table 3, with the timing of events specific to a CANDU-6 reactor [9]. Throughout this sequence, opportunities for mitigating actions are available to the reactor’s operators; however, it is assumed that no such actions are taken.

Table 3. Sequence of Key Events during an Unmitigated CANDU Station Blackout

Time (h) [9]	Event	Notes
0	Loss of electrical power	<ul style="list-style-type: none"> <li>Reactor automatic trip is initiated, and reactor is subcritical</li> <li>Following rundown of PHTS pumps, natural circulation of PHTS is established, with heat transferred primarily to the secondary side of the steam generators.</li> </ul>
1.8	PHTS liquid relief valves (LRVs) open	<ul style="list-style-type: none"> <li>This occurs as a result of pressurization of the PHTS.</li> </ul>
1.9	Secondary side of steam generators is dry	<ul style="list-style-type: none"> <li>Vaporization of the PHTS inventory becomes the primary heat sink.</li> <li>PHTS inventory loss through LRVs accelerates.</li> </ul>
3.9	At least one fuel channel is dry	<ul style="list-style-type: none"> <li>Temperature of fuel and pressure tube (PT) increase quickly.</li> </ul>
3.9	PT and calandria tube (CT) of one channel rupture	<ul style="list-style-type: none"> <li>PHTS vapour is expelled into the calandria vessel (CV), where it contacts subcooled moderator and condenses.</li> </ul>
4.0	Moderator reaches saturation temperature	<ul style="list-style-type: none"> <li>Vaporization of the moderator becomes the primary heat sink.</li> </ul>
4.0	CV rupture discs open	<ul style="list-style-type: none"> <li>Blowdown of vapour and entrained liquid moderator begins.</li> </ul>
4.3	Calandria vault rupture discs open	
5.5	Beginning of core disassembly	<ul style="list-style-type: none"> <li>As the moderator level falls, CTs not surrounded by liquid moderator heat up, soften, and collapse onto underlying cooled channels (see Figure 2).</li> <li>It is anticipated that the time required for a dry CT to collapse would bear an inverse relationship with channel power during operation (hence decay heat). Low power channels at the CV periphery may remain intact for an extended period after the collapse of high power channels in the same row.</li> <li>Most debris is anticipated to remain in large pieces; however, some smaller pieces would fall to the bottom of the CV.</li> <li>Suspended debris reaches high temperatures, releasing a significant fraction of FP inventory that is transported through the CV relief ducts to containment.</li> <li>Rising vapour reacts exothermically with suspended debris (particularly Zr), releasing flammable D2 gas.</li> </ul>
Variable	Massive core debris relocation to CV bottom	<ul style="list-style-type: none"> <li>As core disassembly progresses, increasingly large masses of suspended debris accumulate. When the strength of the supporting channels is exceeded ([14][15]), the debris collapses to the bottom of the vessel to form a terminal debris bed (TDB).</li> </ul>

Time (h) [9]	Event	Notes
		<ul style="list-style-type: none"> <li>It is anticipated that this would occur in a column by column fashion, starting near the centre of the core and progressing outward to the periphery (see Figure 3).</li> <li>A significant fraction of the material relocating to the bottom of the CV during collapse is anticipated to be solid. Molten material relocated to the bottom would likely solidify, as a result of heat transfer to the residual liquid-phase moderator.</li> </ul>
11.0	Moderator entirely depleted	<ul style="list-style-type: none"> <li>Cessation of D2 gas production and FP transport from the TDB.</li> <li>TDB enthalpy increases, and heat transfer through the CV shell to the calandria vault and end shields accelerates.</li> <li>Eventually, the TDB reaches a quasi-steady state, forming a partially molten pool surrounded by a solid crust (see Figure 4). The maintenance of this state is referred to as in vessel retention (IVR).</li> <li>It is possible that some peripheral channels and/or ‘channel stubs’ may remain suspended above the top of the TDB; however, in the interest of simplicity, these are not depicted in Figure 4.</li> </ul>
14	Water in calandria vault reaches saturation temperature	<ul style="list-style-type: none"> <li>Vaporization of the water in the calandria vault and end shield is now the primary heat sink.</li> </ul>
46	Calandria vessel failure	<ul style="list-style-type: none"> <li>This table is informed by the prediction that IVR can be maintained until the calandria vault inventory falls to the elevation of the top of the corium pool.</li> <li>Once the vessel fails, a significant fraction of the corium would fall to the bottom of the calandria vault.</li> <li>Ex-vessel phenomena occurring at this point have large uncertainties, and would include: melt fragmentation, quenching, steam explosions, and melt spreading.</li> <li>Vessel failure would result in commencement of chemical reactions between corium and water vapour producing flammable H2 gas. The release of FPs and their transport to containment would also be significant.</li> </ul>
53	Water is depleted inside calandria vault	
56	Molten corium-concrete interaction (MCCI) begins in calandria vault	<ul style="list-style-type: none"> <li>MCCI, and the interaction of the resulting gasses with corium would lead to the release of significant quantities of flammable H2 and CO gasses to containment. The release of FPs and their transport to containment would continue.</li> </ul>
120	Calandria vault floor fails due to concrete ablation	

The final four rows of Table 3 would only occur if the CV fails, and IVR is lost. The addition of water to the calandria vault presents the possibility of extending IVR indefinitely, provided that all other conditions for IVR are satisfied (see Section 1.2.2).

The set of event sequences leading to severe core damage includes alternatives to the SBO sequence; however, the SBO sequence is reasonably representative of this set where the focus of this thesis is concerned, in that the majority of event sequences would reach an IVR configuration such as that shown in Figure 4.

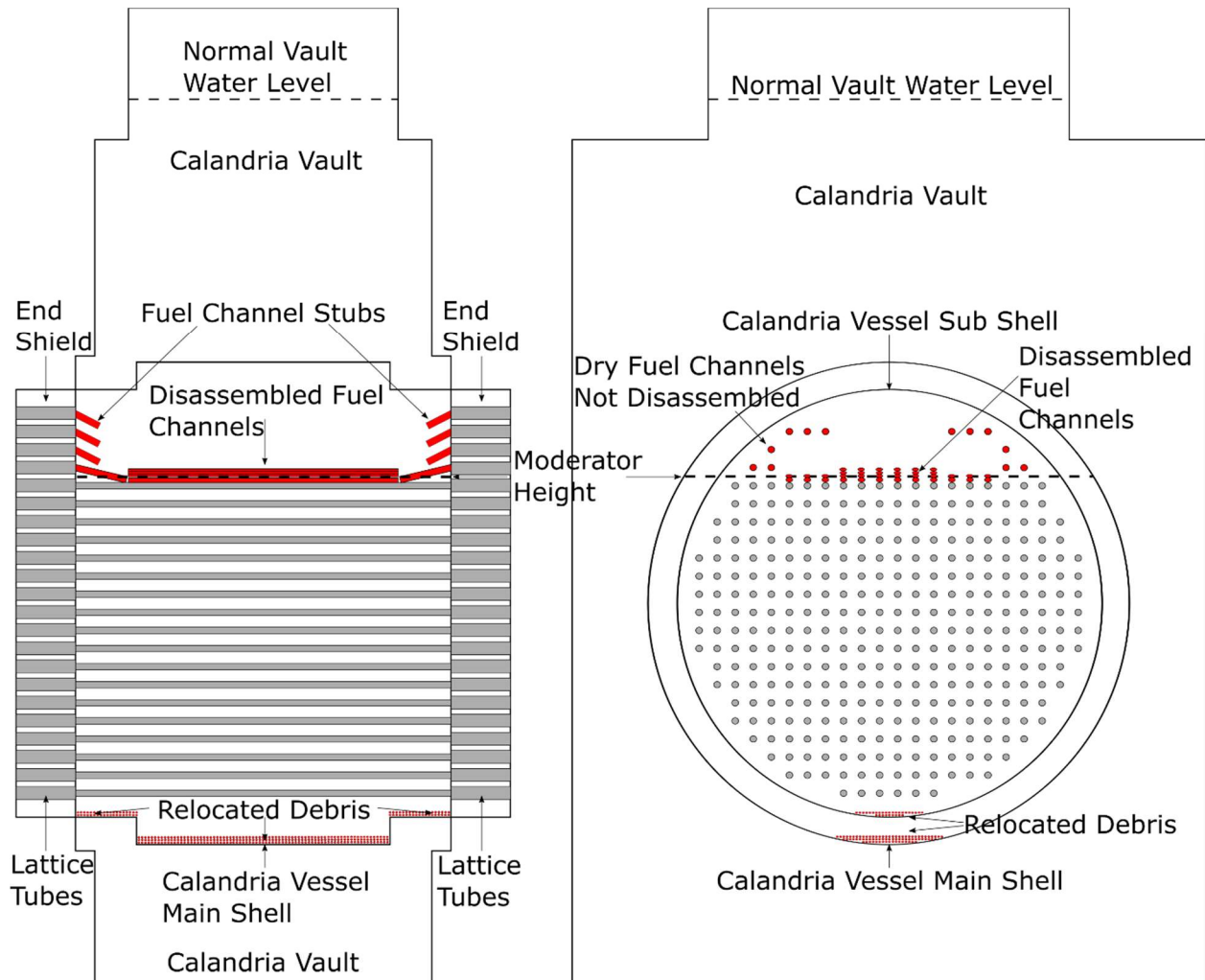


Figure 2. Stylized Representation of a CANDU Reactor Core during Moderator Depletion (L – Section View from Side, R – Section View from End)

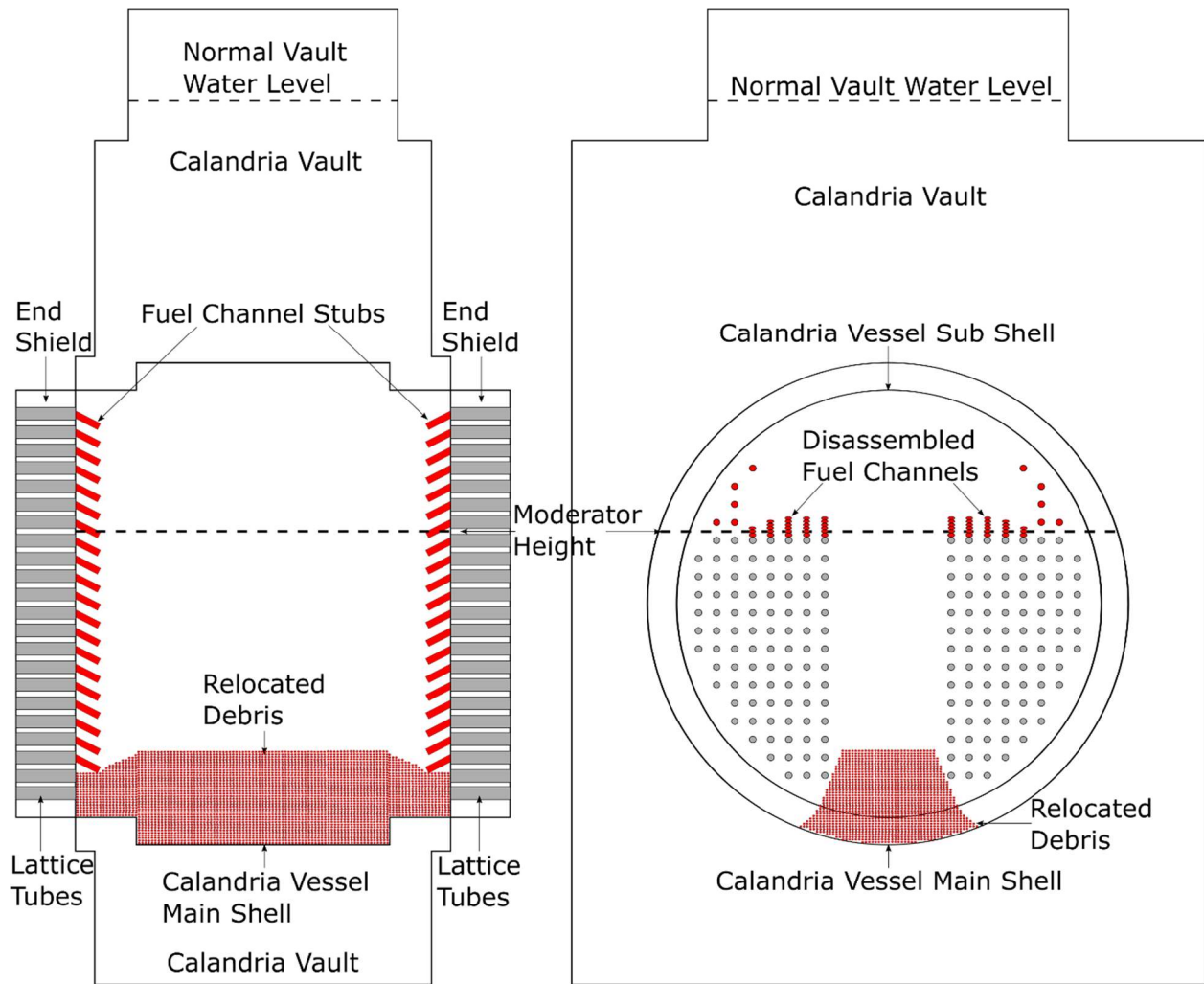


Figure 3. Stylized Representation of a CANDU Reactor Core during Core Collapse (L – Section View from Side, R – Section View from End)

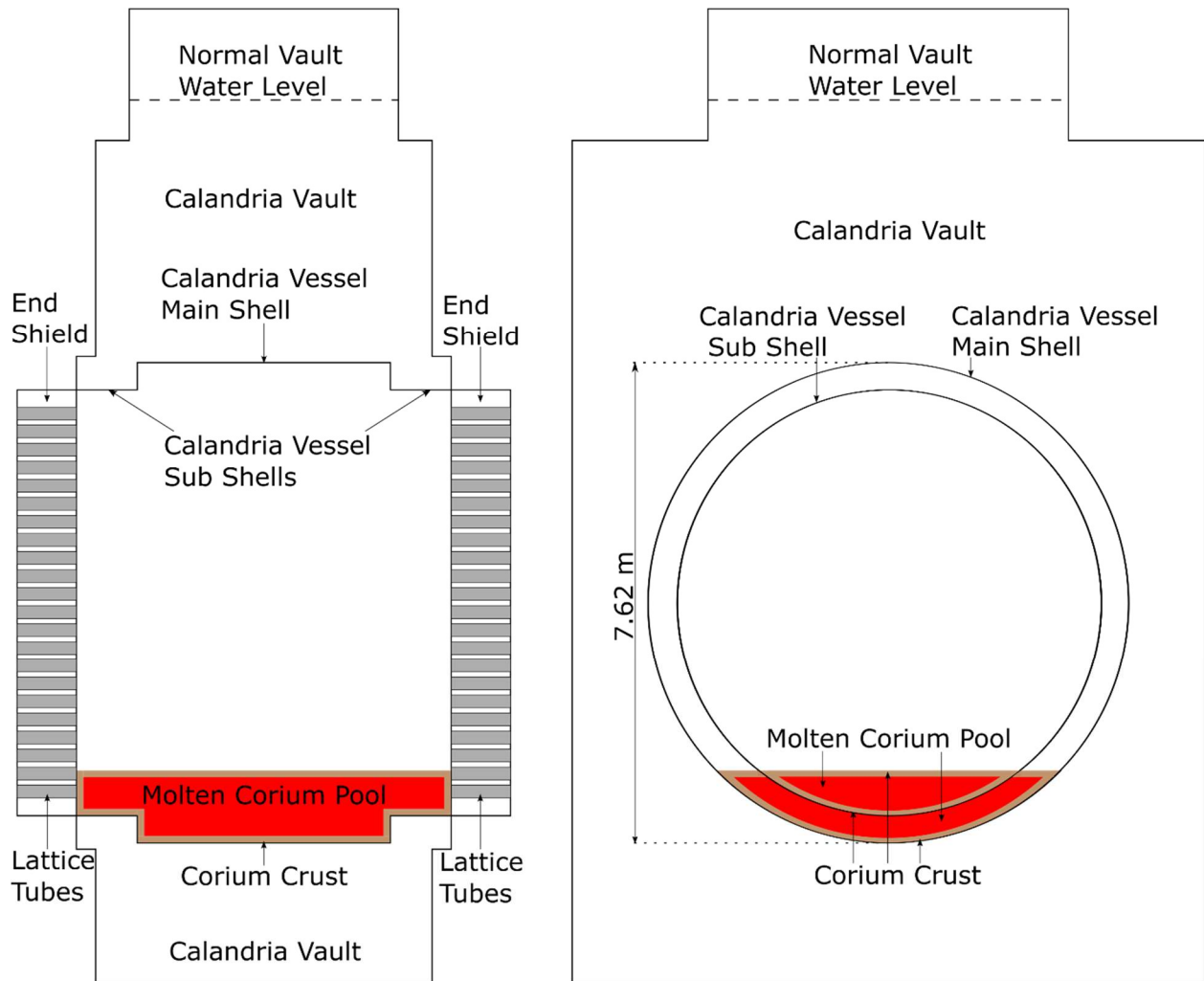


Figure 4. Stylized Representation of a CANDU Reactor Core during In Vessel Retention Core Damage State (L – Section View from Side, R – Section View from End)

### 1.2.2. In Vessel Retention

The concept of IVR was first applied to a power reactor licensing exercise with the two 507 MW<sub>e</sub> PWRs comprising the Loviisa nuclear power plant in Finland [16][17]. IVR presents an opportunity to avoid high-uncertainty ex-vessel phenomena such as ex-vessel steam explosions and MCCI.

As described in Table 3 and shown in Figure 4, IVR in a CANDU reactor is a state in which the core materials have largely relocated to the bottom of the CV. The success of IVR depends upon several conditions, summarized in Table 4. The items listed in this table that are most relevant to this thesis are the exiting heat flux, and the critical heat flux.

Table 4. Conditions Necessary to the Success of In Vessel Retention

Condition	Key Subordinate Factors	Description
<p>The CV must be capable of withstanding both dynamic and static mechanical loads, as well as thermally-induced stresses</p>	<p>Dead weight load</p>	<p>The dead weight load during IVR is the difference between the buoyant forces acting on the vessel from the surrounding calandria vault, and the weight of the corium. Provided that vessel wall temperatures do not increase significantly, this is not considered a challenge to vessel wall integrity [18].</p>
	<p>Sustained overpressure</p>	<p>Sustained pressurization of the vessel can, in principle, threaten its integrity before the moderator is entirely depleted; however, rupture discs provide pressure relief below the safe limits of the vessel.</p>
	<p>Local stress discontinuities</p>	<p>Local stress discontinuities at nozzle attachments or penetration locations are possible, but are anticipated to be below the threshold at which they would threaten IVR [18].</p>
	<p>Transient pressurization</p>	<p>Transient pressurization of the vessel can, in principle, threaten its integrity following either PHTS discharge into the CV, or collapse of hot core material into the moderator; however, the capacity of the four relief ducts is considered to be sufficient to keep the maximum transient pressure below the design limits of the CV [18].</p>
	<p>Impulsive loading</p>	<p>Impulsive loading of the CV could occur as a result of either core collapse, or else pressure waves generated following the in-core rupture of one or more fuel channels. Neither of these presents a plausible threat to exceedance of the CV shell's integrity [18].</p>
	<p>Thermally-induced stresses</p>	<p>Stresses resulting from temperature gradients could in principle threaten CV integrity; however, the magnitude of these temperature gradients are not considered sufficient to threaten the CV shell's integrity [18].</p>
<p>The CV shell must not be subject to significant loss of thickness through melting or ablation</p>	<p>Exiting heat flux</p>	<p>Heat flux exiting the CV shell will vary spatially as a result of factors including corium convection [19][20][21], vessel and crust geometry [22][23], heat transfer coefficients from all surfaces of the corium pool to the CV shell (including radiative</p>

Condition	Key Subordinate Factors	Description
		heat transfer from the upper surface), and boundary conditions at the outer surfaces of the shell [24][25].
	Critical heat flux	The CHF will vary as a function of position around the periphery of the CV shell, as a function of factors including surface orientation, local hydrodynamic conditions during IVR, surface geometry (e.g. proximity to vessel penetration or welds), and the presence or absence of shielding balls (i.e. end shields vs. calandria vault). If the CHF is exceeded by the exiting heat flux, it is anticipated that vessel failure would follow relatively quickly.
	Corium miscibility	The separation of corium into metallic and oxidic components has the potential to lead to local escalations in exiting heat flux, as well as reduction in the temperatures at which ablation rates would become significant.
	CV shell – corium interface temperature and resulting ablation rates	The most important factor in determining the temperature at the interface between the CV shell and the corium crust is the outer boundary condition. If nucleate boiling is maintained (i.e. if the exiting heat flux is less than the CHF), the interface temperature will be below the temperature at which significant ablation would be anticipated.
Corium must not exit the vessel through penetrations near the bottom of the CV (end fittings, moderator outlets, calandria drainline)	Corium crust thickness and strength	A crust bridging the openings to the penetrations near the bottom of the vessel may be capable of resisting the hydrostatic pressure of the molten corium pool, precluding flow of the corium into the penetration.
	Freezing plug formation in penetrations	If a crust bridging the penetration openings is not sufficient to avoid flow of corium, a frozen plug may form in the vessel penetration, precluding excessive corium relocation [26].

Throughout this thesis, the term exiting heat flux (alternatively – heat efflux) is used to refer to the heat transported from the CV shell to the calandria vault or end shield cavity. The exiting heat flux, along with the temperature field, in the vicinity of the calandria tubesheet is shown in Figure 5. Heat flux is proportional to the temperature gradient, as shown in equation 1 (Fourier’s Law).

$$q'' = -k\nabla T \quad (1)$$

Where  $q''$  is the heat flux,  $k$  is thermal conductivity, and  $T$  is the temperature field. In one dimension, Equation 1 can be simplified to equation 2.

$$q'' = -k \frac{dT}{dx} \quad (2)$$

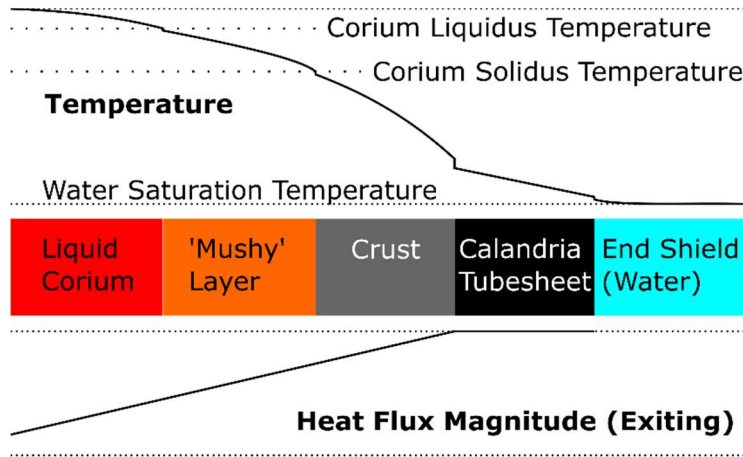


Figure 5. Schematic One-Dimensional Representation of Temperature Field and Exiting Heat Flux at Calandria Tubesheet during IVR

As shown in Figure 5, the heat flux would be expected to increase in the regions in which decay heat is generated. Assuming that the volumetric heat generation is uniform, and ignoring convection, the heat flux would increase linearly in this one dimensional system. As implied by Equation 2, the temperature profile in regions where no heat is generated would be linear, while the profile in regions where heat generation is non-zero would be parabolic in nature (provided that both the volumetric heat generation and the thermal conductivity are uniform). At the junctions between different materials, a step change in temperature would be expected, with magnitude equal to the heat flux divided by the heat transfer coefficient characteristic of that junction. Finally, one of the properties of the multi-component corium is that it lacks a single well-defined melting point. Above the liquidus temperature it is liquid, below the solidus temperature it is solid, and between the two a mixture of the two phases is present, yielding a 'mushy' layer.

The research presented in this thesis was motivated in large part by a phenomena ranking and identification table (PIRT) exercise that found CHF in the end shield to be a phenomenon with both high importance and a high uncertainty [11]. As outlined in Table 4, if the exiting heat flux exceeds the CHF at any location on the CV shell, a temperature escalation would be anticipated, with a magnitude sufficient to cause a loss of vessel integrity and IVR. Prior to publication of the research presented in this thesis, the ability of safety analysts to predict CHF on the surface of the calandria tubesheet facing the end shield cavity was limited. As a concrete example, the most widely used computer code for analysis of severe accidents in CANDU reactors is Modular Accident Analysis Program (MAAP)-CANDU.

In defining the CHF in the end shield, users of this code may select from three options, none of which represent a geometry resembling the end shield<sup>3</sup>.

### 1.3. Objectives

As discussed in Section 1.2.2, one of the conditions of successful IVR is that the heat flux exiting the calandria tubesheet surface facing the end shield cavity must not exceed the local value of CHF. Prior to publication of the papers contained in this thesis, a PIRT exercise found CHF at this location to be a phenomenon with both high importance and a high uncertainty [11]. This undesirable situation motivated the overarching objective of the research presented in this thesis: the generation of a model of critical heat flux on the surface of a calandria tubesheet facing the end shield cavity during IVR in a CANDU reactor, having the following characteristics:

1. Predictive ability across the range of all parameters relevant to the reactor scenario;
2. Empirical validation across a range of experimental data;
3. Identified and explained differences and similarities to knowledge base applicable to similar systems; and
4. To the extent practicable, formulation from well-established physical laws (i.e. a mechanistic model).

Progress toward this objective can be approached through a series of subordinate objectives. These objectives are summarized in Table 5.

Table 5. Subordinate Objectives of Research Presented in this Thesis

	Objectives		Questions to be Answered	Progress
<b>A</b>	Quantify the CHF, and its dependence on key variables.	<b>1</b>	Does elevation (or heating surface height) affect the CHF, when the heat flux (Figure 5) is uniform? If so, how?	See Section 4
		<b>2</b>	Does the condition of the heating surface affect the CHF? If so, how?	See Sections 4 and 6
		<b>3</b>	Does the diameter of the shielding balls affect the CHF? If so, how?	See Section 6
		<b>4</b>	How does CHF vary with local hydrodynamic conditions?	Future work (data presented in Sections 4 and 6 will form part of the solution)
<b>B</b>	Hydrodynamic characterization of the end shield cavity	<b>5</b>	How do vapour and liquid migrate through the porous medium (e.g. is a countercurrent flooding limit relevant to the reactor case)?	See Section 5
		<b>6</b>	How do near-wall hydrodynamic conditions vary as a function of relevant parameters (exiting heat flux distribution, shielding ball diameter, and elevation)?	See Section 5

<sup>3</sup> The available options are correlations relevant to pool boiling in the absence of an abutting packed bed of shielding balls, which are present in the end shield.

	<b>Objectives</b>		<b>Questions to be Answered</b>	<b>Progress</b>
<b>C</b>	Mechanism identification	<b>7</b>	What is the dominant mechanism determining the CHF?	See Section 6
<b>D</b>	Develop a mechanistic correlation	<b>8</b>	What are the constituents of a mechanistic model?	See Section 6
		<b>9</b>	What is the specific form of the model, and the quantities of the model parameters?	Future work
<b>E</b>	Determine current state of calandria tubesheet	<b>10</b>	What is the state of the calandria tubesheet surface in CANDU reactors (roughness, chemical species, contact angle, etc.)?	Future work
<b>F</b>	Differences and similarities to existing knowledge base	<b>11</b>		See Sections 4, 5, and 6

An assessment of the progress toward the overarching and subordinate objectives will be provided in the Section 7 (Conclusions).

#### 1.4. General Notes

The reader is made aware that some information is repeated between the papers presented in Sections 4, 5, and 6. In particular, there is unavoidable overlap in the contextual information in the introductions and literature reviews of these papers. These two areas have some additional commonality with the introduction (1) and literature review and background (2) sections of the thesis. The papers presented in Sections 4 and 6 report the results of experiments making use of the same apparatus, and very similar methods.

Finally, the references in the body of the thesis, and those in the papers it contains are numbered independently.

## 2. Literature Review and Background

The progression of a postulated accident to the IVR core damage state is outlined in Section 1.2. Once a debris bed has formed and partially liquefied at the bottom of the CV (Figure 4), progression of the accident can be halted if the decay heat is removed from the CV without drastic elevation in the temperature of the CV shell. The primary heat transport pathways during IVR would be to the shield tank water via the calandria vessel walls and to the end shields via the calandria tubesheets.

The success of IVR thus depends on the robustness of heat transfer both to the shield tank water and to the water in the end shield. Based on values available in literature [8],[9], heat flux through the tubesheets can be estimated in the range of 100 to 300 kW/m<sup>2</sup>. This falls well below critical heat flux (CHF) values found in literature for vertical surfaces in pool boiling; however, the impact of the packed bed of shielding balls in the end shield is a source of significant uncertainty. A low-resolution description of the expected situation in the end shield would include: void generation at the calandria tubesheet surface, with a two-phase plume rising to the top of the end shield, a single-phase layer of water flowing downward near the fuelling tubesheet, and vapour escaping through the end shield outlets and ultimately to containment via the shield cooling system rupture discs.

The high potential significance of end shield cooling, combined with the associated heat transfer behaviour uncertainties, led to identification of this topic as a high priority research area for COG R&D (CANDU Owner's Group Research and Development) [11]. The importance of this subject has motivated funding of investigations by COG and Candu Energy Inc., with a focus on determining the gross performance of end shield cooling. In addition, the Canadian federal government has funded investigations motivated by a desire to understand the relevant phenomena at a more fundamental level, via the nuclear platform program, and the Federal Nuclear Science and Technology (FNST) program.

At the outset of this literature review, it bears noting that the three papers presented in this thesis constitute the first published studies directly applicable to the prediction of CHF on the calandria tubesheet surface during IVR. This situation calls for a review of related areas of inquiry that may provide context, insight, and guidance contributing to comprehension of the subject. This review will thus include selected concepts and theories from potentially relevant areas of inquiry, but will lack knowledge that can be directly compared to the results of the thesis' novel contributions.

Any discussion of flow boiling is informed by the context of the more fundamental topics of pool boiling and fluid flow. This literature review will proceed accordingly, progressing through pool boiling and one and two-phase adiabatic and diabatic flow, with particular attention paid to the impact of obstructions, porous media, and vertical surfaces where relevant. The relevance of the material covered to the end shield situation will be addressed throughout.

### 2.1. Pool Boiling

Pool boiling is a process that occurs on a heat-releasing surface submerged in a pool of initially stagnant liquid. With low heat fluxes, cooling of the heater through single phase convection is possible (Figure 6, range A-B).

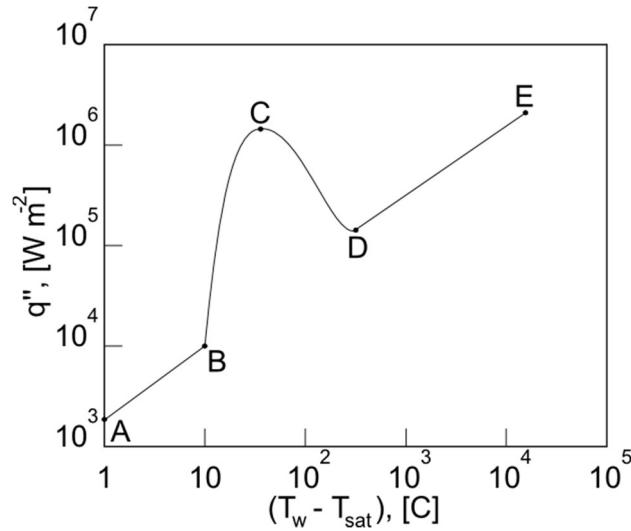


Figure 6. Pool Boiling Curve Schematic

Increasing the heat flux above point B will lead to a the surface temperature of the heater exceeding the saturation temperature of the liquid sufficiently to result in a change of phase of the liquid to a gas – a process expressed through the formation of bubbles at nucleation sites (such as pits and scratches), on the heated surface. This is referred to as the nucleate boiling regime (Figure 6, range B-C). Nucleate boiling in a subcooled liquid is referred to as ‘local boiling’, due to the condensation of bubbles either after they leave the wall or after they grow sufficiently to expand beyond the superheated near-wall layer. Nucleate boiling in a saturated liquid does not involve condensation of bubbles, and is referred to as ‘bulk boiling’. Due to the agitation of liquid near the heated surface and the transport of latent heat resulting from phase change, nucleate boiling is a very effective means of heat transfer, with heat flux varying as  $(\Delta T_{\text{sat}})^n$ , where  $n$  generally ranges from 2 to 5 [27].

The nucleate boiling regime can be divided into two parts: the partial nucleate boiling (or ‘isolated bubble’), region, and the fully developed nucleate boiling region. In isolated bubble nucleate boiling, bubbles are formed and depart cyclically; with heat transport being provided by natural and enhanced convection due to the agitation of the thermal boundary layer by the bubbles, and by latent heat transport by the departing bubbles. Several key parameters increase with wall superheat, including: heat flux, the area density of nucleation sites, bubble departure frequency, bubble departure diameter, and the ratio of heat removed by latent heat relative to convection [28].

With sufficiently high heat flux, increasing bubble diameter and bubble departure frequency results in the replacement of discrete bubbles with the continuous vapour ‘jets’, characteristic of fully developed nucleate boiling. With increasing heat flux, these jets tend to coalesce some distance from the heating surface, forming increasingly large vapour ‘mushrooms’ or agglomerations over a liquid ‘macrolayer’, which is penetrated by vapour stems originating from nucleation sites. The macrolayer includes the ‘microlayer’ – the thin film of liquid in direct contact with the heating surface, where it extends underneath bubbles prior to their departure. Boiling in this regime is governed by phenomena such as evaporation of the macrolayer and departure of the agglomeration. This arrangement is illustrated by Figure 7, a schematic representation of time-averaged void fraction as a function of distance from the heated surface. It should be noted that typically, the thickness of the macrolayer is several times that of the thermal boundary layer. Finally, the evaporative behaviour associated with the vapour stems in the

macrolayer is governed by conduction through the thermal boundary layer, which is strongly influenced by the liquid contact angle (also expressed as wettability).

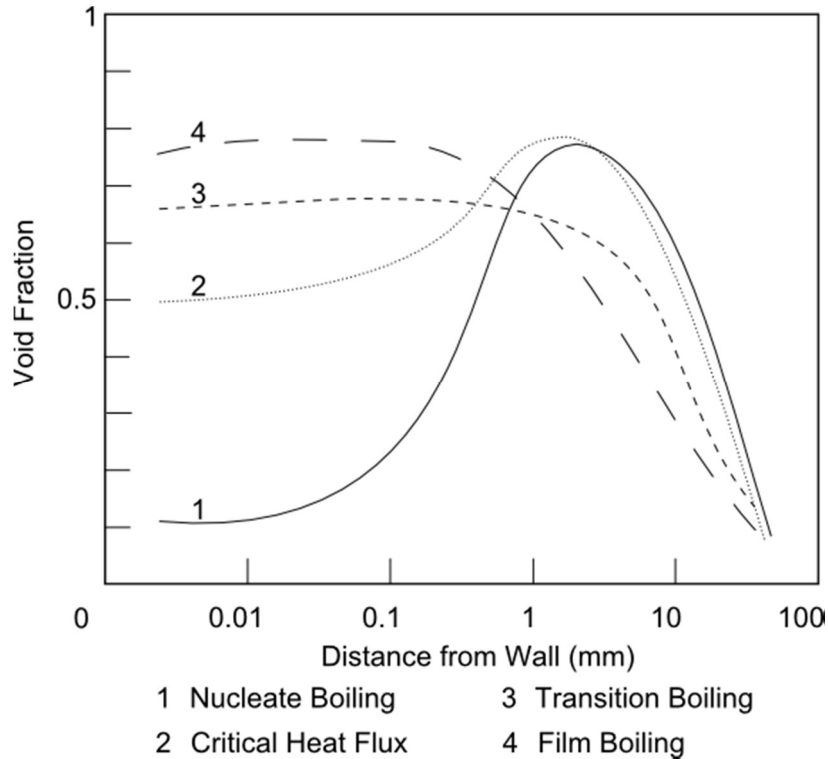


Figure 7. Schematic of Void Fraction Profile for Boiling of Saturated Water at 1 Bar [29]

Increasing heat flux through the nucleate boiling regime, eventually a ‘boiling crisis’ is reached, where the efficiency of heat transfer is reduced, usually as a result of liquid no longer maintaining continuous contact with the heating surface. This takes place at a point referred to as the ‘critical heat flux’ – CHF, (Figure 6, point C). The mechanisms involved in the occurrence of CHF have been the subject of much study, and depend in particular on the geometry of the heater (see Sections 2.1.1 and 2.1.2).

As the temperature of the heating surface increases beyond that associated with CHF, the transition or partial film boiling regime is reached (Figure 6, range C-D). For heat flux controlled surfaces (such as the calandria tubesheet under severe accident conditions), transition boiling is typically passed through swiftly, with excess heat being stored as an increase in heater enthalpy. Eventually, a stable vapour film is established at point D (the minimum heat flux, or Leidenfrost point). Above this temperature, the stable film boiling regime is established (range D-E), where heat is transferred from the surface, through the vapour film, to the liquid via conduction, convection, and radiation. Again, for heat flux controlled surfaces, the temperature of the surface will continue to rise through this regime until the heat flux removed by film boiling matches that added to the heater.

Pool boiling is relevant to the topic of end shield behaviour under severe accident conditions because, depending on the postulated scenario, cooling of the end shield may not be available, and conditions may initially be stagnant. Indeed, the normal operational cooling of the end shields involves liquid velocities that are low enough to be nearly negligible. If the shielding balls and lattice tubes are ignored, the calandria tubesheet can be described as a vertical heated surface cooled by pool boiling. Despite the

geometric differences, this area of inquiry provides valuable guidance for interpretation of two-phase flow boiling in the end shield geometry. Due to the potential implications of a boiling crisis regarding calandria tubesheet integrity, the study of CHF in pool boiling is of particular interest, and takes precedence over investigation of other boiling regimes.

### 2.1.1. Horizontal Surfaces

Nucleate boiling over a horizontal, upward-facing heating surface has been studied for decades; however, due to the greater importance of CHF, consideration of nucleate boiling will be limited to the first and most widely applied correlation developed by Rohsenow [29]. It is expressed as a single-phase forced convection correlation, based on a presumed bubble agitation mechanism, taking the form shown in equation 3.

$$Nu = C_1 Re^x Pr^y \quad (3)$$

The Rohsenow correlation is more typically expressed as shown in equation 4, where the variables ‘ $n$ ’ and ‘ $C_{s,f}$ ’ depend on the fluid-surface combination. In principle,  $C_{s,f}$  accounts for the impact of surface conditions, though the database of experimentally determined values for this variable is limited and an educated guess of its value must often be made [29].

$$q'' = \mu_l h_{fg} \left[ \frac{g(\rho_l - \rho_v)}{\sigma} \right]^{1/2} \left( \frac{c_{p,l} \Delta T_e}{C_{s,f} h_{fg} Pr_l^n} \right)^3 \quad (4)$$

As with nucleate boiling, a brief overview of film boiling over horizontal surfaces is called for. Conditions for a stable vapour film resemble those of laminar film condensation. Consequently, many film boiling correlations are adapted from film condensation, where the dominant feature is conduction across the liquid film. The primary difference lays in the fact that film boiling correlations include convection and radiation as the main constituents, with radiation increasing in relative importance with wall superheat.

Critical heat flux has been the subject of a great deal of research in recent decades. Theofanous et al. [30],[31] have clarified CHF as a process governed by phenomena in the microlayer. While recognizing that the mechanisms involved remain obscured by a “heavy multiplicity of chaotically undulating liquid-vapour interfaces”, they propose a framework of ‘scale separation’ for understanding CHF, with near-wall microhydrodynamics being the suggested focus. The near-wall region is that separated from the wider pool thermalhydraulics by the high void region visible in Figure 7.

While a number of governing mechanisms have been proposed, with associated predictive correlations, the difficulty of directly observing these mechanisms and the variation of behaviour under different conditions has left the matter unsettled, and the subject of some controversy [29]. This leads to a situation in which several models are relatively successful at predicting CHF, in spite of being based on contradictory mechanisms. In spite of the attending uncertainty, the mechanisms proposed for CHF in pool boiling on a horizontal surface may provide context useful to the conceptualization of CHF in geometries resembling the end shield; although it is possible that they may not be directly applicable. The most prominent mechanisms and associated models are outlined in Sections 2.1.1.1 to 2.1.1.5.

### 2.1.1.1. Hydrodynamic Instability Model of CHF

The CHF phenomenon on a horizontal surface was first explained through hydrodynamic theory. This theory was developed by Kutateladze (via dimensional analysis), in 1950 [32] and Zuber (via classical hydrodynamics), in 1959 [33]. Zuber's intuitively informative approach involved calculation of the limits of vapour transport through the Rayleigh-Taylor and Kelvin-Helmholtz instabilities. A schematic of the situation considered by the hydrodynamic theory is shown in Figure 8.

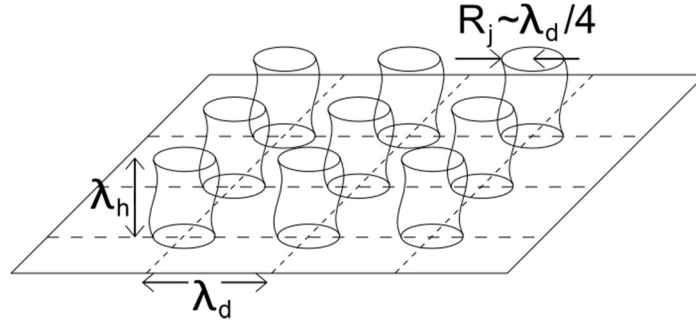


Figure 8. Schematic of Hydrodynamic Theory of Critical Heat Flux

The Rayleigh-Taylor [34] instability refers to a situation where one fluid is accelerated toward a second, more dense fluid. The pertinent application of this instability is a horizontal, upward facing surface which produces vapour. The vapour is less dense than the overlaying liquid, and the stationary system subject to gravity experiences acceleration from the vapour toward the liquid. Above a wavelength determined by the opposing forces of surface tension and buoyancy, perturbation of the interface between the two fluids will grow exponentially. Equation 5 expresses the wavelength for which the perturbation will grow fastest, referred to as the Taylor wavelength. Zuber assumed a spacing of vapour jets equal to the  $\lambda_d$ .

$$\lambda_d = 2\pi \left[ \frac{3\sigma}{g(\rho_l - \rho_v)} \right]^{1/2} \quad (5)$$

The Kelvin-Helmholtz instability arises when two fluids of different densities flow parallel to their interface at differing velocities. Under the high heat flux conditions typically associated with CHF, the formation of discrete bubbles ceases, with vapour transport being replaced by continuous vapour jets. The rising vapour jets are adjacent to falling liquid columns, providing the analogy to the Kelvin-Helmholtz instability. Perturbation of the interface between fluids results in high and low pressure areas adjacent to concave and convex profiles of the interface. The pressure thus acts to increase the perturbations, and as in the Rayleigh-Taylor instability, the surface tension provides an opposing stabilizing force. Equation 6 expresses the velocity for which, at a given perturbation or Helmholtz wavelength, the interface between fluids is unstable [35].

$$u_g = \left[ \frac{2\pi\sigma}{\rho_g\lambda_h} \right]^{1/2} \quad (6)$$

Having a vapour jet spacing and velocity, Zuber then calculated the maximum heat flux for which vapour could be removed from the surface by stable vapour jets by assuming a reasonable Helmholtz wavelength and vapour jet radius. Zuber and Kutateladze both arrived at equation 7, with Zuber deriving a value of  $C = 0.1309$  analytically, and Kutateladze using an empirically-based value of  $C = 0.131$ . Further modifications and extensions of the hydrodynamic theory outlined by Leinhard and Dhir [36], including a suggested adjustment of  $C = 1.49$ .

$$q''_{CHF} = C\rho_g^{1/2}h_{fg} [\sigma g(\rho_l - \rho_g)]^{1/4} \quad (7)$$

It is important to recognize that the hydrodynamic theory, as shown in equation 7, is independent of surface conditions. Subsequent experimental investigation has found surface conditions to have a significant impact on CHF, even finding conditions where the apparent hydrodynamic limits can be exceeded. Further, observed behaviour has been inconsistent with the mechanism identified in the hydrodynamic theory. With that said, this approach can be a useful starting point, is adaptable to geometries other than infinite horizontal surfaces [36], and informs the approaches taken by many other models.

### 2.1.1.2. Macrolayer Dryout Model of CHF

Due to limitations of the experimental knowledge base, the behaviour of fully developed nucleate boiling was not understood as presented at the beginning of this section until after the development of the hydrodynamic model. According to the macrolayer dryout model of CHF proposed by Haramura and Katto [37], during fully developed nucleate boiling, the Helmholtz instability acts on vapour stems associated with nucleation sites, resulting in the formation of vapour agglomerations with a diameter equal to the Taylor wavelength – in other words, a number of vapour stems typically contribute to a single vapour agglomeration. This is in contrast to the hydrodynamic theory, where CHF results from the Helmholtz instability acting on vapour jets distributed over a grid corresponding to the Taylor wavelength.

Under the macrolayer dryout model, CHF occurs when the macrolayer evaporation time exceeds the hovering period of the agglomeration. Using this model, CHF can be expressed as shown in equation 8; where  $\alpha_M$  represents void fraction in the macrolayer,  $\delta_o$  represents the macrolayer thickness at vapour agglomeration departure, and  $\tau$  represents hovering time.

$$q''_{CHF} = \frac{(1 - \alpha_M)\delta_o\rho_l h_{fg}}{\tau} \quad (8)$$

Haramura and Katto calculated the hovering time using an expression derived by Katto and Yokoya [38], which is predicated on the volumetric growth rate of the bubble and the balance of buoyancy force and upward mass acceleration of the two-phase fluid overlaying the bubble (equation 9). The macrolayer thickness was calculated as the critical wavelength for the Helmholtz instability as shown in equation 10, where  $A_v$  is the cross-sectional area of vapour stems, and  $A_w$  is the area of the heated surface. Finally, the void fraction in the macrolayer was chosen to bring the predictions into agreement with the CHF data (equation 11).

$$\tau = \frac{(1 - \alpha_M)\delta_o\rho_l h_{fg}}{\tau} \quad (9)$$

$$\delta_o = 0.5\pi\sigma \left[ \frac{\rho_l + \rho_g}{\rho_l\rho_g} \right] \alpha_M^2 \left( \frac{\rho_g h_{fg}}{q''} \right)^2 \quad (10)$$

$$\alpha_M = 0.0584 \left( \frac{\rho_g}{\rho_l} \right)^{0.2} \quad (11)$$

### 2.1.1.3. Bubble Crowding Model of CHF

The original mechanism of close packing of bubbles leading to a reduction in wetted area of the heated surface, and hence reduction in heat flux with increased wall superheat, was proposed in 1956 by Rohsenow and Griffith [39]. Although this model quickly fell out of favour, related models explaining the impact of contact angle could also be categorized as a bubble crowding models.

A model conceptually similar to bubble crowding was proposed in 1989 by Dhir and Liaw [40]. The bases of vapour stems in the macrolayer reduce the wetted area of the heating surface. Recognizing that the area density of nucleation sites increases with contact angle, with the density of vapour stems increasing correspondingly, they developed a model predicting heat transfer from fully developed nucleate boiling through CHF and transition boiling to the minimum heat flux for poorly wetted surfaces, as a function of contact angle. In this model, CHF occurs as a result of an increased density of nucleation sites, and hence, vapour stems.

Another related model proposed by Kolev [41], uses turbulence in the boundary layer due to bubble departure (accounting for contact angle), as a method for predicting heat transfer in nucleate boiling. Although not intended to predict CHF, the model predicts an increase in nucleation site density with wall superheating, accompanied by a decrease in bubble departure diameter and bubble departure time. Given this trend, there is some level of wall superheat at which additional increase does not lead to higher heat flux; with values of superheat and heat flux agreeing closely with experimental CHF data.

### 2.1.1.4. Hot-Spot Heating Model of CHF

After the evaporation of the liquid microlayer underlying the vapour stems, the temperature increases through the agglomeration hovering period until departure and the rewetting of the surface. Unal et al. theorize that CHF occurs when, during this cycle, the temperature under the vapour stem increases above the Leidenfrost point [29]. The dry spot is not rewetted at the conclusion of the cycle, and continues to spread, leading to CHF. Although this mechanism has not been directly observed, calculations of the temperature rise of hot spots support its plausibility.

Theofanous et al. [30],[31] also identify the transient appearance of hot-spots during nucleate boiling, and connect CHF to the spreading of a subset of these. This conclusion should be qualified by the observation that the appearance, growth, and disappearance of hot spots have a clear relationship with the thermal diffusivity and thickness of the heating surface; and further, that the BETA experiment supporting these conclusions used a 140 – 1000 nm thick Titanium heater, forming an extremely thin and smooth coating on a thin layer of borosilicate glass. Despite the use of heaters of nano-scale thickness, the BETA tests

achieved heat fluxes up to 1.6 MW/m<sup>2</sup>, which is somewhat inconsistent with other data indicating a marked decrease in CHF for thin heating surfaces and surfaces with poor thermal conductivity.

#### 2.1.1.5. Vapour Cutback Model of CHF

Kandlikar [42],[43], proposes vapour cutback as the mechanism responsible for CHF. During boiling, evaporation at the liquid-vapour interface results in recoil forces, which push back the contact line (see Figure 9), resulting in a thin vapour film underneath the liquid. This process oscillates during boiling, with the advancing and receding contact angles dependent on surface conditions and fluid properties. Based on the vapour cutback mechanism, Kandlikar developed equation 12 for critical heat flux.

$$q''_{CHF} = h_{fg} \rho_g^{1/2} \left( \frac{1 + \cos\beta}{16} \right) \left[ \frac{2}{\pi} + \frac{\pi}{4} (1 + \cos\beta) \cos\phi \right]^{1/2} [\sigma g (\rho_l - \rho_g)]^{1/4} \quad (12)$$

Where  $\beta$  is the contact angle, and  $\phi$  is the angle of orientation of the surface. The inclusion of surface orientation is of particular relevance to the topic at hand.

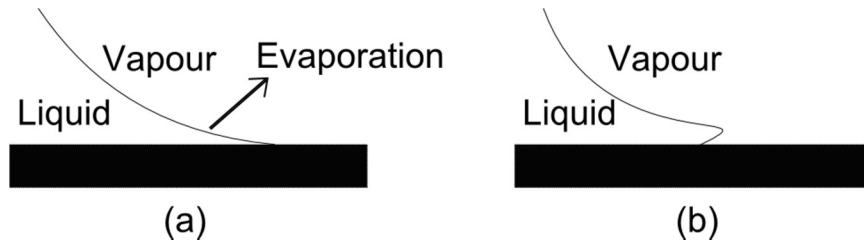


Figure 9. Schematic of Vapour Cutback Mechanism [43]

#### 2.1.2. Vertical Surfaces

Pool boiling on vertical surfaces has been studied somewhat less thoroughly than it has on horizontal surfaces. This is due in part to the added complexity of buoyancy driven flow parallel to the surface, creating a situation somewhat analogous to forced flow. A significant fraction of investigations that have been performed on vertical surfaces have involved vertical cylinders, representative of fuel rods in some reactor designs. Pioro et al. [44] point out the common trend of increased heat transfer coefficient during nucleate boiling with the height of a given heated surface, resulting from increased flow velocity; however, the impact of the height of heaters on CHF is somewhat less obvious.

While the size of a horizontal heated surface may impact the critical heat flux if it is sufficiently small, the impact of height on CHF for vertical heated surfaces is more complex and necessitates some semantic clarification. It is obvious at the outset that hydrodynamic conditions incident upon the surface will be a function of vertical location, as subcooling, void fraction, flow regime, and flow velocity will be influenced by boiling at lower elevations. With this in mind, critical heat flux in this geometry can be interpreted either as a local value or as a limiting heat flux applied uniformly to the surface, which will lead to a boiling crisis at some point on the surface. In the latter case, CHF is likely to vary strongly with the dimension of the heater. Most of the literature on the subject uses the latter definition of CHF, which is both relevant and convenient for smaller heating surfaces, but must be applied with caution to larger ones.

Photographic studies have indicated that at high heat fluxes, boiling on near-vertical surfaces (between  $60^\circ$  and  $165^\circ$  where  $0^\circ$  is upward-facing horizontal), tends to result in the formation of a ‘wavy interface’ between vapour and liquid due to a Kelvin-Helmholtz instability, as shown in Figure 10 [45]. The critical wavelength,  $\lambda_c$ , should not be confused with the Rayleigh-Taylor or Kelvin-Helmholtz critical wavelengths, as these are calculated as special cases involving zero velocity, and zero gravity, respectively. For saturated water at atmospheric pressure, the critical wavelength is approximately 2mm. This wavelength may have a significant impact on the behaviour of boiling on the calandria tubesheet due to the shielding ball contact points which are spaced approximately 11mm apart.

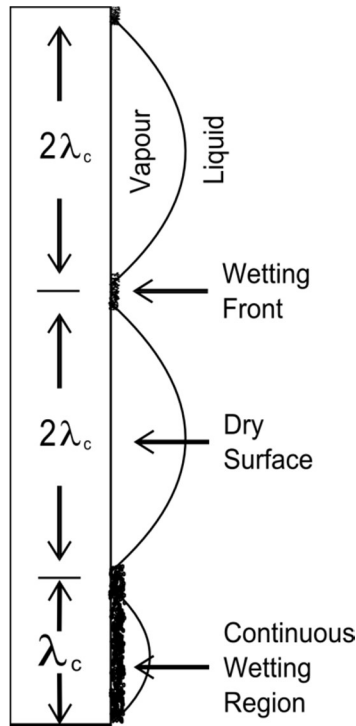


Figure 10. Wetting Front Propagation along Vertical Heated Surface [45]

Continual contact is not maintained between the liquid and the surface; however, cyclical re-wetting prevents deterioration of heat transfer. Under this regime, a boiling crisis occurs when the momentum of the vapour generated at the wetting front is sufficient to lift the wetting front off of the surface [45].

This nucleate boiling and CHF behaviour stands in strong qualitative contrast with that of smaller curved surfaces. In situations such as boiling on calandria tubes after pressure tube ballooning, bubbles can generally be observed to quickly move away from the surface, even at downward-facing angles. This behaviour results from a combination of hydrodynamics of the flowing two-phase mixture and the momentum imparted to bubbles through vaporization. The pre-existing literature does not permit prediction of whether the influence of the shielding balls will result in vapour following the calandria tubesheet as is the case with plain vertical walls, or if it will migrate laterally (experimental observations of vapour transport are included in Sections 4, 5, and 6).

One of the strong appeals of pool boiling for researchers is the simplicity of the situation in the absence of forced flow; such that relevant calculations on boiling behaviour can proceed without primary consideration given to flow outside the microlayer, as suggested by Theofanous [30],[31]. However, it

appears that this simplification is not relevant in the case of vertical heated surfaces. The identification of disparate pool boiling regimes in the downward-facing, near-vertical, and upward-facing orientations [45] precludes the applicability of any single mechanistic model for either nucleate boiling or CHF at all angles, for heaters of larger scale than the continuous wetting region shown in Figure 10. Further, although micro-scale phenomena are doubtless key in determining behaviour of the wetting front, the observation that transient dryout occurs on a macroscopic scale as a result of the wavy interface prior to the boiling crisis precludes the application of models based exclusively on micro-scale behaviour.

Models and correlations that are ostensibly applicable to vertical surfaces that follow from CHF criteria based solely in the microlayer include the vapour cutback model proposed by Kandlikar (equation 12), and the macrolayer dryout model proposed by Haramura and Katto (equation 8). Given the observations of Howard and Mudawar, it seems reasonable to restrict these models to angles between  $0^\circ - 65^\circ$ , or perhaps to  $90^\circ$  if very small heating surfaces are employed.

With the aforementioned caveat in mind, starting from equation 8, Haramura and Katto derive an expression for CHF in upward forced flow on a vertical plate of finite size that follows from ignoring entrainment and deposition such that supply and depletion of the macrolayer at the top and bottom of the heated surface are the only considerations [37] (see equation 13, where  $G$  is the mass flux and  $L$  is the length of the heater). Despite the apparent inapplicability of equation 8 to large vertical surfaces without obstruction, equation 13 is of particular interest since it is possible that the wavy interface will not form in the end shield geometry due to the interference of the shielding balls; in which case replenishment of the macrolayer associated with ball contact points may be an important mechanism, and some expression resembling equation 13 may be appropriate.

$$q''_{CHF} = Gh_{fg} \left( \frac{\rho_v}{\rho_l} \right)^{0.467} \left( 1 + \frac{\rho_v}{\rho_l} \right)^{1/3} \left( \frac{\sigma \rho_l}{GL} \right)^{1/3} \quad (13)$$

A review of experimental studies by Howard and Mudawar [45] shows that CHF typically has an inverse relation with surface angle – that is to say, that the majority of available data sets indicated a reduction in CHF on vertical surfaces relative to horizontal ones. This trend is reflected in most correlations including surface angle as a parameter. These statements must be qualified, however, as there is disagreement amongst data sets. While most experimental work has shown CHF values for vertical geometries between 70-100% of their horizontal counterparts, the data are not consistent. Most notably, an experimental study by Yang et al. [46], of CHF using 0.5 mm thick stainless steel surfaces and water observed an increase relative to horizontal of approximately 10% in CHF at vertical. Reflective of the experimental data, correlations typically predict either reduction of CHF for vertical surfaces, or else a constant value between horizontal and vertical. The first and most commonly cited correlation incorporating the effects of surface orientation was developed by Vishnev [47], based on a fit of liquid helium data (equation 14).

$$\frac{q''_{CHF}(\theta)}{q''_{CHF}(0^\circ)} = \frac{(190 - \theta)^{1/2}}{190^{1/2}} \quad (14)$$

Leinhard and Dhir [36], outline an approach to extension of the hydrodynamic model to finite heaters of various geometries, including vertically oriented ribbons. While the mechanism underlying for the hydrodynamic theory (instability of vapour jets departing the surface - Figure 8) has not been consistently

observed in experimental studies, the approach nevertheless provides reasonable agreement with data for many surfaces, along with a conceptual approach that has clearly influenced the development of other mechanistic models.

The easy adaptation of the Zuber's correlation to widely varied geometries makes it a potential candidate for formulating a correlation for the very complex arrangement of the tubesheet-shielding ball interface. The approach taken by Leinhard and Dhir is to use part of Zuber's derivation of the hydrodynamic limits of coolability for infinite flat plates (equation 15) [33], and determine the appropriate values for the area of vapour jets ( $A_j$ ), and the area of the heater surface ( $A_h$ ), where  $u_g$  is given in equation 6. The applicability of this approach will depend greatly on the observed behaviour of the system.

$$q''_{CHF} = \rho_g h_{fg} \left( \frac{A_j}{A_h} \right) u_g \quad (15)$$

Another source of information on pool boiling angular dependence is the work done in support of in-vessel retention for light water reactors. Care must be taken in the interpretation of this data for CHF on large hemispherical (SBLB facility, Yang et al. [48], equation 16) and cylindrical (ULPU-2000 facility, Theofanous et al. [49], equations 17, 18) heated surfaces, both because these differ geometrically from flat plates, and at a more mundane level, because of the reversal of angular measurements, with  $0^\circ$  taken as downward – facing horizontal.

$$q''_{CHF}(\theta) = (1 + 0.036 \Delta T_{sub})(0.434 + 0.347 \theta + 0.0604 \theta^2) \frac{MW}{m^2} \text{ for } 0^\circ < \theta < 90^\circ \quad (16)$$

$$q''_{CHF}(\theta) = (500 + 13.3 \theta) \frac{kW}{m^2} \text{ for } \theta < 15^\circ \quad (17)$$

$$q''_{CHF}(\theta) = (540 + 10.7 \theta) \frac{kW}{m^2} \text{ for } 15^\circ < \theta < 90^\circ \quad (18)$$

Although it is difficult to separate the impact of surface orientation from that of hydrodynamic conditions, the results of the ULPU-2000 and SBLB tests underline the importance of the spatial variation of hydrodynamic conditions arising from natural circulation on CHF. This aspect was emphasized by the implementation of a baffle in the ULPU-2000 which channelled the two phase flow along the surface, resulting in a siphoning effect. The impact was small but positive near the vertical surface, where velocity was relatively high without the baffle; but it was significant at downward facing angles, where flow was added where conditions were otherwise nearly stagnant.

A final related source of information may be the subject of critical heat flux in vertical tubes with a closed bottom, as studied by Katto and Hirao [50]. In this case, the maximum heat flux is limited by the downward annular flow of water along the walls. The value and axial location of CHF is strongly dependent on the height to diameter ratio of the tube, with proportionately shorter tubes experiencing CHF at higher axial locations, with higher heat fluxes. Although the flow behaviour through the porous medium of shielding balls is sure to be distinct from the observed annular flow in closed bottom tubes, it

is possible that these trends may be applicable to understanding of the limits of end shield cooling on a large scale, as it is conceivable that the upward flow of vapour may impede the downward percolation of water.

### 2.1.3. Porous Media

The most significant areas of investigation into porous media pool boiling CHF are: volumetrically heated porous media in the context of either debris bed cooling [51] or proposed liquid-cooled nuclear reactors with spherical fuel elements, and micro-porous coatings on surfaces to enhance CHF. Additionally, there has been some experimental and analytical work done involving heated surfaces adjacent to porous media of a relevant scale (see Section 2.1.3.1). None of the information available in the literature on this topic has any direct application to the prediction of CHF on vertical surfaces adjacent to a medium such as the end shield.

It is worth noting that in the film boiling regime, cooling of the surface will likely be improved by the addition of conduction through the ball contact points to the heat removed through the vapour film. Similar behaviour has been considered in analytical work in the area of effective conductivity of porous media incorporating conduction, local convection, and radiation [52]. It is possible that the occurrence of CHF in the end shield geometry may not lead to catastrophic temperature increases so long as the interface between water and vapour does not retreat overly far from the calandria tubesheet. In particular, it may be possible to establish the viability of cooling in the event that nucleate boiling on the calandria tubesheet cannot be maintained in localized areas (such as underneath lattice tubes).

#### 2.1.3.1. Externally-Heated Porous Media

Some investigations of CHF in externally-heated porous media have been carried out. Although they involve conditions inapplicable to the end shield, these investigations constitute the literature most applicable to the calandria tubesheet. The first analytical efforts assumed a simple model of vapour film adjacent to a vertical heating surface separated by a sharp interface from a single-phase liquid region [53],[54]. For subcooled boiling in this geometry, and assuming a Darcian flow regime, a numerically solvable relation between the Nusselt and Rayleigh numbers was found.

$$Nu_x \propto \sqrt{Ra_x} \quad (19)$$

$$Nu_x = hz/k_{eff} \quad (20)$$

$$Ra_{x,v} = K(\rho_l - \rho_v)gz/\mu_v\alpha_v \quad (21)$$

Subsequent work included a two-phase zone adjacent to the heating surface [55],[56]. Assuming a Darcian flow regime and strong capillary forces, the heat flux at which saturation of the medium adjacent to the heating surface reaches zero can be characterized.

$$q''_{dry} = 2.716 \times 10^{-3} \frac{h_{fg}\sigma}{v_l} \left(\frac{\epsilon K}{L^2}\right)^{1/4} \left(\frac{(\rho_l - \rho_v)gK}{\sigma}\right)^{1/2} \quad (22)$$

Limitations of this model include a lack of experimental validation and inapplicable assumptions: Darcy flow, significant capillary forces, and an infinite thickness of the porous medium in the dimension normal to the heated surface. Despite these limitations, it is worth noting the implication of equation 22 that the dryout heat flux is proportional to:  $K^{3/4}$ ,  $L^{-1/2}$ , and  $\epsilon^{1/4}$ . An additional key implication of this work is that the horizontal extent of the two-phase region in this model is proportional to  $L^{1/2}$ .

Some experimental studies of boiling on surfaces abutting porous media are available, but none directly reflect the geometry of interest. These include studies of heated cylinders in liquid-saturated sands with particle diameters ranging from 0.16 to 1.5 mm [57], horizontal heating surfaces underneath a packed bed of particles with diameters ranging from 1 to 16 mm [58], and spherical heating surfaces in a packed bed of particles with diameters ranging from 2.9 to 19 mm [59]. These investigations agreed in observing a positive relationship between particle size and CHF. It was also observed that for sufficiently small particles, heat flux tended to increase monotonically with temperature during the transition from nucleate to film boiling.

## 2.2. Single-Phase Flow

With heating of the end shield, and particularly after the onset of nucleate boiling, buoyant forces will result in natural circulation. Understanding this behaviour begins with a review of single-phase flow fundamentals.

The categorization of single-phase flow generally follows from the degree of randomness exhibited. In laminar flow, streamlines are orderly arranged with each stream progressing in parallel with its neighbours. Mixing between streams does not occur, even when velocity is distributed non-uniformly. Turbulent flow on the other hand, involves significant randomness and mixing between flow streams. The standard criterion for identification of flow structure is the Reynolds number (equation 23), where ' $v$ ' is the mean flow velocity and ' $L$ ' is a characteristic linear dimension such as tube diameter.

$$Re = \frac{\rho v L}{\mu} \quad (23)$$

A Reynolds number above 2300 is typically assumed to be turbulent, with laminar flow associated with lower values.

### 2.2.1. Single-Phase Flow in Pipes and over Flat Surfaces

For flowing fluids, it is assumed that the first layer of molecules adjacent to any surface is stationary – referred to as the no-slip condition. This combined with the viscosity of the fluid, determines a velocity profile that varies with distance from the wall. Shear stress for laminar flow can be expressed as shown in equation 24 (where ' $r$ ' is the distance from the wall).

$$\tau = \mu \frac{dv}{dr} \quad (24)$$

Expressing the shear stress distribution in terms of the pressure gradient, a velocity profile can be calculated (see Figure 11). Following from conservation of mass, this velocity profile will be independent of axial position for incompressible flow. For diabatic flow, the viscosity will be reduced near the wall, resulting in a sharper velocity gradient in this area.

Turbulent flow can be considered to consist of three layers: laminar, turbulent, and buffer. Shear stress in the laminar layer is the result of viscous forces (as in equation 23), while in turbulent flow it is the result of turbulent effects (equation 25). ‘ $\epsilon$ ’ is referred to as the eddy viscosity, which is typically taken as a function of a proportionality factor known as the mixing length. Shear stress in the buffer layer is the result of both viscous and turbulent forces (equation 26).

$$\tau = \rho\epsilon \frac{dv}{dr} \quad (25)$$

$$\tau = (\mu + \rho\epsilon) \frac{dv}{dr} \quad (26)$$

Qualitatively, the radial intermixing involved in turbulent flow results in a ‘flattening’ of the velocity profile inside flow paths, and a steeper variation close to walls (see Figure 11). This steeper velocity gradient close to the wall in the turbulent flow case results in greater shear stress and a larger pressure drop. The viscosity reduction in the laminar boundary layer during diabatic flow results in a similar velocity profile flattening effect to that seen in heated laminar flow.

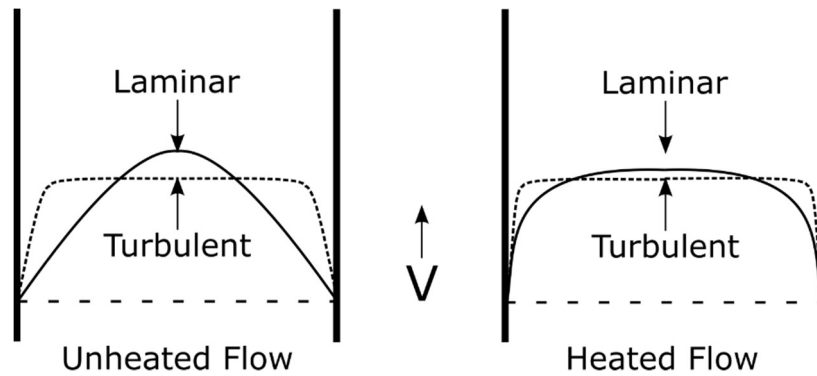


Figure 11. Representative Velocity Profiles for Forced Flow in a Round Pipe

The pressure gradient follows from three force components: friction, acceleration, and gravity. The frictional component of the pressure gradient is proportional to the kinetic energy of the flow, as expressed in equation 27, where ‘ $f$ ’ is an empirically-based friction factor, and ‘ $D$ ’ is the diameter of the (assumed circular), pipe.

$$\left(\frac{dP}{dz}\right)_f = \frac{f \rho v^2}{D} \quad (27)$$

For laminar flow, the friction factor is linear with respect to the Reynolds number, following the Hagen-Poiseuille law for long cylindrical pipes (equation 28).

$$f = \frac{64}{Re} \quad (28)$$

For turbulent flow, friction factors must typically be obtained empirically. These values can be arrived at via iterative means from the implicit, empirically-based Colebrook equation (equation 29, where ‘ $\epsilon$ ’ represents wall roughness). Moody’s diagram (not shown), was introduced to allow graphical determination of friction factors, which is particularly valuable for hand calculations. Various corrections to the friction factor have been proposed for diabatic flow. These are typically based on a ratio of properties in bulk flow and in the near-wall fluid.

$$\frac{1}{\sqrt{f}} = -0.86 \ln \left( \frac{\epsilon/D}{3.7} + \frac{2.51}{Re\sqrt{f}} \right) \quad (29)$$

Natural circulation arises as a result of gravity acting on density differences in a fluid, often resulting from thermal expansion or phase change. In order to address this subject, several dimensionless numbers must be defined. The Nusselt number (equation 30), is expressed as the ratio of convective and conductive heat transfer coefficients – ‘ $h$ ’ is the convective heat transfer coefficient, ‘ $L$ ’ is a characteristic length, and ‘ $k$ ’ is the thermal conductivity of the fluid. The Prandtl number (equation 31), expresses the ratio of momentum and thermal diffusivities – ‘ $C_p$ ’ is the specific heat of the fluid. The Grashof number (equation 32, referring to a vertical flat plate), approximates the ratio of viscous to buoyant forces acting on the fluid – ‘ $\beta$ ’ is the coefficient of volumetric thermal expansion, ‘ $T_s$ ’ is to temperature of the surface, ‘ $T_\infty$ ’ is the bulk temperature, and ‘ $\nu$ ’ is the kinematic viscosity. Finally, the Rayleigh number (equation 33), is the product of the Prandtl and Grashof numbers, and is an indication of whether heat transfer during natural circulation is primarily a result of conduction or convection.

$$Nu = \frac{hL}{k} \quad (30)$$

$$Pr = \frac{C_p \mu}{k} \quad (31)$$

$$Gr = \frac{g\beta(T_s - T_\infty)L^3}{\nu^2} \quad (32)$$

$$Ra = Pr Gr = \frac{C_p \rho g \beta (T_s - T_\infty) L^3}{\nu} \quad (33)$$

For flat surfaces, or any surface if a thin thermal layer is assumed, we can express the Nusselt number as a function of the Rayleigh number and a coefficient that depends on geometry and the Prandtl number

(equation 34). The value of  $c$  is a function of the fluid; and  $n$  depends on the flow characteristics, with  $n = 1/3$  for laminar flow and  $n = 1/4$  for turbulent flow.

$$Nu = c Ra^n \quad (34)$$

Although analyzing the situation using typical natural circulation approaches will not provide a value for CHF, it may prove instructive in understanding flow behaviour. Additionally, some aspects of this approach including the dimensionless numbers listed in equations 30 – 33 may be useful in formulating correlations describing end shield behaviour.

### 2.2.2. Single-Phase Flow in Porous Media

A porous medium is a heterogeneous system composed of a solid matrix with its void filled by fluid. Understanding of porous media is important to the study of topics such as the migration of ground water and petroleum in geological structures, the operation of packed bed chemical reactors, and the cooling and flow behaviour of nuclear reactors making use of spherical fuel elements.

Analysis of porous media often involves application of a local volume-averaging method, involving the selection of a representative elementary volume, which represents local average properties. The purpose of this approach is to obtain a macroscopic momentum equation that does not require detailed calculation of pore-level behaviour.

The structure of porous beds that have been studied varies widely in parameters such as scale, morphology, isotropy, and the volume fraction of free space – referred to as porosity; with different phenomena evident depending on the values of these parameters. This section will focus primarily on those phenomena and approaches relevant to porous media resembling that created by the shielding balls in the end shield.

#### 2.2.2.1. Seeping Flow

The study of porous media began in 1856 with Henry Darcy's work on water percolating through sand. He found that for such flows, pressure loss is proportional to velocity (equation 35). ' $K$ ' is an intrinsic quantity of the porous medium referred to as the 'permeability', with units of length squared. ' $v$ ' is referred to as the superficial velocity, and defined as the volumetric flow rate divided by the total cross sectional area; this is differentiated from the advection velocity, which is the superficial velocity divided by the porosity. The linearity reflected in equation 32 follows from the fact that for slow flows in a porous medium, viscous forces dominate over inertial forces.

$$-\frac{dP}{dx} = \frac{\mu}{K} v \quad (35)$$

Darcy's Law is useful in describing bulk hydrodynamic behaviour, and is a relatively simple and convenient approach; however, this behaviour can in principle be determined from a more fundamental level by application of mass and momentum conservation at a pore level. In practice, use of this approach for calculation of behaviour in complex geometries is a daunting task; consequently, several simplified approaches have been developed, including the hydraulic radius approach, and capillary and drag models [53].

The hydraulic radius model is a semi-heuristic model often referred to as the Carman-Kozeny theory (equation 36, where ‘ $\varepsilon$ ’ represents porosity, and ‘ $d$ ’ represents the mean particle diameter). It is developed from a series of simplifying assumptions, the characterization of equivalent hydraulic diameters, flow velocities, and path lengths (expressed as ‘tortuosity’), and the application of the Hagen-Poiseuille law (see equations 27 and 28). Due to the simplifying assumptions exercised in its derivation and the variation of flow behaviour in different porous media, the applicability of the Carman-Kozeny equation is limited; consequently, modifications have been developed to adjust the results to match experimental data in different situations (e.g. inertial flow – see Section 2.2.2.2).

$$K = \frac{\varepsilon^3}{180(1 - \varepsilon)^2} d^2 \quad (36)$$

### 2.2.2.2. Inertial Flow

The flow rates expected in the end shield during boiling exceed the range of applicability of Darcy’s law. This is determined by calculation of the particle Reynolds number, as expressed in equation 37, where ‘ $v_a$ ’ is the advection velocity, and ‘ $d$ ’ is a characteristic length, such as mean particle diameter. The particle Reynolds number ( $Re_p$ ) in the end shield during boiling would be expected to be on the order of  $10^4$ ; whereas the upper threshold for Darcian flow can be approximated as  $Re_p \approx 10$ . The use of macroscopic fluid speed and a single particle diameter is a means of simplifying a potentially complex pore-scale geometry. The pore geometry is affected by factors including particle shape (sphericity) and size variation that render the transition to a nonlinear regime medium-specific [60]. In the case of the end shield, the shielding balls are nearly spherical, and of uniform diameter. The resulting medium exhibits pore geometry that deviates less from the idealized case than do many other media of interest (for example, the sand beds considered in Darcy’s experiments).

$$Re_p = \frac{\rho v_a d}{\mu} \quad (37)$$

It is observed that between  $1 < Re_p < 10$ , inertial effects begin to affect pressure drops across porous media. This behaviour is addressed by adding an inertial term (referred to as the Forchheimer term), to equation 35, resulting in equation 38. ‘ $K_1$ ’ is referred to as the inertial permeability.

$$\nabla P = -\frac{\mu}{K} \bar{v}_a - \frac{\rho}{K_1} |\bar{v}_a| \bar{v}_a \quad (38)$$

The most commonly applied version of equation 38 was derived by Ergun in 1952 [53] using the hydraulic radius approach of Carman-Kozeny. The roughness of surfaces becomes important under inertial flow conditions, with equation 39 being applicable to smooth surfaces, and an adjustment to the coefficient of the inertial term being used to account for rough surfaces. A variety of other correlations have been developed to predict pressure drops for flow at higher Reynolds numbers, including the widely-cited KTA correlation [61].

$$\nabla P = -\frac{\mu}{K} \bar{v}_a - 1.8 \frac{1 - \varepsilon}{\varepsilon^3} \frac{1}{d} \rho |\bar{v}_a| \bar{v}_a \quad (39)$$

It should be pointed out that direct measurement of flow behaviour has indicated that the onset of inertial effects in porous media flow precedes the transition to turbulent flow, which occurs in the range  $110 > Re_p > 150$ . Observed inertial flow behaviour does not necessarily indicate turbulent flow.

### 2.3. Two-Phase Adiabatic Flow

Flowing fluids in two phases can be categorized according to flow regime, which refers to the relative distribution and motion of each phase. Any prediction of bulk or local flow behaviour must begin with recognition of the overall regime of flow expected in the situation. Flow regime maps are available for a variety of geometries, allowing for prediction of regime based on vapour and liquid fluxes. Unfortunately, no such map is available for geometries relevant to the end shield.

In practice, prediction of pressure drops in two-phase flow is typically at least semi-empirical. A variety of prediction methods may be used, with their results dictated by empirically-based coefficients. As is the case with flow regime maps, the data available for empirical prediction of friction factors in two-phase flow through porous media resembling the end shield, or over relevant obstructions, is lacking.

#### 2.3.1. Two-Phase Flow in Pipes and over Flat Surfaces

In the analysis of two phase flow, the distribution of void is often of primary importance. Several parameters must be defined to allow consideration of this problem. The mass quality expresses the fraction of mass passing down a channel that is in gaseous form (equation 40, where ' $W_g$ ' and ' $W_l$ ' are the vapour and liquid mass fluxes, respectively). If the two phases are not in thermal equilibrium, the thermodynamic quality may also be important (equation 41, where ' $H_l$ ', ' $H_f$ ', and ' $H_{fg}$ ' are the fluid enthalpy, saturated-liquid enthalpy, and latent heat of vaporization, respectively). Finally, the void fraction is defined as the cross-sectional area ratio of vapour and total flow (equation 42). For internal flow, it is common to consider the entire cross-sectional area of the pipe when calculating void fraction. The choice of area is less clearly defined in cases of flow over a surface (e.g. the calandria tubesheet).

$$x_a = \frac{W_g}{W_g + W_l} \quad (40)$$

$$x_{th} = \frac{H_l - H_f}{H_{fg}} \quad (41)$$

$$\alpha = \frac{A_g}{A_g + A_f} \quad (42)$$

Considering the mixture of liquid and gas, the simplest approach is to assume that both phases are travelling at the same velocity – referred to as the homogenous-flow model (equation 43). If the two phases are travelling at significantly different velocities, a separated-flow model is more appropriate (equation 44). The separated flow model, involves a variable ' $K_s$ ', known as the slip ratio, which is the velocity ratio of the gas and liquid phases. The slip ratio is a function of various factors including flow regime and geometry, and typically needs to be determined empirically.

$$\alpha_{\text{homogenous}} = \frac{x_a \rho_l}{x_a \rho_l + (1 - x_a) \rho_g} \quad (43)$$

$$\alpha_{\text{separated}} = \frac{x_a \rho_l}{x_a \rho_l + K_s (1 - x_a) \rho_g} \quad (44)$$

### 2.3.2. Two-Phase Flow in Porous Media

Two-phase flow in a porous medium actually constitutes a three-phase system of solid, liquid, and gas. At the pore level, consideration must be given to interfacial tensions, static and moving contact angles, and Van der Waals interfacial layer forces. The importance of these is largely a function of the scale of the porous medium, with the end shield falling in a size range where these effects do not predominate. The author's judgement is that at present, the relatively undeveloped state of the knowledge base pertaining to end shield CHF calls for somewhat simplified analytical approaches that avoid the challenges presented by a pore level analysis. The approach of considering first the system from a macroscopic perspective is consistent with the historical study of single-phase flow in porous media [62]. The increased complexity of pore-level behaviour during two-phase flow could be expected to magnify the challenges of a potential pore-level analysis.

Macroscopic behaviour of two-phase flow in a porous medium can be approached through consideration of relative permeability and interfacial drag. Relative permeability can be used to express the permeability of each phase as shown in equations 45 and 46 (where ' $K$ ' is the absolute permeability determined for single-phase flows). ' $K_{rl}$ ' and ' $K_{rg}$ ' are functions of matrix structure, saturation (void fraction), surface tension, contact angle, density ratio, and (for transient or quasi-static behaviour), history. For a given matrix, combination of fluids, and saturation, the relative permeability can be taken simply as a function of saturation [53].

$$K_l = K K_{rl} \quad (45)$$

$$K_g = K K_{rg} \quad (46)$$

Determination of relative permeabilities of a porous medium as a function of saturation is possible using comparatively simple experimental means [62]. It should be noted that simultaneous flow typically causes excess resistance in both phases. In fact, in some cases,  $K_{rl} + K_{rg} < 0.1$  for some intermediate values of saturation [53].

When the velocities of each phase are unequal, some interfacial drag  $K_{lg}$  can be expected to provide resistance to flow as a function of the interfacial area ' $A_{lg}$ '. Several correlations have been developed for prediction of these values [53], but, as with two-phase flow in pipes, they are not applicable across different flow regimes. These variables can be expected to lead to some permeability limit – similar to a countercurrent flooding limit – where gas rising at some velocity will preclude the falling of liquid. This effect is of interest to end shield cooling, as it will impact the conditions under which two-phase flow near calandria tubesheet will be concurrent. Further, it is conceivable that near the top of the end shield, a non-zero saturation could be present at all locations between the calandria and fuelling tubesheets. In

such a scenario, the sustainability of liquid supply to the bottom of the end shield may depend on the permeability limit.

As with the relative permeability, determination of the permeability limit using comparatively simple experimental means should be possible [62]. It may also be possible to collect data on the interfacial drag and interfacial area for conditions outside of the limiting case, through similar measurements combined with comparison to the existing knowledge base.

### 2.3.3. Two-Phase Flow in Minichannels

Aside from the porous medium approach, flow through the end shield could also be considered as flow through a collection of interconnected, tortuous minichannels passing through a continuous mass of steel. While this expression of the problem may be redundant in light of the preceding discussion of porous media, it is suggestive of a possibly valuable approach to analysis. Specifically, in the limit where there is no exchange of mass between the flow paths directly adjacent to the calandria tubesheet and the bulk of the end shield, the production of vapour is likely to result in chugging flow regimes or complete and persistent dryout with comparatively low heat fluxes. This approach provides a valuable limiting case for comparison to experimental results.

Attempts have been made at dividing small channels into phenomenologically-relevant size categories. Kandlikar [63], for example, has proposed a division between conventional channels ( $d > 3$  mm), mini channels ( $200 \mu\text{m} > d > 3$  mm), and micro channels ( $10 \mu\text{m} > d > 200 \mu\text{m}$ ). By this definition, the channels between the shielding balls in an end shield fall near the division between conventional and minichannels. As such, capillary forces can be expected to have a limited impact, with treatment of flow paths as conventional channels being cautiously justified.

## 2.4. Two-Phase Boiling Flow

While pool boiling on vertical surfaces as discussed in section 2.1.2 could be described as two-phase flow boiling due to the presence of natural circulation, the large uncertainties associated with the behaviour of the end shields call for a brief review of knowledge under forced flow conditions.

### 2.4.1. Two-Phase Boiling Flow in Pipes and over Flat Surfaces

As with pool boiling, a variety of CHF mechanisms have been explored for two-phase boiling flow. In general, these mechanisms and models must be applied in the context of a specific flow regime.

The scales separation approach and the mechanism of dry spot spreading can be applied to most convective boiling situations, as it is with pool boiling [64],[65]. The critical heat flux is still typically determined by behaviour of the near-wall microlayer; however, shear between the microlayer, vapour blanket, and bulk flow plays an important role. The shear between the vapour blanket and bulk flow leads to liquid entrainment via the Kelvin-Helmholtz instability, with these droplets depositing on the microlayer or any dry spots that may be formed. Additionally, the shear forces between the vapour blanket and microlayer result in stabilization of the thin film, discouraging the formation of dry spots. The result of these factors is that, at high velocities, the orientation of a surface is relatively unimportant in determining CHF.

Other approaches include consideration of: dryout under a vapour agglomeration or slug flow bubble (see equation 13), near-wall bubble crowding and vapour blanketing preventing the ingress of liquid to the surface, and film dryout in annular flow.

In practice, prediction of CHF in two-phase flow is largely empirically-based. Methods include lookup tables, which are composed of large arrays of different input parameters – such as pressure, temperature, flow rate, and void fraction – for which experimental results are available, and from which desired values can be interpolated. The various correlations that are used for predicting CHF in two-phase flow conditions will not be discussed, but a brief outline of relevant parametric effects may be useful. CHF typically increases linearly with subcooling. Tube length has an inverse relationship with CHF for given inlet conditions; this is relevant to the end shield in the limit where no lateral exchange of mass is considered between flow paths adjacent to the calandria tubesheet and the bulk of the end shield – as discussed in section 2.3.3. At low mass flux, CHF increases rapidly with flow rate, and eventually approaches a constant value. CHF typically increases with pressure before falling off as the critical point is approached. Finally, the orientation of a surface has very little effect on CHF for high flow rates, but in the limit of low flows, the significant reduction for downward-facing surfaces seen in pool boiling is approached.

#### 2.4.2. Two-Phase Boiling Flow over Obstructions

Obstructions in flowing channels tend to promote turbulence and mixing between streamlines. This has the effect of improving heat transfer at surfaces and increasing CHF, but also increasing flow resistance. It is important to consider the interplay of these two effects in, for example, nuclear reactor primary heat transport system design, where the optimization of CHF safety margins and the pressure drops dictating the capabilities of expensive and power-hungry pumps must be considered. In the case of the end shield, where the flow is driven by buoyancy, the interplay of heat transfer promotion, void fraction, and flow velocity can be expected to influence the primary concern of CHF.

Obstructions can take a variety of forms, beginning with the continuum of progression from smooth to rough pipes. The impact of roughness on the friction factor is accounted for by the Colebrook equation (equation 29) for pipe flows. Roughness can also be ‘discrete’, which refers to a separation between obstacles such that flow is neither continuous nor fully-developed. Discrete obstacles are often employed for CHF enhancement, such as mixing vanes in LWR fuel assemblies.

#### 2.4.3. Two-Phase Boiling Flow in Internally-Heated Porous Media

As is the case with pool boiling, there is a significant body of knowledge for flow boiling CHF in two main geometries involving porous media: volumetrically heated porous media in the context of both debris bed cooling [51] or proposed liquid-cooled nuclear reactors with spherical fuel elements, and micro-porous coatings on surfaces to enhance CHF. However, as observed in section 2.1.3, investigations in these geometries have no obvious application to CHF on vertical surfaces adjacent to a porous medium such as the end shield.

### 3. Experimental and Analytical Methods

The purpose of this section is to provide context to assist readers in the understanding of the methods used in the papers presented in Sections 4, 5, and 6, rather than to reiterate information provided in Sections 1 and 2.

As discussed in Sections 1 and 2, the knowledge base applicable to CHF in the end shield was very limited at the outset of the work outlined in this thesis. The ability to analyze the phenomenon is hampered by a lack of knowledge of behaviour of the system, including the mechanisms of CHF. In addition, no experimental data is available to validate predictions arising from such analyses. Under such circumstances, the performance of ‘exploratory tests’ is warranted, to improve understanding of the system’s behaviour. This approach is recommended by the Hierarchical, Two-Tiered Scaling Analysis, An Integrated Structure and Scaling Methodology for Severe Accident Technical Issue Resolution [66], for areas where large uncertainties in system behaviour exist.

Some preliminary exploratory experiments were performed by the author prior to those reported in this thesis, but are not included, given that the results have not been published

#### 3.1. Heated Experiments

The apparatus utilized in the papers presented in Sections 4 and 6 is outlined in Sections 3.1.1 to 3.1.3, and the experimental procedures are summarized in Section 3.1.4. A schematic of the apparatus is shown in Figure 12.

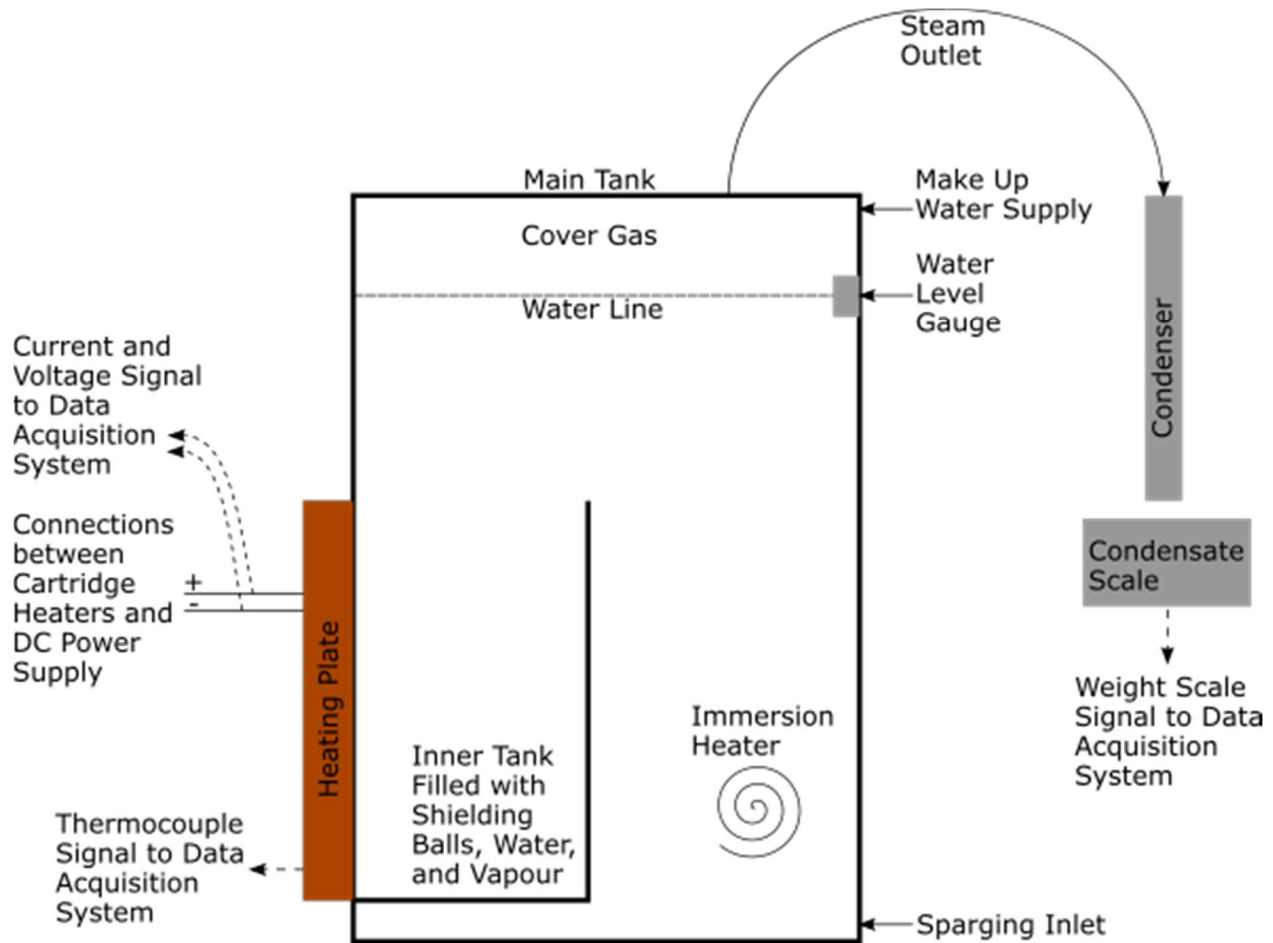


Figure 12. Schematic of Apparatus Used for Heated Experiments

### 3.1.1. Heating Plate

The apparatus utilized in the papers presented in Sections 4 and 6 represented the calandria tubesheet with a thick metal block heated by embedded cartridge heaters. This approach was selected for the following reasons:

- The large thermal capacitance of the heating plate slows the temperature transient following a boiling crisis. This permits avoidance of damage to the plate, permitting performance of repeated tests.
- The macroscopic irregularities arising from the presence of the shielding balls in contact with the heating plate suggests that conduction parallel to the surface is a phenomenon of potential importance to CHF. This would lead to an increase in CHF with heating plate thickness, for sufficiently thin plates. In an open pool with an upward-facing heating surface, the thickness at which the effect of plate thickness becomes negligible has been proposed to be a function of the nucleation site size and spacing [67]. Given the diameter of the shielding balls and the associated spacing of the contact points, it is reasonable to expect that the thickness above

which a calandria tubesheet's thickness would have negligible impact on CHF would be less than the calandria tubesheet thickness of 51 mm.

- A thick plate facilitates the measurement of spatial temperature distribution across the wall thickness. Thermocouples can be embedded throughout the plate, measuring temperature gradients, permitting calculation of heat fluxes and extrapolation of heating surface temperatures.
- In practice, a resistively heated plate can be used to produce only a fixed heat flux distribution, approximately inversely proportional to the local plate thickness - a quantity that cannot be easily varied from test to test. A thick plate heated by cartridge heaters presents an opportunity to shape the heat flux by varying the power supplied to each of the cartridge heaters.

Heat passing through the plate will lead to a thermal gradient inversely proportional to the plate's thermal conductivity. While the calandria tubesheet is composed of stainless steel 304L, it was determined that the relatively low thermal conductivity of this material would present challenges to experimental design. Instead, copper was used, with its high thermal conductivity reducing the maximum temperatures predicted in the plate to values compatible with both the plate material and the cartridge heaters.

The heating plate was designed with a height corresponding to the height of the region of contact between the calandria tubesheet and the crust surrounding the corium pool (0.6 m). This is the region where heat flux supplied to the calandria tubesheet during IVR would be expected to be highest.

The cartridge heaters were selected to match the capabilities of the power supply used for the experiment. The heaters produced their full designed power output at 120 V; whereas the power supply was capable of delivering up to 150 V (DC). The electrical resistance of the heaters was a function of temperature, and hence varied during operation; however, it can be stated that under the conditions of the experiments, the heaters exhibited an average resistance of approximately 6.7  $\Omega$ . The maximum and minimum resistances of individual heaters were within 0.2  $\Omega$  of the average. The heaters were designed with a longitudinal split, such deformation driven by thermal expansion pressed the two halves of the heaters into the walls of the holes in which they were located, improving heat transfer.

The depth of the holes housing the thermocouples was measured with a precision of 0.025 mm, and a measurement uncertainty of 0.05 mm.

The heaters were positioned in a grid, located sufficiently far from the heating surface that the temperature field distortions close to the heaters dissipated at a reasonable distance from the surface, leaving a temperature gradient field close to normal to the surface. This avoided a non-representative 'wavy' exiting heat flux profile, and facilitated the measurement of heat flux using embedded thermocouples. The dimensions of the heating plate, and the positions of the cartridge heater and thermocouple holes are provided in Section 4.

### 3.1.2. Secondary Design Features

In the work presented in Sections 4 and 6, an open-topped polycarbonate tank held a packed bed of shielding balls against the heating plate. This was enclosed by a larger tank filled with water at saturation temperature. The material selection was motivated primarily to facilitate observation of the system, in particular the liquid-vapour plume rising adjacent to the heating plate. The inner tank height

and width was slightly larger than that of the heating plate, and it extends half of the heating surface height (300 mm) from the plate. The ‘water bath’ approach was chosen to facilitate the sealing of components, and also to mitigate edge effects and thermal losses.

The main experimental tank was sealed, with the sole escape path for vapour being through a condenser. The rate at which water condensate was produced was monitored in real time during the test, permitting a redundant measurement of heat supplied to the system, and performance of a heat balance.

In light of the potential for oxidation of shielding balls, the water used in the experiments was sparged using a noble gas to remove oxygen. Finally, the water was heated using immersion heaters to ensure that saturation temperature is maintained.

### 3.1.3. Instrumentation

Thermocouples were used extensively to measure the temperature field throughout the heating plate discussed in Sections 4 and 6, as well as the temperature of the water used in the experiments. Thermocouples make use of the Seebeck effect, by which a thermal gradient in a conducting material results in a corresponding voltage gradient. The ratio of these gradients varies between conducting materials. In a thermocouple, an electrical junction is made between two wires, positioned at a location where the temperature is to be measured. The voltage difference between the two wires is measured at another location with a known temperature (the reference junction). A characteristic relationship between voltage and temperature difference can then be used to calculate the temperature at the measurement location. The thermocouples used in these experiments were ‘type K’, with one leg being composed of chromel (an alloy containing nickel and chromium) and the other being composed of alumel (an alloy containing nickel, aluminum, manganese, and silicon).

The thermocouples used in the experiments were calibrated by bringing the junction to a series of known temperatures, and recording the measurement bias. A three-point calibration (100 °C, 200 °C, and 400 °C). The precision was 0.01 °C, and the maximum calibration uncertainty was 0.3 °C. A similar exercise was carried out with the data acquisition system, applying a voltage characteristic of type K thermocouples at a series of temperatures, and observing the bias in the recorded results. A six-point calibration was used for the data acquisition system (0 °C, 200 °C, 400 °C, 600 °C, 800 °C, and 1000 °C), with a precision of 0.01 °C and a maximum calibration uncertainty of 0.1 °C. The two resulting calibration curves were then used to correct the temperatures recorded by each thermocouple during the experiments, linearly interpolating between the measured points on the calibration curves. During the experiments, thermocouple data (along with electrical and condensate scale measurements) was recorded by the data acquisition system at a frequency of 10 Hz.

The primary uses of the thermocouples in the heating plate were to measure the heat flux, and to sense the initiation of temperature transients. Closely clustered groups of thermocouples were embedded in the heating plate, with the junctions located at different distances from the heating surface. The temperatures measured by these thermocouples were then used to establish a thermal gradient within the plate. This thermal gradient was used to calculate the local value of heat flux, using the thermal conductivity of the plate material, via Fourier’s law (see Equation 1).

The voltage and current supplied to the cartridge heaters was measured throughout the tests. Given the presence of thick insulation on the surfaces of the plate not in contact with water, effectively all of the heat generated by the cartridge heaters can be assumed to have exited that heating surface. The electrical power delivered to the cartridge heaters was then divided by the surface area of the heating plate (0.18 m<sup>2</sup>) to calculate the spatially averaged heat flux at steady state.

Given that the water in the apparatus was kept at saturation temperature, and that water vapour exiting the apparatus would also be saturated, a heat balance can be calculated by multiplying the vapour production rate (inferred from the rate at which condensate exited the condenser) by water's latent heat of vaporization at atmospheric pressure (see Equation 47). The condensate scale was subjected to a seven point calibration (0 kg, 10 kg, 20 kg, 30 kg, 40 kg, 50 kg, 60 kg) through the addition of calibrated weights, with a precision was 0.1 g, and a maximum calibration uncertainty of 0.5 g. A heat balance for steady state operation, with makeup water supplied at saturation temperature can be calculated as shown in Equation 47:

$$q = h_{lv} \frac{dM_c}{dt} - q_{added} + q_{lost} \quad (47)$$

Where  $M_c$  is the condensate mass,  $q_{added}$  is the thermal power supplied by the immersion heater, and  $q_{lost}$  is the thermal power lost from the outer surfaces of the main tank (see Figure 12). When operating at a steady state, the value of  $q_{loss}$  calculated by Equation 47 is within the range of uncertainty of calculated heat loss estimates derived from natural convection from the outer surface of the main tank.

#### 3.1.4. Experimental Procedure

Each test was carried out by increasing power to the heating plate in a stepwise fashion, with a steady state achieved at each power level prior to the subsequent power increase. A series of heat fluxes at which nucleate boiling could be maintained was thus established, each constituting a lower bound of the CHF. Eventually, a heat flux was reached at which a temperature transient was observed, establishing an upper bound of the CHF. Nucleate boiling was not directly observed, but was inferred through a combination of wall superheat (less than 30 °C), the production of vapour (observed as it exited the top of the packed bed of shielding balls), and the establishment of a steady state.

In experiments where a non-uniform heat flux was desired to be delivered (see Section 4), cartridge heaters were divided into as many as three groups. The electrical power delivered to each of these groups was then varied, producing the desired exiting heat flux profile.

#### 3.1.5. Repeatability of Results

Quantification of the repeatability of experiments performed with this apparatus is complicated by the evolving nature of the heating plate surface, as detailed in Sections 4 and 6. Investigation of the relationship between surface conditions and CHF is the focus of subordinate objective A, question 2, as summarized in Table 5. The set of results representing the most consistent surface conditions was carried out using borosilicate shielding balls, as part of the experimental campaign outlined in Section 6. These results can be utilized for the conditional quantification of the repeatability of results produced using the apparatus. The uncertainty bands of the three measurements (defined by the upper and lower bounds of CHF established through the stepwise power increases described in Section 3.1.4) overlap, as shown in Figure 11 of Section 6. Taking the average of the upper and lower bounds of each

test as the measured value of CHF, the standard deviation of the measurements is 5.97 kW/m<sup>2</sup> (1.9% of the mean) and the standard deviation of the mean is 3.45 kW/m<sup>2</sup> (1.1% of the mean).

### 3.2. Air Barbotage

One of the subordinate objectives outlined in Table 5 was to characterize the hydrodynamics of the end shield cavity during IVR. The air barbotage technique as used to address this (Section 5). This technique has been employed widely in the study of boiling, with pioneering investigations of the hydrodynamics associated with CHF carried out by Kutateladze [68], and other investigations performed subsequently [69][70].

In simulating the phenomenon of interest, a perforated plate was used to represent the calandria tubesheet, adjoining a volume representing the end shield cavity. Air was injected through the perforated plate, serving as a simulant of water vapour in the end shield cavity. A simple equivalence can be expressed between heat flux in the reactor case, and air flow rate in the air barbotage (see Equation 48).

$$A'' = q''v / h_{lv} \quad (48)$$

Where:

- $A''$  is the volumetric air flux [m/s]
- $q''$  is the heat flux [W/m<sup>2</sup>]
- $v$  is the specific volume of water vapour [m<sup>3</sup>/kg]
- $h_{lv}$  is the latent heat of vapourization of water [J/kg]

Further explanation of the technique and a discussion of its validity can be found in Section 5.2.

The apparatus (see Figure 13) permitted visual observation of the simulated end shield cavity, while varying parameters including shielding ball diameter, air flow rate, and end shield cavity dimensions. Visibility was facilitated through the use of transparent (acrylic) shielding balls. Video recordings were made of experiments performed with different combinations of these parameters. These recordings were analyzed, permitting various observations, including quantification of the extent of the air-water two-phase plume adjacent to the perforated plate.

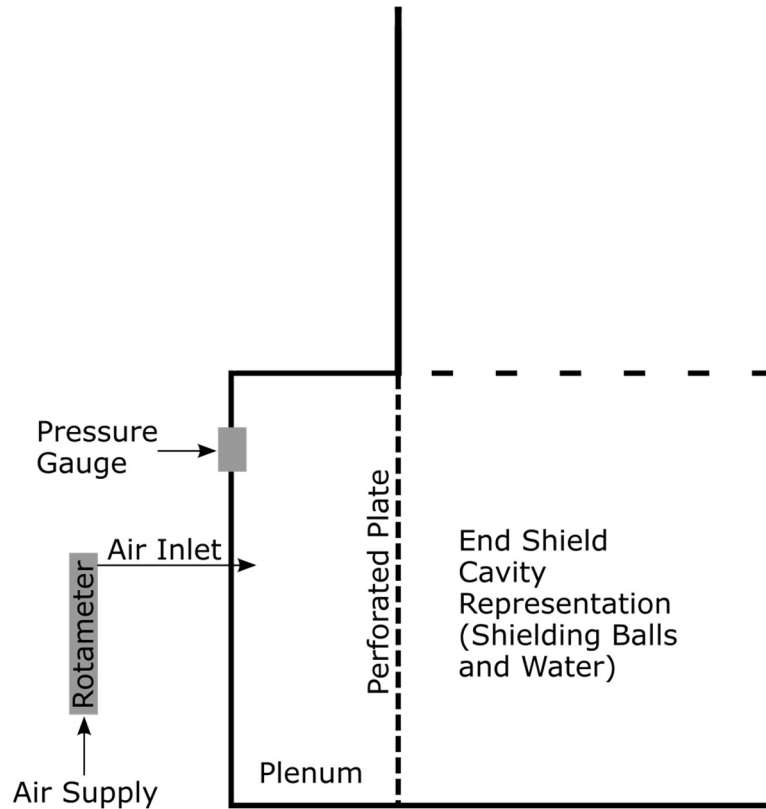


Figure 13. Schematic of Apparatus Used for Air Barbotage Experiments

Instrumentation used with this apparatus was limited to the following:

- An air rotameter used to measure air flow rate, having a measurement uncertainty of  $\pm 0.24$  l/s. This yields an uncertainty of  $7.5 \text{ kW/m}^2$  in equivalent heat flux,
- A calibrated analog pressure gauge, with a measurement uncertainty of 3 kPa, and
- An optical video camera.

Further apparatus details and images are provided in Section 5.2.4.

## 4. Measurement of Critical Heat Flux in a CANDU End Shield Consisting of a Vertical Surface Abutting a Packed Bed of Steel Shielding Balls

### 4.1. Preface

#### 4.1.1. Citation

The paper can be cited as follows:

J. Spencer, Measurement of critical heat flux in a CANDU end shield consisting of a vertical surface abutting a packed bed of steel shielding balls, CNL Nucl. Rev. 6(1) (2017) 79 90

#### 4.1.2. Contribution to Knowledge

Prior to the publication of this paper, the literature applicable to boiling on the surface of the calandria tubesheet during IVR (and specifically to CHF) was very limited. The inability to predict the behaviour of the system motivated the objectives of this paper.

The first objective of the paper was to quantify the CHF, and its dependence on key variables. As outlined in Table 5, this objective was approached through investigation of the following questions:

- Does elevation (or heating surface height) affect the CHF, when the exiting heat flux is uniform? If so, how?
- Does the condition of the heating surface affect the CHF? If so, how?

A second objective of this paper was to determine the differences and similarities of the system's behaviour to the predictions available in the literature.

These objectives were approached through the performance of experiments that faithfully represented as many of the key aspects of a CANDU reactor's calandria tubesheet – end shield cavity system as was possible. The calandria tubesheet was represented by a copper block containing embedded cartridge heaters. The copper block abutted a representation of the end fitting cavity, comprising a packed bed of 11.1 mm diameter carbon steel shielding balls (consistent with the specifications for use in a CANDU end shield), filled with water at saturation temperature. The copper block contained 47 type-k that were used to measure the temperature field (hence thermal gradients and exiting heat flux), and detect temperature transients.

The power was increased in a stepwise fashion, with a steady state being achieved at each step. When the boiling surface temperature significantly exceeded a value corresponding to the critical heat flux and continued to increase, it was inferred that the prior nucleate boiling regime had been replaced by a transition or film boiling regime. This implied that a lower bound of the CHF was established by the final step during which nucleate boiling was sustained, while an upper bound was established by the final step during which a transition of boiling regimes occurred.

As outlined in Section 2.1.2, the literature on the subject of CHF on vertically-oriented surfaces during pool boiling indicates that the height of the surface is a key parameter [45]. It was hypothesized that the hydrodynamic conditions would vary with elevation in the end shield, resulting in the CHF having an

inverse relationship with elevation (or heating surface height). The most direct means of quantifying the relationship between heating surface height and CHF would be to use a series of heating surfaces of different heights. This was not deemed a practicable approach, given cost restraints and other practical considerations such as sealing between sections of a segmented heating plate. Instead, the electrical power delivered to the cartridge heaters embedded in the copper block was varied from test to test, such that the exiting heat flux conformed to a desired profile. In a subset of these tests, the exiting heat flux was roughly uniform from the bottom of the heating surface to the location at which a temperature transient initiated. These results were used to quantify the relationship between elevation (heating surface height) and CHF, through least squares regression.

The objective of determining whether the condition of the heating surface was addressed by performing tests with all parameters other than the surface conditions held constant, over a lengthy ‘campaign’ of individual tests. During this campaign, visual observations were made that were consistent with the deposition of iron oxide particles on the heating surface were made. As the campaign progressed, the measured value of CHF increased, suggesting that the CHF is influenced by the heating surface conditions. Neither quantification nor control of these conditions and the resulting characteristics (e.g. contact angle) were possible, precluding reporting of a quantitative relationship between surface conditions and CHF.

The maximum heat flux deliverable by the apparatus ( $806 \text{ kW/m}^2$ ) was found to be lower than the CHF in the absence of shielding balls. This result is consistent with values of CHF for unobstructed vertical surfaces reported in literature (see Section 2.1.2). While measurement of CHF in this configuration would provide a potentially useful comparison to existing literature, it is peripheral to the focus of the investigation. The results of this test involving nucleate boiling in the absence of shielding balls are not published.

The work presented in this section constitutes the first published experimental or analytical results that can be used to quantify the CHF on the calandria tubesheet surface facing the end shield cavity in a CANDU reactor during IVR. As outlined in Section 1.2.2, CHF in this location was found in a PIRT exercise to be a phenomenon with both high importance to severe accidents in CANDU reactors, and a high uncertainty [11]. If the exiting heat flux at this location exceeds the CHF, it is likely that IVR would be lost. The publication of this work significantly improved the ability of safety analysts to assess the CHF in this location, with an empirical correlation quantifying CHF as a function of elevation. Additionally, qualitative observation of vapour transport in the packed bed of shielding balls improved understanding of the system’s behaviour, with the potential to inform further investigations.

#### 4.1.3. Author’s Contribution to Paper

The author led the design process of the apparatus presented in the paper. Following manufacturing of the components by various suppliers, the author directed Atomic Energy of Canada Limited (AECL) technologists in the assembly and preparation of the apparatus. Performance of the experiments was led by the author, with assistance by AECL technologists and the supervisor of the high temperature fuel channel laboratory. Finally, analysis of the experimental data and preparation of the paper was carried out by the author. Limited assistance was provided by an AECL professional in assembling a two dimensional heat transfer model of the heating plate in the finite element code ANSYS.

## 4.2. Publication

### 4.2.1. Abstract

The Critical Heat Flux (CHF) was measured in an experimental apparatus representative of a Canada Deuterium Uranium (CANDU) reactor end shield porous medium heated by a vertical surface. The understanding of peak heat transfer rates in this geometry is crucial to the demonstration of in-vessel retention (IVR) of corium during a postulated severe accident in a CANDU reactor. In this paper, a large-scale experimental apparatus is described, which is capable of measuring CHF from a vertical surface to a packed bed of steel balls representative of a CANDU end shield. Data are presented from a large matrix of tests investigating the impact of heated surface height on CHF. Preliminary analysis of a subset of these data is also presented, as well as the derivation of an empirical, correlation for CHF as a function of elevation along the vertical wall. Qualitative comparisons are made between the results of the tests and predictions of peripherally related work carried out in the past, with reasonable agreement being observed in vapour-phase transport in the porous medium and in trends of CHF. It is expected that future work including further analysis of the current data will allow for the development of an improved mechanistic understanding of the phenomenon, leading to a more broadly-applicable correlation for CHF which is subject to smaller uncertainties, and could be incorporated into severe accident codes such as MAAP CANDU.

### 4.2.2. Nomenclature

$g$	Gravitational acceleration, $m/s^2$
$H$	Heat transfer coefficient, $W/m^2-K$
$K$	Absolute permeability of the medium, $m^2$
$k_{eff}$	Effective thermal conductivity, $W/m-K$
$L$	Heated wall length, $m$
$q''$	Heat Flux, $W/m^2$
$s$	Saturation
$t$	Time, $s$
$v$	Velocity, $m/s$
$z$	Position relative to the bottom of the heating plate, $m$

#### Greek Letters

$\alpha$	Thermal diffusivity, $m^2/s$
$\varepsilon$	Porosity
$\mu$	Dynamic viscosity, $kg/m-s$
$\nu$	Kinematic viscosity, $m^2/s$
$\rho$	Density, $kg/m^3$

$\sigma$  Surface Tension, N/m

Subscripts

*eff* Effective

*l* Liquid

*v* Vapour

Acronyms

BC Boiling Crisis

CANDU CANada Deuterium Uranium

CHF Critical Heat Flux

CNL Canadian Nuclear Laboratories

CV Calandria Vessel

IVR In Vessel Retention

LWR Light Water Reactor

MAAP Modular Accident Analysis Program

MCCI Molten Core Concrete Interaction

SNB Sustained Nucleate Boiling

TB Transition Boiling

TC Thermocouple

TT Temperature Transient

### 4.2.3. Introduction

In a postulated severe accident in a CANDU Pressurized Heavy Water reactor, loss of coolant from the primary heat transport system, combined with loss of the moderator cooling system, may result in core heat-up, moderator boiling, and uncovering of the fuel channels [1][2]. Decay heat would lead to progressive heat-up of the fuel channels, and within several hours, core collapse would result in relocation of debris to the bottom of the calandria vessel (CV) and subsequent formation of a terminal debris bed. Retaining the resulting ‘corium’ material in the calandria vessel – referred to as ‘In-Vessel corium Retention’ (IVR) – would arrest accident progression, avoiding high uncertainty ex-vessel phenomena with the potential to challenge containment integrity such as ex vessel molten fuel coolant interaction and Molten Core – Concrete Interaction (MCCI). Consequently, IVR is a subject of great interest in assessing the consequences of postulated severe accidents in CANDU reactors.

The success of IVR depends upon several physical phenomena which are the subject of either recent or ongoing investigation. One key condition for IVR is effective heat removal from the stainless steel walls

forming the boundaries of the CV. The most efficient heat transport pathway from the CV walls is via nucleate boiling of the surrounding shield water. This boiling regime cannot be sustained above a limit known as the critical heat flux (CHF). Application of heat flux above this critical value raises the possibility of a dramatic shift in boiling regime followed by a temperature escalation and loss of CV wall integrity.

The main boundaries constituting the CV walls are the cylindrical shell and the two calandria tubesheets which separate the CV from the end shields packed with steel balls. CHF in geometries resembling the cylindrical shell has been studied as part of investigations of IVR in the light water reactor (LWR) community [3]-[14]. In contrast, CHF has not been studied in geometries analogous to the surface of the calandria tubesheet facing the coarse porous medium constituted by steel balls and the end shield.

A series of large-scale experiments have been carried out at Canadian Nuclear Labs (CNL) to measure the critical heat flux of the surface of the calandria tubesheet facing the end shield. This paper presents the experimental apparatus and method of operation, as well as an enumeration of the tests and their key conditions. In recognition of the physical complexity of the system, analysis of the data is outlined and applied, allowing for presentation of the results of a subset of the tests in a coherent and useful manner. This process allows for the empirical formulation of a relationship between CHF and the height of a uniformly heated surface abutting a porous medium similar to a CANDU end shield. The test data is available for further analysis, which will allow for a more definitive characterization of CHF and its relation to relevant parameters.

#### 4.2.4. Pre-Existing Knowledge Base

A CANDU reactor's calandria tubesheet and the 11.1 mm diameter steel shielding balls in the end shield constitute a porous medium, externally heated by vertical surface. While there are no existing studies of CHF in such a configuration, key points of the applicable knowledge base are summarized to provide necessary context.

##### 4.2.4.1. Pool Boiling

The boiling crisis (BC) phenomenon has been studied extensively for a variety of applications and in numerous scenarios characterized by geometry, thermalhydraulic conditions, heat-releasing surface and wall continuum characteristics, and coolant properties. Unfortunately, the investigations published in open literature do not appear to sufficiently reflect the end shield geometry.

For the widely studied scenario of pool boiling with a flat, upward-facing surface, proposed approaches to predicting CHF include hydrodynamic [15][16][17], macrolayer dryout [18], hotspot heating [19][20], vapour cutback [21][22], and bubble crowding [23] and related [24][25] models. When a vertical surface is considered, the situation is complicated by the development of buoyancy driven flow parallel to the surface. In this geometry, it is believed that the mechanism determining CHF follows from the formation of a wavy interface between the vapour and liquid phases due to the Helmholtz instability [26]. The presence of the steel shielding balls interferes with the formation of this wavy interface, rendering this model inapplicable to the geometry in question.

Other issues such as surface roughness [19][20], aging [3], and wall thickness [27] have been investigated and found to impact CHF under many circumstances. It is suspected that wall thermal properties and thickness may be of particular importance to the situation in question due to the spatial

variation in surface conditions brought about by the presence of the steel shielding balls in the endshield.

Finally, several experimental programs have examined the feasibility of IVR for externally-flooded LWR pressure vessels under severe accident conditions. These include both flat [13], and curved [3][6], surfaces. Some indication of relevant trends may be taken from the results, particularly the angular dependence of CHF for large surfaces in the SULTAN experiments [13], and the impact of a ‘baffle’ to direct water flow in the ULPU experiments [3]; however, the potential for significant deviation from these results due to the presence of the steel shielding balls cannot be discounted.

#### 4.2.4.2. Externally Heated Porous Media

While not directly applicable to the case at hand, some investigations of CHF in externally heated porous media have been carried out. Early analytical work related to external boiling in porous media assumed a simple model of vapour film adjacent to the heating surface separated by a sharp interface from a single-phase liquid region [28][29]. For subcooled boiling in this geometry, and assuming a Darcian flow regime, a numerically solvable relation between the Nusselt and Rayleigh numbers was found.

$$Nu_x \propto \sqrt{Ra_x} \quad (1)$$

$$Nu_x = hz/k_{eff} \quad (2)$$

$$Ra_{x,v} = K(\rho_l - \rho_v)gz/\mu_v\alpha_v \quad (3)$$

Subsequent work included a two-phase zone adjacent to the heating surface [30][31]. Assuming a Darcian flow regime and strong capillary forces, the heat flux at which saturation of the medium adjacent to the heating surface reaches zero can be characterized.

$$q''_{dry} = 2.716 \times 10^{-3} \frac{h_f g \sigma}{v_l} \left( \frac{\epsilon K}{L^2} \right)^{1/4} \left( \frac{(\rho_l - \rho_v) g K}{\sigma} \right)^{1/2} \quad (4)$$

While the mechanistic assumptions of Darcy flow and significant capillarity are inapplicable to the case under consideration, it is worth noting the implication that the dryout heat flux is proportional to:  $K^{3/4}$ ,  $L^{-1/2}$ , and  $\epsilon^{1/4}$ . An additional key implication of this work is that the horizontal extent of the two-phase region in this model is proportional to  $L^{1/2}$ .

Some experimental studies of boiling on surfaces abutting porous media are available, but none directly reflect the geometry of interest. These include studies of heated cylinders in liquid-saturated sands with particle diameters ranging from 0.16 to 1.5 mm [32], horizontal heating surfaces underneath a packed bed of particles with diameters ranging from 1 to 16 mm [33], and spherical heating surfaces in a packed bed of particles with diameters ranging from 2.9 to 19 mm [34]. These investigations agreed in observing a positive relationship between particle size and CHF. It was also observed that for sufficiently

small particles, heat flux tended to increase monotonically with temperature during the transition from nucleate to film boiling.

#### 4.2.5. Experimental Apparatus and Procedure

The fundamental objective of the experiments is to measure the CHF of a thick vertical plate abutting a porous medium representing the steel shielding balls of a CANDU end shield. This is achieved by heating a thick copper plate via embedded cartridge heaters, which is positioned adjacent to a packed bed of steel balls in a tank filled with stagnant saturated water at atmospheric pressure (Figure 1).

The plate is bolted to a stainless steel housing, which is in turn bolted to the transparent tank which holds the water. Gaskets are used in these connections to avoid water leakage. During operation, all surfaces of the heating plate aside from the boiling surface are well insulated. The boiling surface has a roughness of less than  $1.6 \mu\text{m}$  which is significantly smoother than the specifications of the calandria tubesheet (Figure 2). The heating plate is 0.6 m tall, approximating the height of the portion of the calandria tubesheet in contact with the crust surrounding the corium pool during IVR. This is the region where the highest heat flux to the calandria tubesheet would be expected. In order to minimize the impact of edge effects associated with vapour transport through the packed bed, a heating plate width of 0.3 m was used, providing a low ratio of height to width.

The 48 cartridge heaters contained in the heating plate are located in two columns, the nearest of which is positioned 47.6 mm from the boiling surface so that spatially periodic variations in the temperature gradient are small in this area (Figure 3). The heating plate temperature was measured by 47 embedded Type-K thermocouples. There are five centrally-located cascades of five thermocouples at different depths which are used to establish a temperature gradient, and 22 additional thermocouple positions which are used to identify the occurrence of temperature transients (TT) in their vicinity (Table 1). The thermocouples are inserted from the rear of the heating plate to maintain a smooth boiling surface representative of the CV tubesheet.

The cartridge heaters are powered using a 500 kW DC power supply. Two of the power supply's rectifiers are controlled separately and connected to different groupings of the cartridge heaters, allowing for independence in the heat supplied to different zones of the plate.

The steel balls constituting the porous medium abutting the boiling surface were selected to be representative of the shielding balls used in CANDU end shields, being composed of carbon steel. The diameter of the shielding balls used in the tests is 11.1 mm. This is at the midpoint of the range specified for CANDU 6 reactors, which employ uniform shielding balls with diameters between 9.5 mm and 12.7 mm. The shielding balls are held in place with a transparent inner tank which is open at the top to the main test tank to allow for natural circulation of water in a manner meant to represent conditions in a CANDU end shield during postulated severe accident conditions. The inner tank is 306 mm in width, 610 mm tall, and extends 300 mm in a direction normal to the boiling surface (thickness). A low ratio between the height of the heated surface and the thickness of the inner tank was chosen to minimize the potential impact of constraint of the two-phase region. Qualitative observations indicate that the two-phase region was not constrained in any of the tests. It can thus be concluded that scaling to approximately one third of the end shield thickness would have negligible impact on the results.

The chemistry of the water used in the tests is controlled to represent CANDU shield water, and to minimize oxidation of the carbon steel balls. The initially de-ionized water is sparged using a noble gas to remove oxygen, and LiOH is added to maintain a pH between 10.0 and 10.5. The water is heated using immersion heaters to ensure that saturation temperature is maintained.

To allow for the performance of lengthy tests without depletion of water in the main tank, a make-up water system is included. The make-up tank contains chemistry-controlled, heated water, which is pumped to the main experimental tank when a drop in the water level actuates a flotation switch. The make-up water system maintains the water depth within a 50 mm range.

Heat flux is determined through measurement of the power supplied to the heater cartridges and by measurement of the temperature gradient in the plate. An additional energy check is made by condensing the water vapour produced during the experiments, and measuring mass transient of the condensate, which is collected in a receptacle resting on an electronic scale. The main experimental tank is sealed so that the sole escape path for vapour is through the condenser. A simple steam separator is included at the outlet of the main tank to avoid droplet entrainment; and trace heating and insulation of the steam line between the main tank and the condenser avoids vapour condensation (Figure 4). The reported heat fluxes are calculated from voltage and current measurements characterizing the power supplied to the cartridge heaters. These measurements are taken using calibrated instruments, and uncertainties for these parameters are considered to be negligible.

The optical transparency of the main tank and inner tank allow for the capturing of high-definition still images and video of the behaviour of the system during high-heat flux boiling.

In accordance with safety protocols related to the use of the 500 kW power supply, the tests are operated remotely. Live video feeds allow for observation of the behaviour of the system. The data acquisition program written for the experiment includes real-time monitoring of temperatures read by thermocouples in the heating plate and water tanks, condensate scale weight, electrical power, and heat flux.

Each test was carried out by increasing power to the heating plate in a stepwise fashion. A steady state was achieved at each power level prior to the subsequent power increase – a process that typically required a minimum of three minutes due to the large thermal capacitance of the copper heating plate. This process eventually leads to deterioration in heat transfer at some location on the boiling surface identified by a continuously increasing TT. This deterioration is indicative of a transition from a nucleate boiling (NB) to a transition boiling (TB) regime, and can be characterized as a BC brought about by a heat flux exceeding the CHF for the conditions present at some point on the boiling surface. The highest power level at which sustained nucleate boiling (SNB) is observed and the power level at which the TT is observed can then be considered lower and upper bounds for CHF.

Due to the large thermal capacitance of the plate, TTs observed in this apparatus are much slower than those typically associated with BC in thin plates. As a result, prompt identification of TTs allowed for a reduction in power and re-establishment of nucleate boiling long before temperatures reached a level where damage to the heating plate would be a concern. It was thus possible to repeat many tests in sequence. The tests described in this paper were performed over a five day period, during which the main tank was continuously filled with chemistry-controlled water.

#### 4.2.6. Results

As indicated in the introduction, the physical complexity of the system in question necessitates significant post processing of experimental data before the results can be interpreted in a definitive manner. The complexity of the system arises from two primary sources: heat conduction in the heating plate continuum in the vertical direction due to the spatially inhomogeneous heat flux, and the ‘upstream’ (i.e., lower elevation) impacts of void generation on local hydrodynamic conditions.

For a given heating surface and porous medium, and with the cooling fluid at saturation temperature,  $q''_{CHF}(s, v_l, v_v)|_z$ ; where  $s$  is the local water saturation of the porous medium,  $v_l$  is the liquid velocity,  $v_v$  is the vapour velocity, and  $z$  is the elevation. These values are, in turn a function of  $q''(z)$  where  $z < z'$ . While disentanglement of these factors may be achieved in future work, the current paper will be restricted to presentation of raw results and post-processing which involves the application of significant simplifying approximations.

##### 4.2.6.1. Summary of Experiments Performed

Tests were carried out in eight configurations, characterized by the location of the cartridge heaters powered by each of the rectifiers. These dispositions are outlined in Table 2 – with Zone 1 powered by rectifier 1 and Zones 2a and 2b powered by rectifier 2. A summary of the key results of all tests performed is presented in Table 3. The heat fluxes quoted in this table correspond to the heat delivered via the cartridge heaters, not the heat flux released from the wall. These figures of interest are spatially dependent, and require further analysis to extract.

An example of the data taken during a temperature transient is shown in Figure 5. This shows the temperature measured by thermocouples located at the lateral centre of five different planes. Several tests were examined in detail to determine their implications regarding the dependence of CHF on the height of a heated surface. This analysis required the identification of the locations of the temperature transients observed in these tests, which are summarized in Table 4.

Quantitative measurement of water saturation inside the porous medium in question is technically challenging, and was not carried out during these tests. However, the use of transparent materials in the tank construction allows for continuous qualitative observation the extent of the two-phase region arising from vapour production at the boiling surface. High heat flux nucleate boiling is associated with vigorous, highly turbulent flow of a liquid / vapour mixture through the packed bed. This two-phase region follows a general trend of increasing in thickness with both height and heat flux. The interface between the two-phase region near the wall and the single-phase liquid region beyond is not smooth, but rather is quite wavy. It appears that a flow regime similar to chug flow in a pipe results in frequent protrusion of the two phase region beyond its minimum extent by a horizontal distance on the order of 100 mm. This flow regime may arise from the dependence of inertial permeability on saturation.

The wavy interface between the two-phase and single-phase regions can be seen qualitatively in Figure 6. Qualitatively, observation of the side of the packed bed of shielding balls reveals waves in the interface forming near the bottom of the packed bed and growing as they travel upward. While less obvious in still images, this behaviour can be discerned in the three images spaced 0.4 s apart, during nucleate boiling at a uniform heat flux of 308 kW/m<sup>2</sup>.

Although the physics involved in the inertial flow through a non-capillary porous medium differ significantly from the viscous, capillary situation considered by Wang and Beckerman [30][31], qualitative observations of the extent of the two-phase region exhibit some similarity to their predictions.

#### 4.2.6.2. Surface Aging Correction

At the beginning of each day of testing, one or more `baseline` tests were performed to measure the CHF when the plate was heated as uniformly as possible, but also to quantify the impact of surface aging. A clear trend in these tests was evident (see Figure 7), with CHF increasing over time as observed by other investigators [3][4]. A logarithmic curve was fit to the data (equation 5), where  $t$  is the time since testing began in seconds.

$$q''_{CHF} \left[ \frac{kW}{m^2} \right] = 9.499 \left[ \frac{kW}{m^2} \right] \ln(t [s]) + 254 \left[ \frac{kW}{m^2} \right] \quad (5)$$

Because the nature of the parameters causing the aging effect is unknown, the choice of a logarithmic function was purely empirical; other classes of functions could be used to fit the data within the experimental uncertainties. All results were then scaled in accordance with this curve, centred at an early baseline test with a relatively low CHF to provide a somewhat conservative treatment of surface conditions.

#### 4.2.6.3. Finite Element Simulation of heating Plate

Due to the spatially inhomogeneous heat flux delivered to the heating plate, significant heat conduction in the vertical dimension can be expected. In order to account for this effect, a two dimensional heat transfer model of the heating plate was developed using the finite element code ANSYS. As a simplifying assumption, the boiling surface was taken to have a uniform temperature of 120 °C – a temperature corresponding to high heat flux nucleate boiling in these tests. Simulations were performed for the SNB and TT power levels for each of the tests listed in Table 4, and the results were scaled for surface aging. The results for SNB and TT power levels are shown in Figures 8 and 9, respectively. The potential ranges of position for the TTs identified using TC data as shown in Table 4 are shown for each transient in Figure 9 as a solid line.

#### 4.2.6.4. Critical Heat Flux

The highest SNB heat fluxes for each of the cases shown in Table 4 were taken as a lower limit to CHF. Following from the observation that regions of transition or film boiling spread more quickly upward than they do downward, and recognizing the trend that CHF increases monotonically with elevation, the conservative assumption is made that each TT initiated at the lowest elevation in the range identified in Table 4. The approximation is then made that the heat flux at lower elevations is constant and equal to the heat flux at the assumed location of TT initiation. The result is a set of six data points with small uncertainty with respect to heat flux and large uncertainty with respect to position (Figure 10). The line of best fit identified in Figure 10 is described by equation 6.

$$q''_{CHF} \left[ \frac{kW}{m^2} \right] = -519.4 \left[ \frac{kW}{m^3} \right] z [m] + 539.6 \left[ \frac{kW}{m^2} \right] \text{ for } 0.058 \text{ m} < z < 0.398 \text{ m} \quad (6)$$

This line of best fit was produced using the least-squares method and has  $R^2 = 0.9037$ . As the functions  $s(z, q'')$  and  $q''_{CHF}(s)$  are currently unknown, extrapolation of this preliminary CHF correlation beyond the range of elevations represented by the data points used in formulating this correlation would be associated with large uncertainty.

While the data points used in developing this correlation are lower bounds, the correlation itself cannot be considered completely bounding, as it does not underlie all data points. It is expected that future work will provide insight into the trends of CHF and saturation with respect to height as well as relevant mechanisms and phenomena. This should allow for the production of a correlation whose form is more reflective of the physics involved than the linear relationship outlined above.

As observed regarding some qualitative aspects of the results, the negative trend of CHF with respect to height is consistent with that predicted for the mechanistically different situation of viscous flow in a capillary porous medium [30][31].

#### 4.2.7. Summary

In this paper, details are given for a large-scale experimental apparatus capable of measuring CHF in an endshield porous medium externally heated by a vertical surface. Data are presented from a large matrix of tests investigating the impact of heated surface height on CHF. Preliminary analysis of a subset of these data is presented, resulting in an empirical, relatively conservative correlation for CHF as a function of elevation (equation 6).

Qualitative comparisons of the results of the tests are made to predictions of peripherally related work carried out in the past, with reasonable agreement being observed in vapour-phase transport in the porous medium and in trends of CHF. It is expected that future work including further analysis of the presented data will allow for additional insight into the impact of key mechanisms influencing these results, leading to a more broadly-applicable correlation for CHF which is subject to smaller uncertainties. Such work is particularly important in light of the potential differences between CHF for copper and stainless steel surfaces, to allow for direct application to the reactor case.

Prior to this work, the publicly available knowledge base was devoid of experiments or analyses applicable to CHF in coarse porous media externally heated by a vertical surface. Understanding of heat transfer in such a scenario has potentially significant impacts on the nuclear community's capability to accurately predict IVR and overall accident progression during a postulated severe accident in a CANDU reactor.

#### 4.2.8. References

- [1] J.C. Luxat, "Thermal-Hydraulic Aspects of Progression to Severe Accidents in CANDU Reactors", Nuclear Technology, 2009 July
- [2] T. Nitheanandan and M.J. Brown, "Backup and Ultimate Heat Sinks in CANDU Reactors for Prolonged SBO Accidents", Nuclear Engineering and Technology, Vol. 45 No. 5, 2013 October
- [3] T.G. Theofanous, S. Syri, T. Salmassi, O. Kymalainen and H. Tuomisto, Critical heat flux through curved, downward facing, thick walls, Nuclear Engineering and Design 151 (1994) 247-258
- [4] T.G. Theofanous and S. Syri, The Coolability Limits of a Lower Reactor Pressure Vessel Lower Head, Nuclear Engineering and Design 169 (1997) 59-76
- [5] S. Angelini, J.P. Tu, Yu.A. Buyevich and T.G. Theofanous, The mechanism and prediction of critical heat flux in inverted geometries, Nuclear Engineering and Design 200 (2000) 83-94

- [6] J. Yang, F.B. Cheung, J.L. Rempe, K.Y. Suh and S.B. Kim, Correlations of Nucleate Boiling Heat Transfer and Critical Heat Flux for External Reactor Vessel Cooling, ASME Summer Heat Transfer Conference, San Francisco, CA, 2005 July 17-22
- [7] J. Yang, M.B. Dizon, F.B. Cheung, J.L. Rempe, K.Y. Suh and S.B. Kim, CHF enhancement by vessel coating for external reactor vessel cooling, Nuclear Engineering and Design 236 (2006) 1089-1098
- [8] T.G. Theofanous, C. Liu, S. Additon, S. Angelini, O. Kymalainen and T. Salmassi, In-vessel coolability and retention of a core melt, Nuclear Engineering and Design 169 (1997) 1-48
- [9] O. Kymalainen, H. Tuomisto and T.G. Theofanous, In-vessel retention of corium at the Loviisa plant, Nuclear Engineering and Design 169 (1997) 109-130
- [10] S.W. Nob and K.Y. Suh, Critical heat flux for APR 1400 lower head vessel during a severe accident, Nuclear Engineering and Design 258 (2013) 116-129
- [11] T.Y. Chu, J.H. Bentz and R.B. Simpson, Observation of the boiling process from a large downward facing torispherical surface, Proceeding of National Heat Transfer Conference, American Nuclear Society, Portland, OR, USA, 1995 August 5–9
- [12] T.Y. Chu, B.L. Bainbridge, R.B. Simpson and J.H. Bentz, Ex-vessel boiling experiments: laboratory and reactor-scale testing of the flooded cavity concept for in-vessel core retention. Nucl. Eng. Des. 169 (1997), 77–88
- [13] S. Rouge, SULTAN test facility for large-scale vessel coolability in natural convection at low pressure, Nucl. Eng. Des. 169 (1997), 185–195
- [14] Y.H. Jeong and S.H. Chang, Critical Heat Flux Experiments on the Reactor Vessel Wall Using 2-D Slice Test Section, Nuclear Technology, 152 (2005 November), 2, 162-169
- [15] S.S. Kutateladze, Hydrodynamic model of heat transfer crisis in free-convection boiling, J. Tech. Phys. 20(11) (1950) 1389–1392
- [16] N. Zuber, Hydrodynamic Aspects of Boiling Heat Transfer, PhD Thesis, Dept. of Eng., UCLA, 1959
- [17] J.H. Lienhard and V.K. Dhir, Extended Hydrodynamic Theory of the Peak and Minimum Heat Fluxes, NASA CR-2270, 1973
- [18] Y. Haramura and Y. Katto, “New Hydrodynamic Model of Critical Heat Flux Applicable Widely to both Pool and Forced Convection Boiling on Submerged Bodies in Saturated Liquids”, Int. J. Heat Mass Transf., 26, pp. 379–399, 1983
- [19] T.G. Theofanous, J.P. Tu, A.T. Dinh and T.N. Dinh, The boiling crisis phenomenon part I: nucleation and nucleate boiling heat transfer, Exp. Therm. Fluid Sci. 26, pp. 775–792, 2002
- [20] T.G. Theofanous, J.P. Tu, A.T. Dinh and T.N. Dinh, The boiling crisis phenomenon part II: nucleation and nucleate boiling heat transfer, Exp. Therm. Fluid Sci. 26, pp. 793–810, 2002
- [21] S.G. Kandlikar, A Theoretical Model to Predict Pool Boiling CHF Incorporating Effects of Contact Angles and Orientation, Journal of Heat Transfer, Vol. 123, pp. 1071-1079, 2001 December
- [22] S.G. Kandlikar and M.E. Steinke, Contact angles and interface behavior during rapid evaporation of liquid on a heated surface. International Journal of Heat and Mass Transfer 45, 3771–3780, 2002

- [23] W.M. Rohsenow and P. Griffith, Correlation of Maximum Heat Flux Data for Boiling of Saturated Liquids, Chem. Eng. Prog. Symp. Series (52): 47-49, 1956
- [24] V.K. Dhir and S.P. Liaw, Framework for a Unified Model for Nucleate and Transition Pool Boiling, J. Heat Transfer (111): 389-399, 1983
- [25] N.I. Kolev, How accurately can we predict nucleate boiling? Exp. Therm. Fluid Sci. 10, pp. 370–378, 1995
- [26] A.H. Howard and I. Mudawar, Orientation effects on pool boiling critical heat flux (CHF) and modeling of CHF for near-vertical surfaces, Int. J. Heat Mass Transfer 42, pp. 1665–1688, 1999
- [27] I.I. Gogonin, Influence of the Thickness of a Wall and of its Thermophysical Characteristics on the Critical Heat Flux in Boiling, Journal of Engineering Physics and Thermophysics, Vol. 82, No. 6, 2009
- [28] E.M. Parmentier, “Two-phase natural convection adjacent to a vertical heated surface in a permeable medium”, Int. J. Heat Mass Transfer, 22, pp. 849-855, 1979
- [29] P. Cheng and A.K. Verma, “The effect of subcooled liquid on film boiling about a vertical heated surface in a porous medium”, Int. J. Heat Mass Transfer, 24, pp. 1151-1160, 1981
- [30] C.Y. Wang and C. Beckermann, “A two-phase mixture model of liquid-gas flow and heat transfer in porous media. Part II: Application to pressure-driven boiling flow adjacent to a vertical heated plate”, Int. J. Heat Mass Transfer 36, pp. 2759-2768, 1993
- [31] C.Y. Wang and C. Beckermann, “Boundary-layer analysis of buoyancy-driven two-phase flow in capillary porous media”, J. Heat Transfer, 117, pp. 1082-1087, 1995
- [32] V.E. Schrock, R.T. Fernandes and K. Kesavan, “Heat transfer from cylinders embedded in a liquid filled porous medium”, Heat Transfer, Proc. Int. Heat Transfer Conf, Vol. 7, Pap. CT3.6., 1970
- [33] S. Fukusako, T. Komoriya and N. Seki, “An experimental study of transition and film boiling heat transfer in liquid-saturated porous bed”, J. Heat Transfer 108, pp. 117-124, 1986
- [34] V.X. Tung and V.K. Dhir, “Experimental study of boiling heat transfer from a sphere embedded in a liquid-saturated porous medium”, J. Heat Transfer, 112, pp. 736-743, 1990

#### 4.2.9. List of Figures

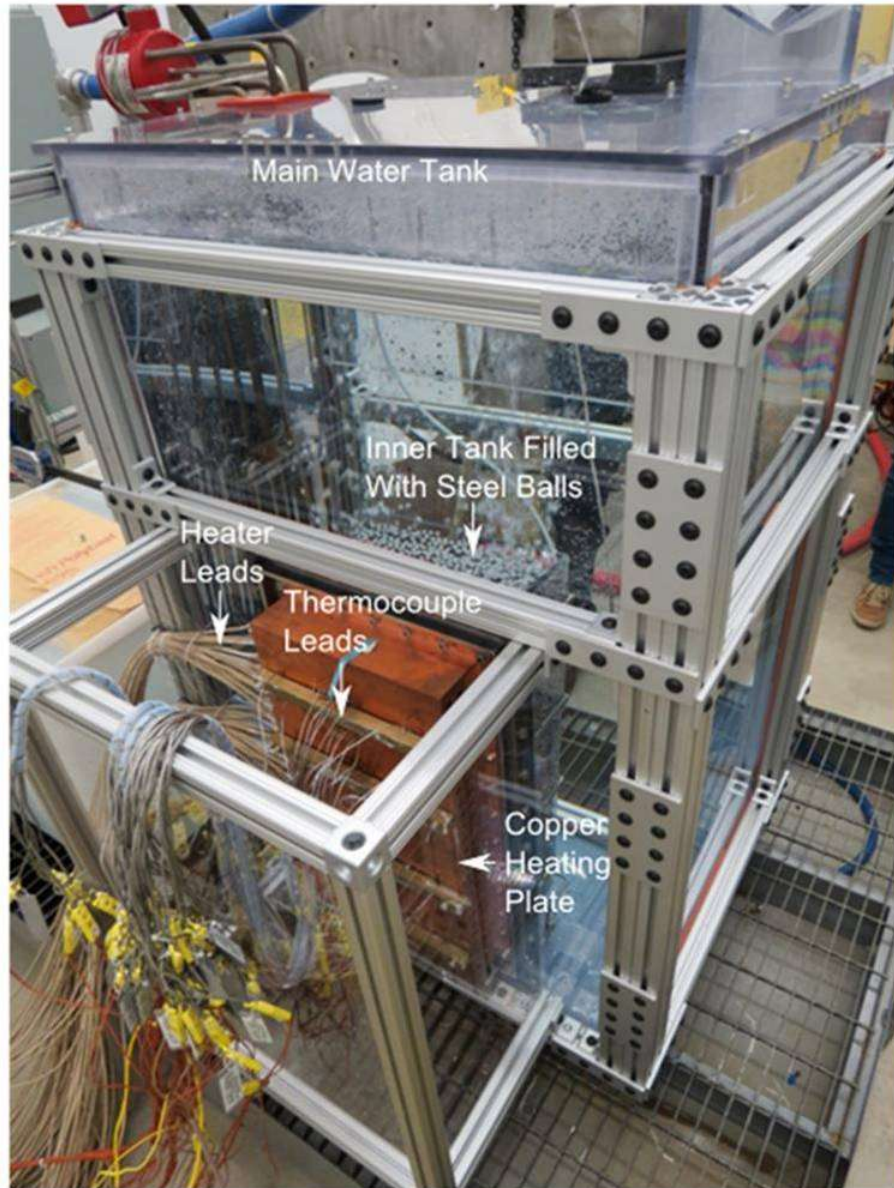


Figure 1. Instrumented copper heating plate prior to the addition of insulation.



Figure 2. Heating Plate assembled with stainless steel housing (left), and installed in apparatus during test preparations (right).

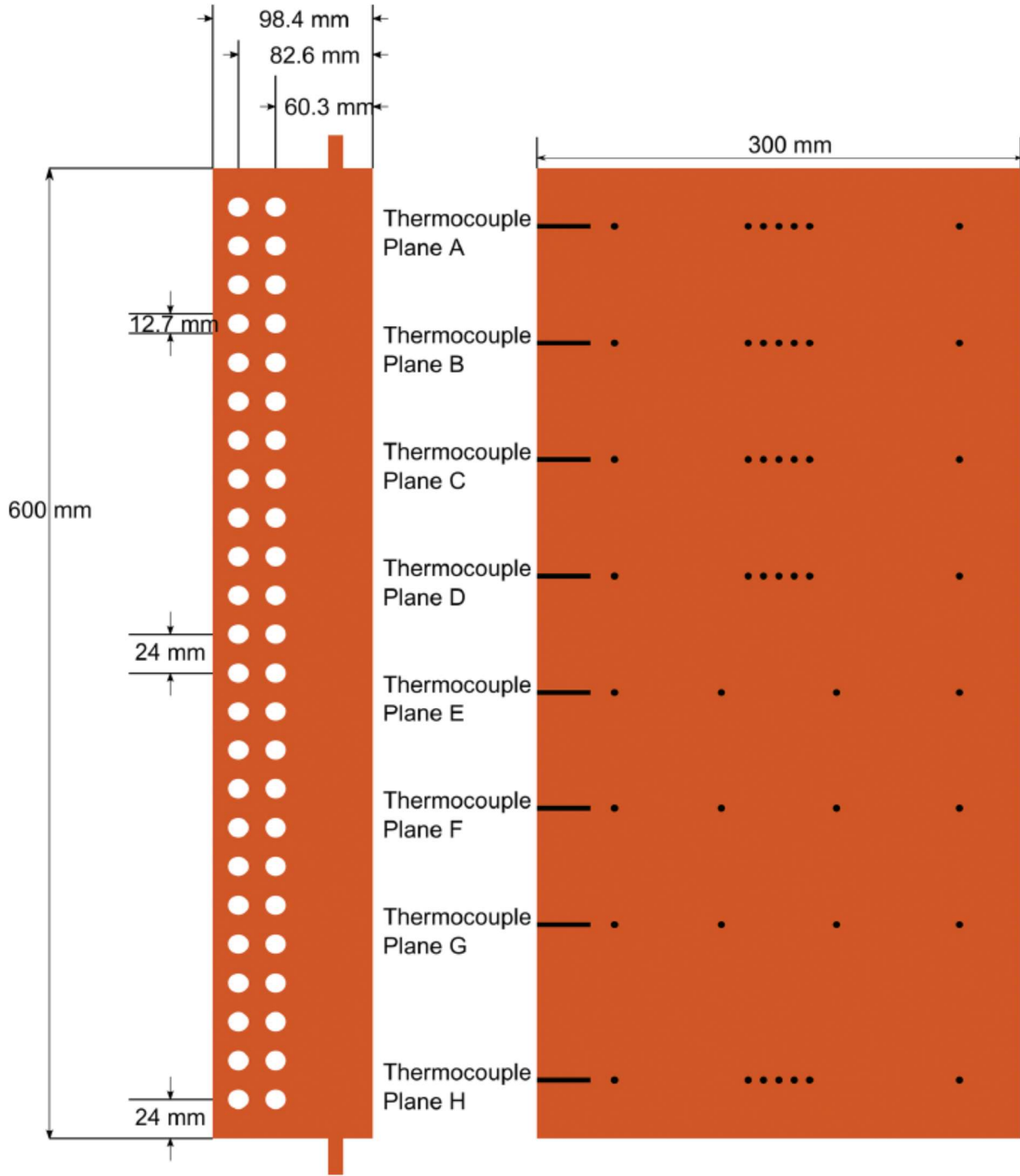


Figure 3. Heating plate geometry.

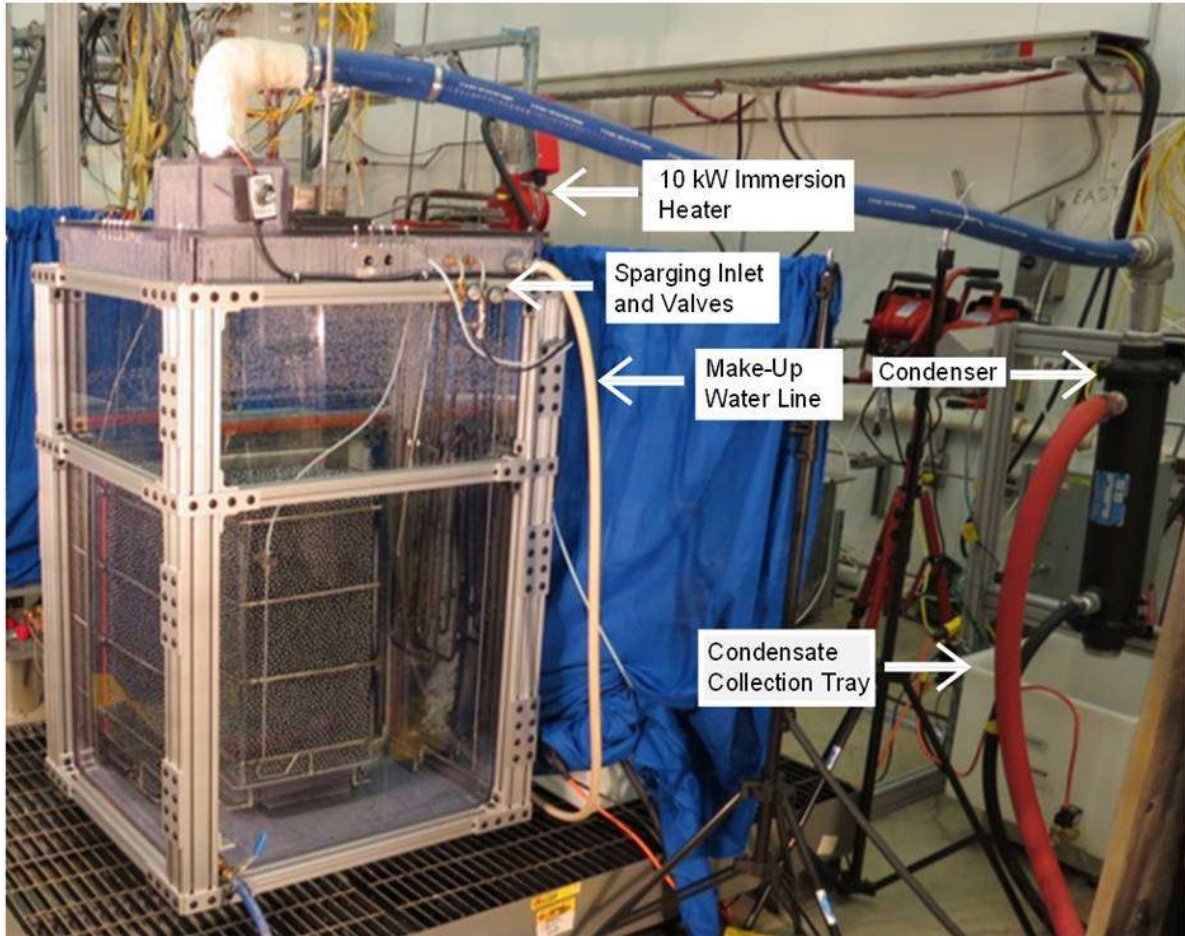


Figure 4. Secondary aspects of the experimental apparatus.

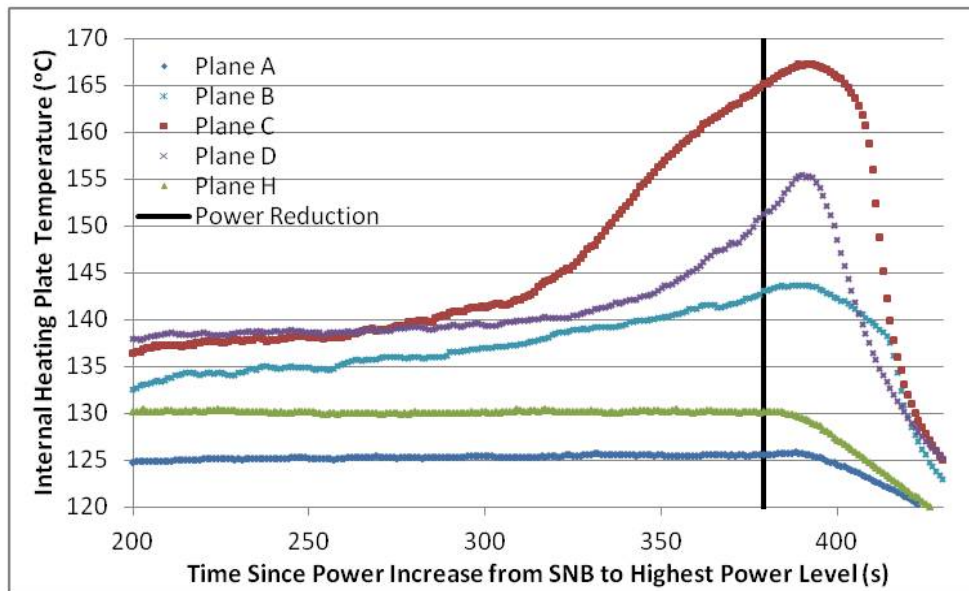


Figure 5. Thermocouple measurements during test ES-MZ-1-5 temperature transient (thermocouple planes are shown in Table 1).

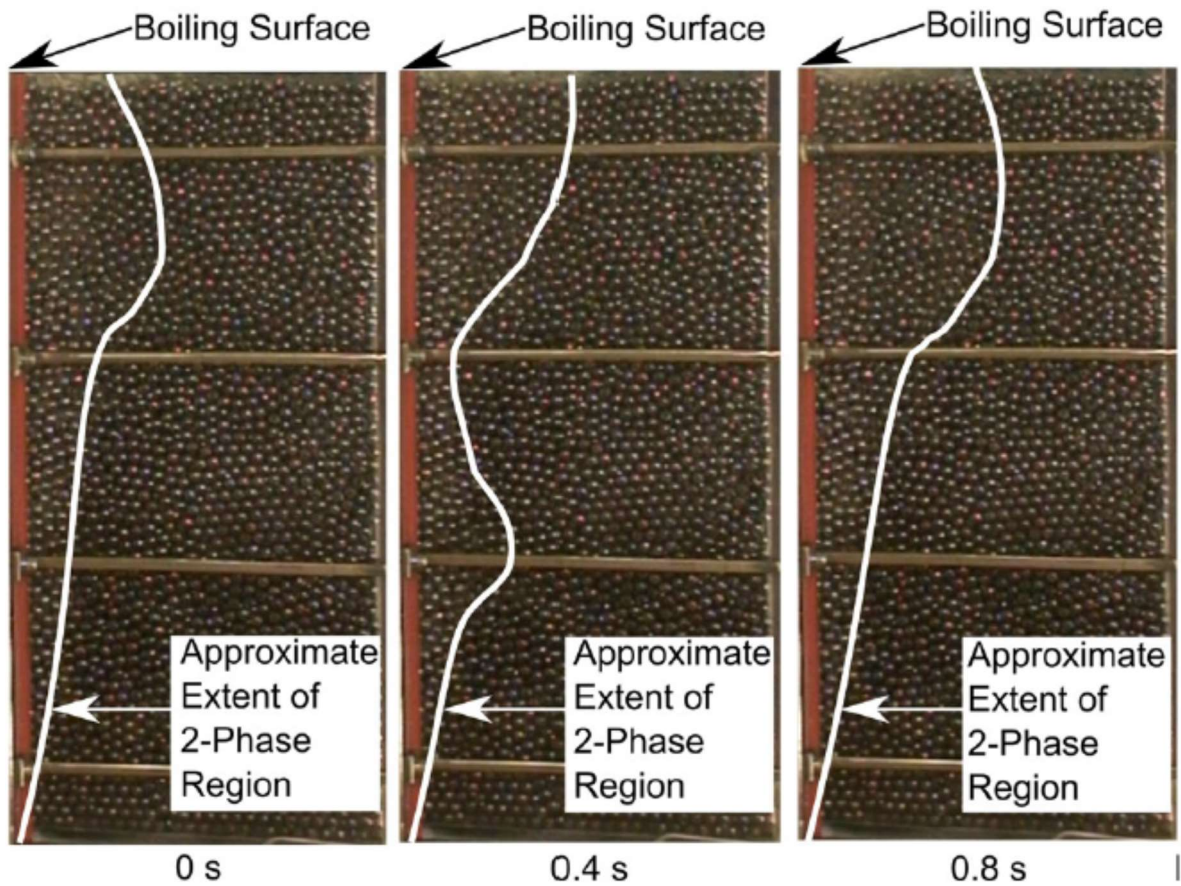


Figure 6. Side views of packed bed of steel balls during nucleate boiling at 308 kW/m<sup>2</sup>.

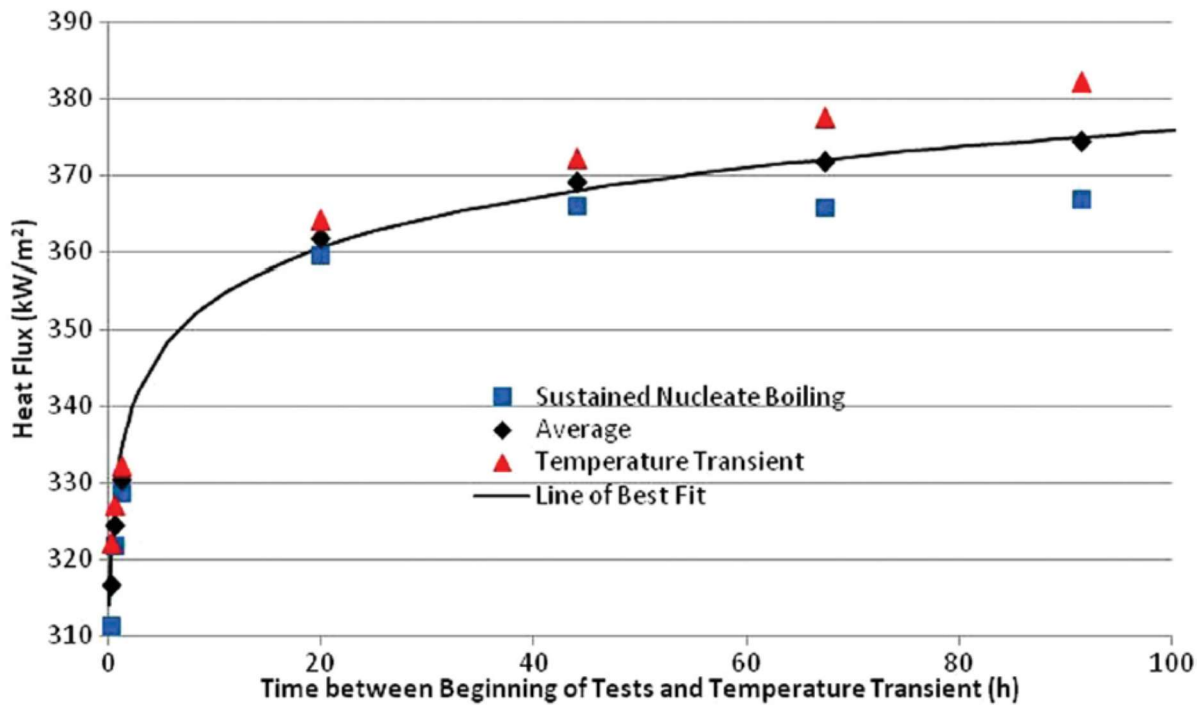


Figure 7. Surface aging impact on baseline test results.

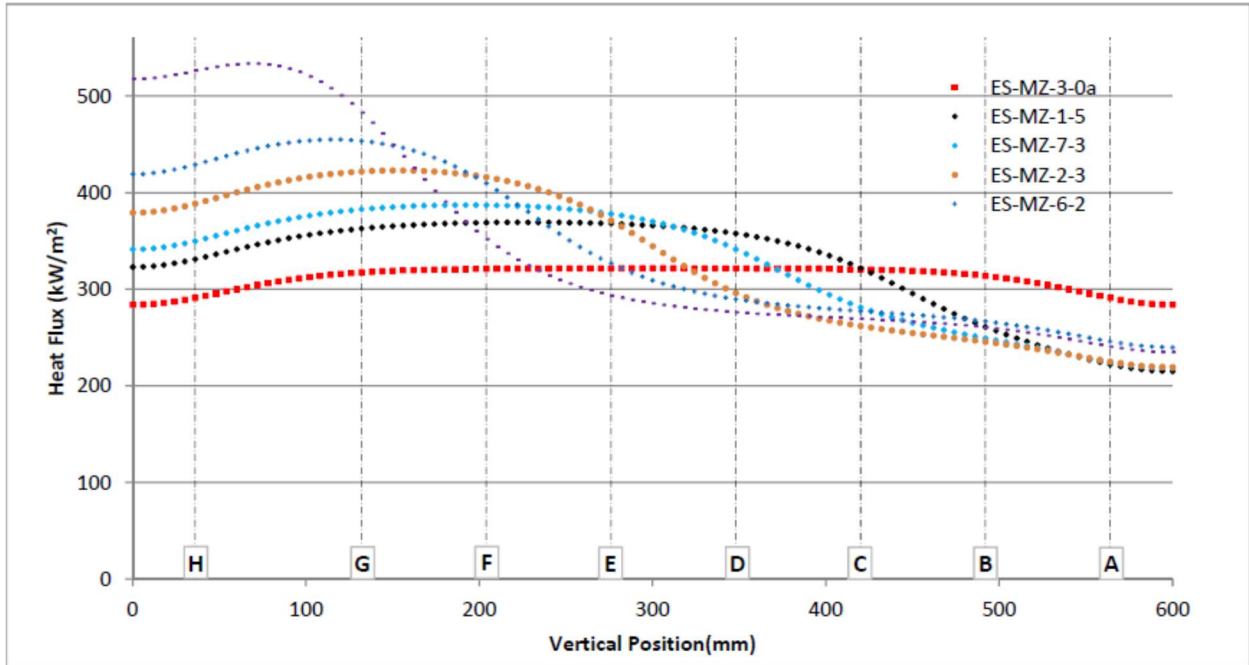


Figure 8. Aging-scaled heat flux as a function of position for sustained nucleate boiling as predicted using finite element simulations (alphabetic characters indicate the plane position given in Table 1).

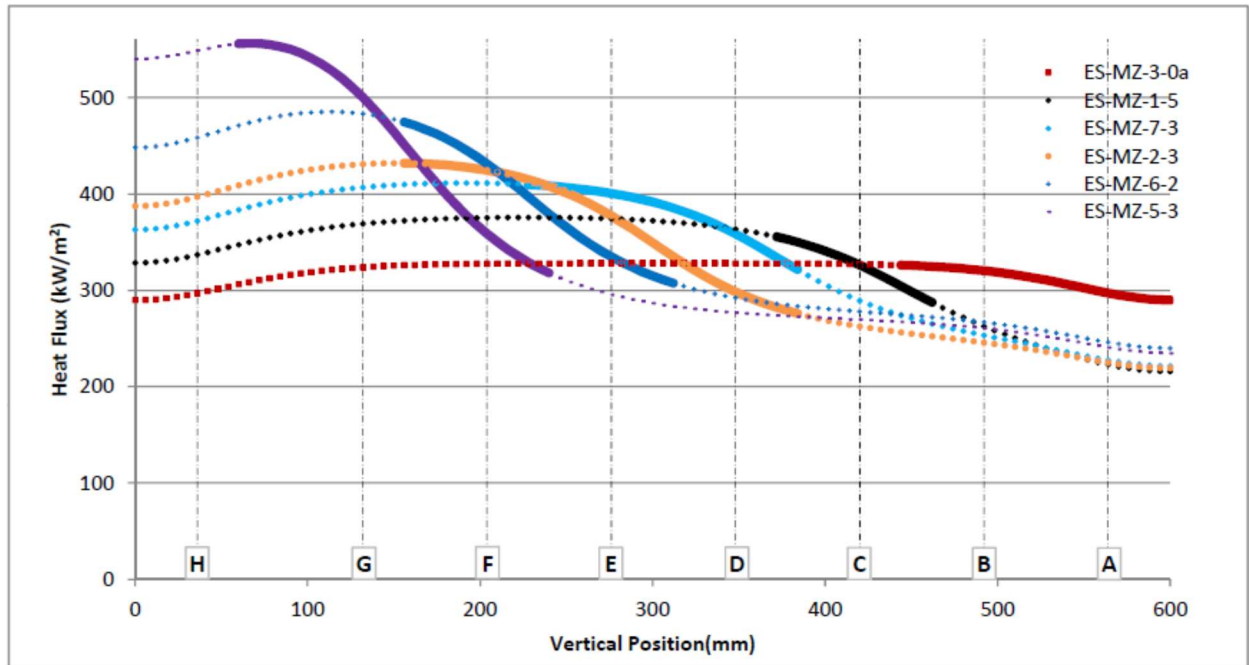


Figure 9. Aging-scaled heat flux as a function of position for temperature transient as predicted using finite element simulations (alphabetic characters indicate the plane position given in Table 1).

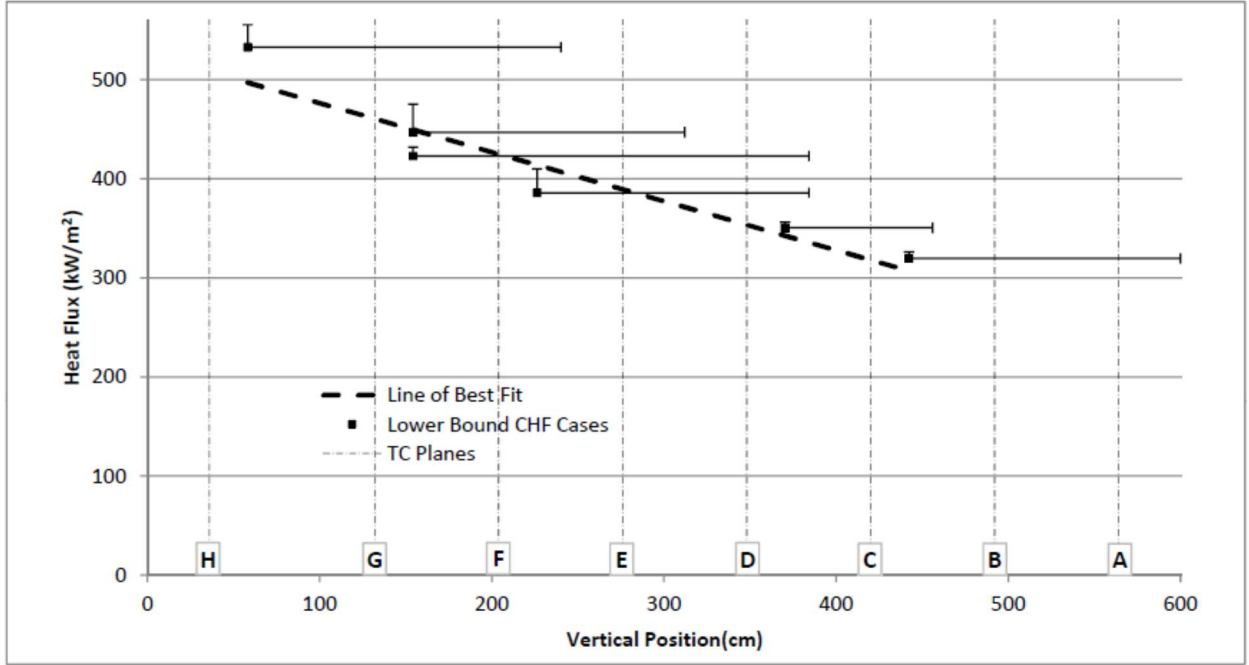


Figure 10. CHF as a function of position (alphabetic characters indicate the plane position given in Table 1).

#### 4.2.10. List of Tables

Table 1. Positions of thermocouple planes.

Thermocouple Plane	Distance from Bottom of Heating Plate (mm)
A	36
B	132
C	204
D	276
E	348
F	420
G	492
H	564

Table 2. Geometry of heating zones for each configuration.

Configuration	Position as Measured from Heating Plate Bottom (cm)					
	Zone 1		Zone 2a		Zone 2b	
	Bottom	Top	Bottom	Top	Bottom	Top
1	444	600	0	444	Not Applicable	
2	300	600	0	300		
3	300	444	0	300	444	600
3a	156	444	0	156	444	600

4	156	300	0	156	300	600
5	0	156	156	600	Not Applicable	
6	0	228	228	600		
7	0	372	372	600		

Table 3. Raw experimental results.

Test Name	Configuration	Time from Beginning of First Test (s)	q'' During Highest SNB (kW/m <sup>2</sup> )		q'' During TT (kW/m <sup>2</sup> )		Duration of Highest SNB (s)
			Zone 1	Zone 2a/2b	Zone 1	Zone 2a/2b	
ES-MZ-1-0a	1	540	311.4	323.2	322.3	336.1	229
ES-MZ-1-0b	1	1 950	321.8	337.7	327.2	343.7	238
ES-MZ-1-0c	1	5 250	328.6	347.5	332.2	352.3	268
ES-MZ-1-1	1	7 565	300.2	370.8	300.3	385.0	238
ES-MZ-1-2	1	8 240	264.7	378.1	264.7	392.3	237
ES-MZ-1-3	1	8 835	245.3	378.2	245.3	392.2	308
ES-MZ-1-4	1	9 795	244.7	385.2	244.9	392.0	239
ES-MZ-1-5	1	10 460	244.6	384.9	244.7	391.7	297
ES-MZ-1-6	1	16 150	475.0	207.7	508.9	207.6	238
ES-MZ-1-7	1	16 695	474.4	207.9	490.5	207.9	236
ES-MZ-1-8	1	17 325	473.8	208.1	490.6	208.1	294
ES-MZ-1-9	1	18 480	573.3	100.5	621.4	100.4	252
ES-MZ-1-10	1	19 230	596.5	100.4	613.0	100.5	238
ES-MZ-1-11	1	19 780	594.9	100.4	603.7	100.4	296
ES-MZ-2-0a	2	72 800	359.6	338.3	364.3	352.7	243
ES-MZ-2-1	2	74 760	276.1	472.7	276.1	512.8	262
ES-MZ-2-2	2	77 015	274.2	476.8	274.2	507.2	317
ES-MZ-2-3	2	77 690	275.4	479.5	275.4	490.1	410
ES-MZ-2-4	2	78 540	294.3	470.5	294.4	480.2	397
ES-MZ-3-0a	3	158 730	365.9	358.8	373.6	366.1	239
ES-MZ-3-1	3	163 400	680.5	208.7	726.8	208.7	364
ES-MZ-3a-1	3a	173 050	501.0	208.5	540.3	208.2	237
ES-MZ-3a-2	3a	173 310	501.1	209.3	520.8	209.2	632
ES-MZ-3a-3	3a	174 530	480.8	209.7	510.8	209.5	407
ES-MZ-3a-4	3a	175 880	540.2	100.4	560.0	100.4	257
ES-MZ-4-1	4	180 400	706.3	208.7	767.3	208.5	379
ES-MZ-5-0a	5	243 525	375.8	365.9	384.6	377.7	358
ES-MZ-5-1	5	245 740	695.8	206.1	772.6	206.1	328
ES-MZ-5-2	5	250 310	724.4	205.7	755.2	205.5	298
ES-MZ-5-3	5	252 095	707.9	305.5	740.0	305.5	237
ES-MZ-6-1	6	259 980	628.8	213.7	666.4	213.8	269
ES-MZ-6-2	6	262 795	551.9	312.3	590.9	312.3	237
ES-MZ-6-3	6	264 010	626.8	102.8	676.0	102.8	240
ES-MZ-6-4	6	265 360	212.2	404.2	212.2	429.4	299
ES-MZ-7-0a	7	330 235	381.8	366.9	398.7	382.2	392

Test Name	Config-uration	Time from Beginning of First Test (s)	q'' During Highest SNB (kW/m <sup>2</sup> )		q'' During TT (kW/m <sup>2</sup> )		Duration of Highest SNB (s)
			Zone 1	Zone 2a/2b	Zone 1	Zone 2a/2b	
ES-MZ-7-1	7	331 810	470.4	203.7	512.1	203.7	238
ES-MZ-7-2	7	333 750	503.3	100.1	520.0	100.1	388
ES-MZ-7-3	7	337 825	448.2	283.2	472.8	283.5	264
ES-MZ-7-4	7	339 175	518.6	0.0	535.1	0.0	319
ES-MZ-7-5	7	341 325	208.7	499.0	208.7	521.7	239

Table 4. Location of observed temperature transients for selected experiments.

Test Name	Thermocouple Plane(s) in which Temperature Transient was Observed
ES-MZ-3-0a	A,B
ES-MZ-1-5	C
ES-MZ-7-3	D,E
ES-MZ-2-3	D,E,F
ES-MZ-6-2	E,F
ES-MZ-5-3	F,G

## 5. Results of Air Barbotage Experiments Simulating Two-Phase Flow in a CANDU End Shield during In-Vessel Retention

### 5.1. Preface

#### 5.1.1. Citation

The paper can be cited as follows:

J. Spencer, Results of air barbotage experiments simulating two-phase flow in a CANDU end shield during in-vessel retention, ASME J. Nucl. Rad. Sci. 3(2) (2017) 1-10

#### 5.1.2. Contribution to Knowledge

The first objective of the paper was to characterize the hydrodynamics of the end shield cavity during IVR. As outlined in Table 5, this objective was approached through investigation of the following questions:

- How do vapour and liquid migrate through the porous medium (e.g. is a countercurrent flooding limit relevant to the reactor case)?
- How do near-wall hydrodynamic conditions vary as a function of relevant parameters (exiting heat flux distribution, shielding ball diameter, and elevation)?

A second objective of this paper was to determine the differences and similarities of the system's behaviour to the predictions available in the literature.

These objectives were approached through the performance of experiments making use of the air barbotage technique. This technique is well-established in the study of boiling, with pioneering application carried out by Kutateladze [68], and further use subsequently [69][70]. In this case, it facilitated visual observation of hydrodynamic conditions in the simulated end shield cavity.

Air was injected through a perforated plate representing the calandria tubesheet, into a volume representing the end shield cavity. In these experiments, the air took the place of the water vapour that would be produced on the calandria tubesheet surface during a heated test. Given the saturated temperature of water in the end shield during IVR:

- The non-condensability of the air does not constitute a significant distortion of the hydrodynamics in the porous medium, relative to the reactor case.
- The superficial velocity of air exiting the simulated calandria tubesheet can be equated to a superficial velocity of water vapour produced at the calandria tubesheet in the accident case, yielding an equivalent heat flux.

The design of the apparatus and the test conditions were influenced by practical considerations:

- The pressure in the air plenum was required to exceed a minimum value, defined as a multiple of the hydrostatic head in the simulated end shield on the other side of the perforated plate. Below this minimum value, the pressure differential across the perforated plate would vary significantly as a function of elevation, resulting in non-uniform equivalent heat flux. Some

control over the pressure differential was established using sheets of porous material attached to the plenum side of the perforated plate, affecting frictional pressure losses on the flowing air.

- The pressure in the air plenum was required to stay below a gauge pressure of 100 kPa, to conform to pressure boundary safety regulations. As with the minimum pressure, this was addressed using sheets of porous material attached to the plenum side of the perforated plate. These restrictions placed upper and lower bounds on the equivalent heat flux that could be simulated.

Variation of parameters including shielding ball diameter, equivalent heat flux, and end shield cavity dimensions permitted observation of behaviours and trends in hydrodynamic conditions. The presence of Helmholtz waves observed under all conditions was a noted commonality with related literature [45]. The thickness of the two-phase region adjacent to the wall was noted to diverge from analytical predictions of such a scenario in capillary porous media (as opposed to the more coarse medium presented by the larger shielding balls) [55],[56].

The findings presented in this paper constitute a first step toward a detailed understanding of the previously-unexamined hydrodynamic conditions in a CANDU end shield during IVR. The observations suggested future lines of enquiry, including quantification of the liquid and gas phase distribution within the two-phase region. Furthermore, the experimental technique utilized was determined to be compatible with non-invasive void fraction measurement using x-ray densitometry (with work in this area subsequently pursued [71]). These findings constitute progress toward addressing the subordinate objectives listed in Section 1.3, and the overarching objective of the thesis: the generation of a model of critical heat flux on the surface of a calandria tubesheet facing the end shield cavity during IVR in a CANDU reactor.

### 5.1.3. Author's Contribution to Paper

The author led the design process of the apparatus presented in the paper. Following manufacturing of the components by various suppliers, the author directed AECL technologists in the assembly and preparation of the apparatus. Performance of the experiments was led by the author, with assistance provided by an AECL technologist. Finally, analysis of the experimental data and preparation of the paper was carried out by the author.

## 5.2. Publication

### 5.2.1. Abstract

This paper presents the results of experimental investigations into two-phase mass transport in a coarse packed bed representing the CANDU end shield. This work contributes to understanding of phenomena impacting in-vessel retention during postulated severe accidents in CANDU reactors. The air barbotage technique was used to represent boiling at the calandria tubesheet surface facing the inner cavity of the end shield. Qualitative observations of the near-wall two-phase region were made during air injection. In addition, flow visualization was carried out through the addition of dye to the water. Air flow rate, shielding ball diameter, and cavity dimensions were varied within relevant ranges; and the impact of these parameters on the near-wall region was identified. A brief review of the relevant knowledge base is presented, allowing demonstration of the applicability of the test parameters. The observed phenomena are compared to published results involving similar geometries with capillary porous media.

### 5.2.2. Introduction

CANDU reactors (Figure 1) have a structure significantly different from that of other reactor designs, with the result that the progression of postulated severe accidents follows a distinct course. During a representative sequence such as Station Black Out (SBO), loss of coolant from the primary heat transport system along with loss of the moderator cooling system could lead to core heat-up, moderator boiling, and uncovering of the outside of the fuel channels [1-3]. Within several hours, dropping moderator levels and progressive heat-up of the fuel channels would result in disassembly and core collapse, involving relocation of debris comprising the contents of the core to the bottom of the calandria vessel, forming a Terminal Debris Bed (TDB). At this point, it would be desirable to arrest progression of the accident by retaining the resulting 'corium' material in the calandria vessel – referred to as 'In-Vessel Retention' (IVR). IVR would avoid ex-vessel phenomena with high uncertainties and the potential to challenge containment integrity; for example, ex vessel Molten Fuel Coolant Interaction (MFCI) and Molten Core – Concrete Interaction (MCCI). Assessing the consequences of postulated severe accidents in CANDU reactors thus demands an ability to assess the likelihood of successful IVR.

Several physical phenomena have the potential to decisively impact the success of IVR. For example, IVR is conditional upon the effective heat removal from the stainless steel walls forming the boundaries of the calandria vessel (CV). Nucleate boiling presents an efficient heat transport pathway from the CV walls to the surrounding shield water. This boiling regime cannot be sustained above a limit known as the Critical Heat Flux (CHF). Flow of heat through the CV walls at a magnitude greater than the CHF would lead to a dramatic shift in boiling regime referred to as a Boiling Crisis (BC), followed by a temperature escalation and potentially loss of CV wall integrity and IVR.

The main boundaries constituting the CV walls are the cylindrical shell and the two calandria tubesheets (Figure 1) which separate the CV from the end shields. The end shields are packed with steel 'shielding balls', which attenuate the radiation fields in the adjacent areas. CHF in geometries resembling the cylindrical shell has been studied as part of investigations of IVR in the light water reactor (LWR) community [4-15]. In contrast, significant scrutiny has only recently fallen upon CHF in geometries analogous to the surface of the calandria tubesheet facing the coarse porous medium constituted by shielding balls of the end shield [16].

While recent investigations have experimentally measured CHF in a geometry representative of the CANDU end shield [16], a more comprehensive understanding of relevant phenomena requires further

investigation. This paper presents the results of such efforts. Boiling at the calandria tubesheet surface facing the inner cavity of the end shield was represented through the air barbotage technique. The experimental apparatus was constructed in a manner allowing for observation of the near-wall two-phase region. Air flow rate (proportional to heat flux) and shielding ball diameter were varied within relevant ranges; and the impact of these parameters on the near-wall region was identified. The thickness of the shielding ball and water-filled volume (representing the distance between the calandria and fuelling tubesheets) was varied to allow for observation of the impact of this scaling parameter. Finally, flow visualization was carried out through the addition of water-soluble dye to the water.

This work is focussed primarily on the qualitative identification of phenomena, along with identification of trends in behaviour. This approach to investigating end shield heat and mass transport is consistent with Novak Zuber's hierarchical, two-tiered scaling analysis methodology [17]; which directs that in situations where large uncertainties in relevant phenomena exist, exploratory experiments are called for. These allow for examination of key parameters, and ultimately inform scaling of integrated experiments.

### 5.2.3. Background

#### 5.2.3.1. In-Vessel Retention in CANDU Reactors

As outlined above, a postulated severe accident sequence such as Station Black Out (SBO) is expected to lead to core heat-up, moderator boiling, and uncovering of the outside of the fuel channels [1-3]. In the absence of any mitigating actions, for a CANDU 6 reactor this would lead to the commencement of core disassembly after 5.5 hours, core collapse (with formation of the TDB), and exhaustion of all liquid moderator in the calandria vessel after 11 hours.

Following the compaction associated with liquefaction of the centre of the TDB, it is expected that there will be contact between a solid crust surrounding the liquid core, and approximately the bottom 60 cm of the calandria tubesheet. Convection within the liquid portion will result in spatially varying heat fluxes delivered to the boundaries of the calandria vessel. Radiation from the upper crust of the corium pool is expected to transport approximately 70% of the heat load to the relatively large surface area represented by the upper portions of the calandria vessel [1]. The remaining 30% would be delivered to the areas in contact with the crust.

The knowledge base relating to convecting pools in the calandria vessel relevant geometry at this time is not sufficiently developed to allow for confident prediction of the spatial distribution of this heat load. Further complicating the matter of establishing relevant heat loads is uncertainty over Fission Product (FP) releases prior to formation of the TDB. FP releases are significantly impacted by factors including: the quantity of debris suspended above the moderator during core disassembly, the debris' temperature, and the length of time that it is suspended. Despite these uncertainties, it is contextually valuable to establish an approximate value to aid in interpretation of the test results – Luxat and Luxat [18] predicted a spatially averaged heat flux through the contact areas of  $140 \text{ kW/m}^2$ .

This paper focuses on heat transfer through the calandria tubesheet, to the end shield cavity. This is a volume filled with a random packing of shielding balls of uniform size, and light water. In CANDU 6 reactors, the shielding balls may have diameters between 9.5 mm and 12.7 mm. Work has recently begun studying CHF in this geometry in recognition of the large uncertainties previously associated with this critical value, and the potential decisive threat to IVR should CHF be exceeded.

### 5.2.3.2. Knowledge Base Relevant to Heat Transport from the Calandria Tubesheet to the End Shield

Boiling has been studied extensively in geometries peripherally relevant to the end shield cavity, including unobstructed, vertically oriented surfaces. Unfortunately, the presence of the shielding balls introduces a great deal of uncertainty to predictions of important parameters, including CHF. Prior to recent efforts at Canadian Nuclear Laboratories (CNL), the most applicable results were from studies of vertically oriented heating surfaces abutting a water-saturated capillary porous medium.

Early studies in this area were carried out by Parmentier [19], and continued by Cheng and Verma [20]. This work assumed that the free volume in the near wall region was entirely occupied by vapour – a scenario of limited relevance to the focus of this paper.

Further efforts were made by Wang and Beckerman [21], who assumed a two-phase region near the heated surfaces. Important features of this work are that a Darcian flow regime and strong capillary forces are assumed. The two-phase region was predicted to exhibit a parabolic profile.

The most applicable work to date has been carried out recently at CNL [16]. Experiments were performed measuring CHF in an experimental apparatus representing a CANDU end shield. The heating surface height was 60 cm and the shielding balls were 11.1 mm in diameter. For relevant heating surface heights, CHF was found to be roughly in the range of 300 to 400 kW/m<sup>2</sup>.

### 5.2.4. Experimental Apparatus and Procedure

#### 5.2.4.1. Air Barbotage

Air barbotage is a well established approach to simulating boiling, forming a key portion of pioneering work by Kutateladze [22]. Since then, the technique has been exploited for investigation of several scenarios [23-24].

Air barbotage involves injection of air through a perforated surface, simulating departure of vapour from a heated surface. Given that the specific volumes of water vapour and liquid differ by three orders of magnitude near atmospheric pressure, the volumetric fluxes of each phase toward and away from the perforated surface are nearly identical to those expected for an equivalent heating surface. Additionally, condensation of vapour at locations removed from the boiling surface does not occur during saturated boiling.

The scaling parameters of primary importance between the boiling case and the air barbotage case are thus the properties of the fluids in question, specifically density, viscosity, and surface tension, in addition to contact angle with the shielding balls. The magnitude of these effects can be quickly assessed by considering the large size of the shielding balls and the vigorous flow through the packed bed. Under these conditions:

- Capillary forces are inconsequential, rendering surface tension and contact angle unimportant;
- Frictional resistance to flow through the packed bed is proportional to the density of the fluid, with the viscosity rendered unimportant;
- At atmospheric pressure, the ratio of the densities of water vapour to liquid at atmospheric pressure is very close to the ratio of air to water; and

- Although bubble departure from perforated sheet may not be entirely representative of bubble departure from a boiling surface, it is expected that bubble coalescence in the packed bed would render the impact of this effect on overall two-phase region behaviour insignificant.

For this application, the barbotage approach can thus be considered a good representation of the boiling case.

Finally, the equivalence between vapour production at the calandria tubesheet during boiling in an end shield and air flow in the barbotage simulation can be expressed as shown in Equation 1:

$$A'' = q''v / h_{lv} \quad (1)$$

Where:

- $A''$  is the volumetric air flux [m/s]
- $q''$  is the heat flux [ $W/m^2$ ]
- $v$  is the specific volume of water vapour [ $m^3/kg$ ]
- $h_{lv}$  is the latent heat of vapourization of water [J/kg]

#### 5.2.4.2. Experimental Apparatus

The experimental apparatus is constructed in such a manner that a cavity filled with shielding balls and water abuts a perforated vertical surface, through which air can be injected (Figure 2). Air is injected into a plenum on the opposite side of the perforated plate from the cavity, which reaches a pressure somewhat higher than that in the cavity. The perforated plate separating the cavity from the plenum is 432 mm tall and 102 mm wide. The apparatus thus simulates boiling on the lowest 432 mm of the calandria tubesheet surface facing the end shield cavity. Variation in porosity of the packed bed across the 102 mm width of the cavity, as well as frictional drag along the walls can be expected to have some impact on convection; however, this effect is judged to be inconsequential in use of the apparatus for the identification of trends and phenomena.

In tests where shielding balls are used, they are poured into the cavity from above, achieving random packing. A screen is then pressed against the top of the packed bed to prevent fluidization at high simulated heat fluxes. The thickness of the cavity can be reduced by inserting a structure separating the cavity into a portion adjacent to the perforated plate, and a portion farther from it. This measure allows for simulation of boiling in an end shield where the distance from the calandria tubesheet to the fuelling tubesheet is reduced.

Observations made during initial tests indicated the need for additional measures to ensure that the pressure in the plenum significantly exceeds that in the cavity, minimizing the impact of the differential hydrostatic head between the top and bottom of the perforated plate (approximately 4 kPa). The implementation of such measures ensures that air flowing through the perforated plate does not vary significantly with elevation. In order to ensure the validity of tests, the pressure in the plenum is measured during tests using an analog pressure gauge with an uncertainty of 3 kPa.

A simple calculation allows for conversion between the measured volumetric flow rate of air and the equivalent heat flux (Equation 2).

$$A = A''a = a q''v / h_{lv} \quad (2)$$

Where 'a' is the area over which air is injected.

Air flow into the plenum is measured using a rotameter with an uncertainty of +/-0.24 l/s. This yields an uncertainty of 7.5 kW/m<sup>2</sup> in equivalent heat flux.

While the main structure of the apparatus is composed of aluminium, the sides are sealed with transparent acrylic walls, and the shielding balls are composed of the same material. These measures facilitate visual observation during tests.

#### 5.2.4.3. Test Procedure and Conditions

Tests are run by injecting air into the plenum at a constant rate. Aside from the test conditions, the primary data collected during these experiments is in the form of videography. Each test is sustained with constant parameters for a minimum of 15 seconds, with the system reaching a quasi-steady end state within approximately 1 second.

A variety of test conditions were investigated:

- Tests with and without shielding balls were performed;
- Shielding balls of three different diameters were used (9.5 mm, 11.1 mm, and 12.7 mm), representing the range allowable in the CANDU end shield;
- Air flow rates were varied between the minimum value resulting in sufficient pressure drop (121 kW/m<sup>2</sup> equivalent), and the maximum attainable given the configuration of our facility (326 kW/m<sup>2</sup> equivalent); and
- The thickness of the cavity was varied, to investigate the impact of this potentially important scaling parameter.

#### 5.2.5. Results

##### 5.2.5.1. No Shielding Balls

Although the phenomenon of pool boiling on a vertical heated surface has been studied extensively, this scenario is simulated using the apparatus with no shielding balls in place in order to establish a baseline for determination of impact of the balls.

Howard and Mudawar established that for vertical surfaces subject to high heat flux, vapour tends to form Helmholtz waves that sweep along the surface [25] (Figure 3). While the vertical surface in the present experiments is significantly taller than that studied by Howard and Mudawar, a qualitatively similar phenomenon can be observed on a larger scale (Figure 4). The presence of a wavy interface between the two-phase near wall region and the single-phase liquid in the far field is apparent; however, the physical scale of the waves is significantly larger than that observed with shorter, heated surfaces.

Qualitatively, the near-wall region is highly turbulent and characterized by a churning-type flow. Both the turbulence and the thickness of the two-phase region increase with air flow rate.

#### 5.2.5.2. 9.5 mm Shielding Balls

Tests using shielding balls with a diameter of 9.5 mm (the smallest used in CANDU end shields) demonstrated some qualitative similarities to tests with no shielding balls (Figure 5). In particular, a wavy interface between the two-phase near wall region and the single-phase liquid are observed. The two-phase layer thickness increases with equivalent heat flux, and is thicker than that observed for equivalent heat fluxes in the absence of shielding balls; a result that is expected given the reduced free volume and increased flow resistance.

In recognition of the time-dependent behaviour of the system, video of the tests was analyzed to determine the minimum and maximum thickness of the two-phase region. 10 second intervals were studied, with the minimum and maximum thickness observed during the interval recorded for four different elevations: 9 cm, 18 cm, 27 cm, and 36 cm. Due to the churning behaviour of the near-wall region and refraction associated with the shielding balls, identification of maximum and minimum extents of the two-phase region is somewhat subjective, and is subject to an error of approximately +/- 10 mm. Both minimum and maximum thicknesses appear to increase approximately linearly with respect to elevation within the range considered in the experiment (Figure 6, Figure 7). Finally, both values increase with equivalent heat flux at a given elevation (Figure 8, Figure 9).

#### 5.2.5.3. 11.1 mm Shielding Balls

Behaviour observed in tests with shielding balls of diameter 11.1 mm was effectively indistinguishable from that observed with 9.5 mm balls. The two-phase region forms a wavy interface with the single phase region, with a thickness increasing with equivalent heat flux (Figure 10). The minimum and maximum thicknesses of the two-phase region increase with equivalent heat flux (Figure 11, Figure 12).

#### 5.2.5.4. 12.7 mm Shielding Balls

As was the case with the 11.1 mm shielding ball case, the behaviour observed in tests with 12.7 mm balls (the largest used in CANDU end shields) was effectively indistinguishable from that observed with 9.5 mm balls. Interface waviness (Figure 13) and the relation between two-phase region thickness and effective heat flux (Figure 14, Figure 15) are as observed with the other ball sizes.

#### 5.2.5.5. Impact of Shielding Ball Sizes

Comparisons were made between the thickness of the two-phase region for 9.5 mm, 11.1 mm, and 12.7 mm ball sizes. No noteworthy impact on either the minima or maxima of two-phase region thickness was observed.

#### 5.2.5.6. Cavity Thickness

One parameter with the potential to impact scaling between experimental results and the reactor case is the cavity thickness representing the distance between the calandria and fuelling tubesheets. This parameter was studied by inserting a structure into the cavity, which isolates the portion of the cavity nearest the wall from the remainder. With the cavity thickness reduced to 197 mm (producing an aspect ratio of approximately 2:1 between the cavity height and thickness), the extent of the two-phase region appears unaffected (Figure 16).

With the cavity thickness reduced to 96 mm (producing an aspect ratio of approximately 4:1), the two-phase region reaches the outer edge of the free volume, and is constrained (Figure 17). Extrapolation of these results from the small-scale apparatus to the reactor case must be approached with caution. With that said, a rising vapour plume spanning from calandria tubesheet to fuelling tubesheet would have the

potential to inhibit the downward flow of liquid. Such an effect could potentially lead to transient exhaustion of liquid in the bottom portion of the end shield if the countercurrent flooding limit is exceeded. While the large ratio of height to thickness in the reactor case (the ratio for CANDU 6 design is 8.6) suggests further consideration of this possibility, a likely mitigating factor is the significantly reduced heat flux at elevations above the bottom 60 cm of the end shield.

#### 5.2.5.7. Flow Visualization

In order to develop understanding of flow patterns in the single-phase liquid region, a flow visualization test was carried out through the addition of a water-soluble dye to the water while air was injected at a rate corresponding to a heat flux of approximately  $200 \text{ kW/m}^2$  (Figure 18). The sluggish flow of the dye in the single-phase water region demonstrates the contrast between velocities in the two-phase and single phase regions, with the rapidly rising two-phase region driving a slow downward flow of liquid in the single phase region. The dye does not follow a tight streamline as it travels away from the point of injection demonstrating the diffusive impact of the shielding balls on flowing fluids. Finally, once the dye reaches the edge of the two-phase region (at approximately 20 s), it can be seen to enter the two-phase region through a process of lateral entrainment - although the presence of the dye is not as obvious as in the single-phase region due to dilution and the relatively low liquid saturation in the region. This flow pattern appears to qualitatively confirm some the relevant predictions of the Wang and Beckerman model [21].

#### 5.2.6. Discussion

Several qualitative observations made in the previous section warrant further discussion. These results are all new additions to the knowledge base, given the relatively undeveloped nature of investigations into the phenomenon of boiling in the CANDU end shield under severe accident conditions.

The appearance of Helmholtz waves in both cases with and without shielding balls is noteworthy. It appears that the wavelength differs significantly between the two cases. In the case of unobstructed vertical surfaces, Helmholtz waves are an important mechanism in the CHF phenomenon [25]. It is possible that these waves may be associated with CHF in the end shield. Further work is called for to understand this issue.

The lack of sensitivity of the results to ball sizes is an important result. The possibility exists for CHF in the end shield geometry to be sensitive to ball size through several mechanisms including the impact on vapour transport. This demonstration that vapour transport is relatively insensitive to this parameter within the relevant range supports the broad applicability of recent CHF investigations at CNL [16].

The approximately linear relationship between thickness of two-phase region and elevation observed in these tests does not align with the parabolic two-phase region predicted in work on capillary porous media. However, in light of the significant differences between the systems that were considered analytically and the experimental apparatus, this divergence in results is not surprising. It is also possible that the approximately linear region observed in the tests constitutes the bottom portion of a parabola that would become apparent given a larger apparatus.

While observations of the interface between the two-phase near wall region and the single-phase far field are valuable, further work is suggested to measure saturation of the porous medium as a function of elevation, distance from the heating surface (or porous plate), and heat flux (or air flow rate). Such work could be carried out using an apparatus such as that described in this work, combined with a non-invasive void fraction technique such as x-ray densitometry.

Tests of the impact of cavity thickness suggest that further work may be called for investigating the potential for exceedance of the counter-current flooding limit in the end shields during an accident.

Finally, lateral entrainment of liquid into the two-phase region should be expected due to the diffusive effect of the shielding balls, but verification of this phenomenon is important in understanding how water would be supplied to the calandria tubesheet during boiling in the end shield. Further investigation of this effect, possibly quantifying the mixing, would be valuable. In earlier analytical studies involving capillary porous media [21], liquid was transported from the single-phase liquid region to the heating surface through capillary action. Since capillary forces are insignificant in the end shield porous medium, a similar mathematical treatment of the system could exploit this observed lateral entrainment effect as an alternate mechanism.

### 5.2.7. Summary

This paper presents the results of a series of air barbotage experiments, simulating boiling in the CANDU end shield under severe accident conditions. The interface between the two-phase region near the wall and the single-phase liquid region in the far field was observed, and sensitivity of the system's behaviour to several parameters was investigated, including: equivalent heat flux, shielding ball diameter, and cavity thickness. Finally, flow visualization was carried out through the addition of water-soluble dye to the water.

Several key observations were made:

- Helmholtz waves form without shielding balls, with shielding balls of all diameters, and at all equivalent heat fluxes studied;
- Within the range studied, shielding ball diameter does not significantly impact the thickness of the two-phase region;
- The thickness of the two-phase region grows approximately linearly with elevation;
- At a given elevation, the thickness of the two-phase region grows with equivalent heat flux;
- Lateral entrainment of water into the two-phase region was observed; and
- If the cavity is made sufficiently narrow, the two-phase region may span it entirely, raising the possibility of a counter-current-flooding-limited dryout of the bottom region of the end shield.

By qualitatively investigating behaviours and trends in a separate effects manner, this paper is intended to improve the nascent knowledge base pertaining to CHF in CANDU end shields. The findings presented in this paper suggest future lines of enquiry, including:

- The formation of Helmholtz waves at the interface between the two-phase and single-phase regions;
- Saturation within the two-phase region as a function of elevation, distance from the vertical heating surface, and effective heat flux; and
- The potential for exceedance of the counter-current flooding limit by vapour rising in the end shields during an accident.

## 5.2.8. Nomenclature

### Acronyms

BC	Boiling Crisis
CANDU	CANada Deuterium Uranium
CHF	Critical Heat Flux
CNL	Canadian Nuclear Laboratories
FP	Fission Product
IVR	In Vessel Retention
LWR	Light Water Reactor
MCCI	Molten Core Concrete Interaction
MFCI	Molten Fuel Coolant Interaction
TDB	Terminal Debris Bed

### Variables

a	Area of Air Injection Surface
A	Total Volumetric Air Flow Rate
A''	Volumetric Air Flux
h	Latent Heat of Vapourization
q''	Heat Flux
v	Specific Volume

### Subscripts

l	Liquid
v	Vapour

## 5.2.9. References

1. D.A. Meneley, C. Blahnik, J.T. Rogers, V.G. Snell and S. Nijhawan, "Coolability of Severely Degraded CANDU Cores", AECL report number AECL-11110, 1996
2. J.C. Luxat, "Thermal-Hydraulic Aspects of Progression to Severe Accidents in CANDU Reactors", Nuclear Technology, 2009 July
3. T. Nitheanandan and M.J. Brown, "Backup and Ultimate Heat Sinks in CANDU Reactors for Prolonged SBO Accidents", Nuclear Engineering and Technology, Vol. 45, No. 5, 2013 October

4. T.G. Theofanous, S. Syri, T. Salmassi, O. Kymalainen and H. Tuomisto, Critical heat flux through curved, downward facing, thick walls, *Nuclear Engineering and Design* 151 (1994) 247-258
5. T.G. Theofanous and S. Syri, The Coolability Limits of a Lower Reactor Pressure Vessel Lower Head, *Nuclear Engineering and Design* 169 (1997) 59-76
6. S. Angelini, J.P. Tu, Yu.A. Buyevich and T.G. Theofanous, The mechanism and prediction of critical heat flux in inverted geometries, *Nuclear Engineering and Design* 200 (2000) 83-94
7. J. Yang, F.B. Cheung, J.L. Rempe, K.Y. Suh and S.B. Kim, Correlations of Nucleate Boiling Heat Transfer and Critical Heat Flux for External Reactor Vessel Cooling, *ASME Summer Heat Transfer Conference*, San Francisco, CA, 2005 July 17-22
8. J. Yang, M.B. Dizon, F.B. Cheung, J.L. Rempe, K.Y. Suh and S.B. Kim, CHF enhancement by vessel coating for external reactor vessel cooling, *Nuclear Engineering and Design* 236 (2006) 1089-1098
9. T.G. Theofanous, C. Liu, S. Additon, S. Angelini, O. Kymalainen and T. Salmassi, In vessel coolability and retention of a core melt, *Nuclear Engineering and Design* 169 (1997) 1-48
10. O. Kymalainen, H. Tuomisto and T.G. Theofanous, In-vessel retention of corium at the Loviisa plant, *Nuclear Engineering and Design* 169 (1997) 109-130
11. S.W. Nob and K.Y. Suh, Critical heat flux for APR 1400 lower head vessel during a severe accident, *Nuclear Engineering and Design* 258 (2013) 116-129
12. T.Y. Chu, J.H. Bentz and R.B. Simpson, Observation of the boiling process from a large downward facing torispherical surface, *Proceeding of National Heat Transfer Conference*, American Nuclear Society, Portland, OR, USA, 1995 August 5–9
13. T.Y. Chu, B.L. Bainbridge, R.B. Simpson and J.H. Bentz, Ex-vessel boiling experiments: laboratory and reactor-scale testing of the flooded cavity concept for in-vessel core retention. *Nucl. Eng. Des.* 169 (1997), 77–88
14. S. Rouge, SULTAN test facility for large-scale vessel coolability in natural convection at low pressure, *Nucl. Eng. Des.* 169 (1997), 185–195
15. Y.H. Jeong and S.H. Chang, Critical Heat Flux Experiments on the Reactor Vessel Wall Using 2-D Slice Test Section, *Nuclear Technology*, 152, 2, 162-169, 2005 November
16. J. Spencer, “Measurement of Critical Heat Flux in a CANDU End Shield Consisting of a Vertical Surface Abutting a Packed Bed of Steel Shielding Balls”, *AECL Nuclear Review – In-Press*, 2016
17. N. Zuber, Hierarchical, Two-Tiered Scaling Analysis, An Integrated Structure and Scaling Methodology for Severe Accident Technical Issue Resolution: Appendix D, U.S. Nuclear Regulatory Commission, Washington, D.C. 20555, NUREG/CR-5809, 1991 November
18. D.L. Luxat, J.C. Luxat, “Calandria vessel integrity under severe accident loads”, *Transactions of SMiRT*, J07/2, 2007
19. E.M. Parmentier, “Two-phase natural convection adjacent to a vertical heated surface in a permeable medium”, *Int. J. Heat Mass Transfer*, 22, pp. 849-855, 1979
20. P. Cheng and A.K. Verma, “The effect of subcooled liquid on film boiling about a vertical heated surface in a porous medium”, *Int. J. Heat Mass Transfer*, 24, pp. 1151-1160, 1981
21. C.Y. Wang and C. Beckermann, “Boundary-layer analysis of buoyancy-driven two-phase flow in capillary porous media”, *J. Heat Transfer*, 117, pp. 1082-1087, 1995
22. S.S. Kutateladze and V.N. Moskvicheva, “Hydrodynamics of a Two-Component Layer as Related to the Theory of Crises in the Process of Boiling”, *Soviet Technical Physics*, Vol. 4, No. 12, 1960 June
23. S. Narayanaswamy, “Bubble Dynamics in Barbotage and Boiling”, Thesis (Masters of Science), University of Manitoba, 1973 February
24. P.Y.J. Chan, “Bubble Dynamics in Combined Constant-Flow and Constant-Pressure Barbotage”, Thesis (Masters of Science), University of Manitoba, 1985 September
25. A.H. Howard and I. Mudawar, Orientation effects on pool boiling critical heat flux (CHF) and modeling of CHF for near-vertical surfaces, *Int. J. Heat Mass Transfer* 42, pp. 1665-1688, 1999

26. D.A. Meneley and Y.Q. Ruan, “Introduction to CANDU 6 - Part 1 Comparison of PHWR and PWR”, Overheads for a course presented at Xi'an Jiaotong University, 1998 September 22–25

5.2.10. List of Figures

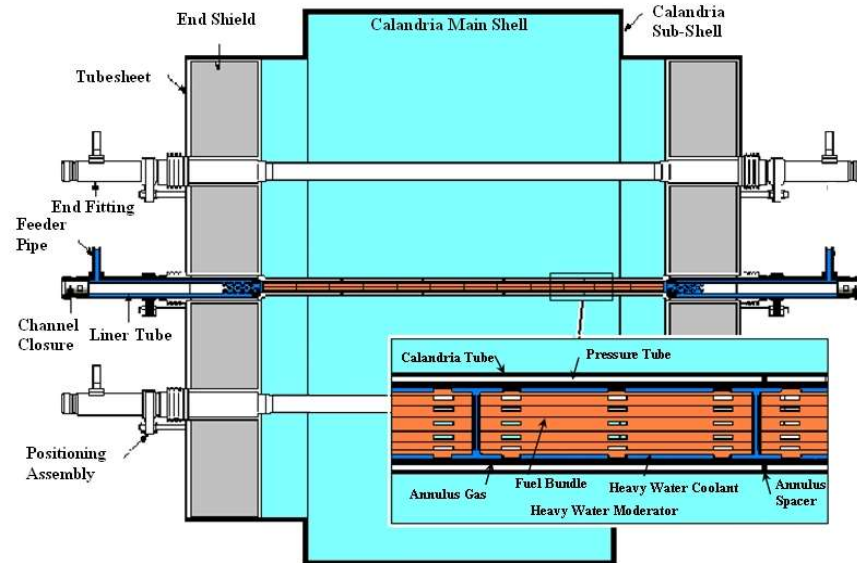


Figure 1. CANDU Reactor Core (Reproduced from Meneley et al. [26])

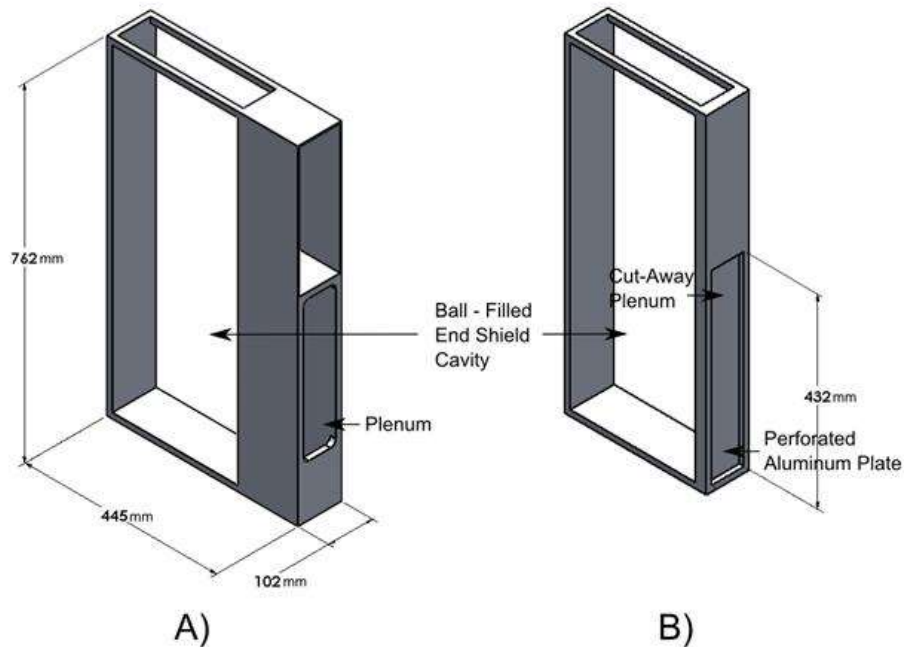


Figure 2. Experimental Apparatus – A) Full Apparatus Frame, B) Cutaway View

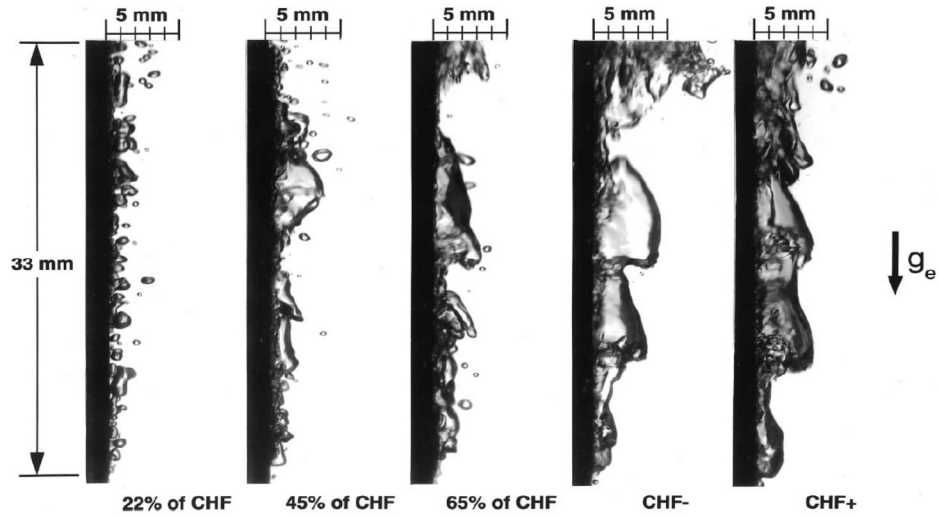


Figure 3. Pool Boiling Photographs at Increasing Heat Fluxes for a Thin, Vertically Oriented Heater (Reproduced from Howard et al. [25])

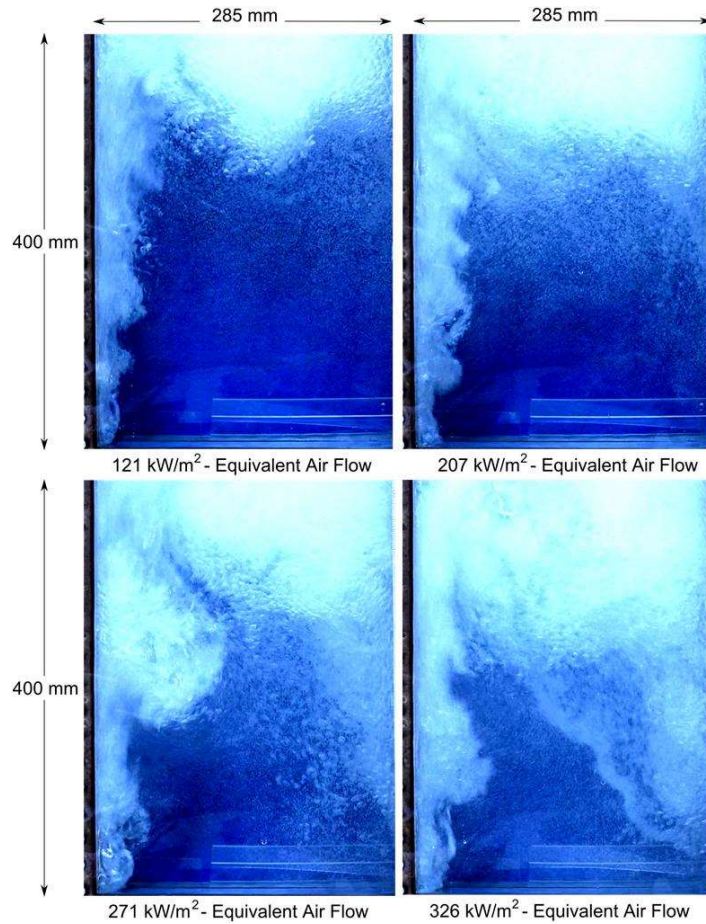


Figure 4. Tests in the Absence of Shielding Balls

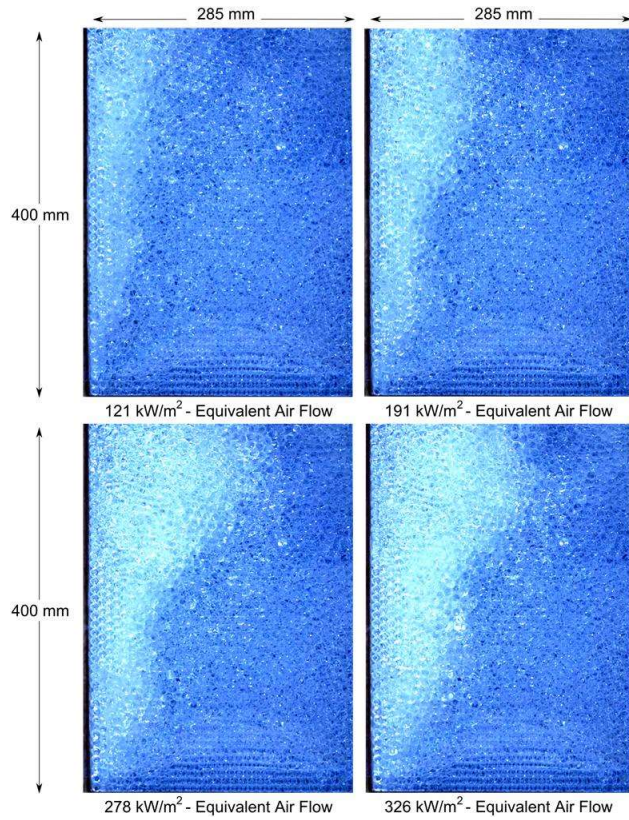


Figure 5. Tests with 9.5 mm Shielding Balls

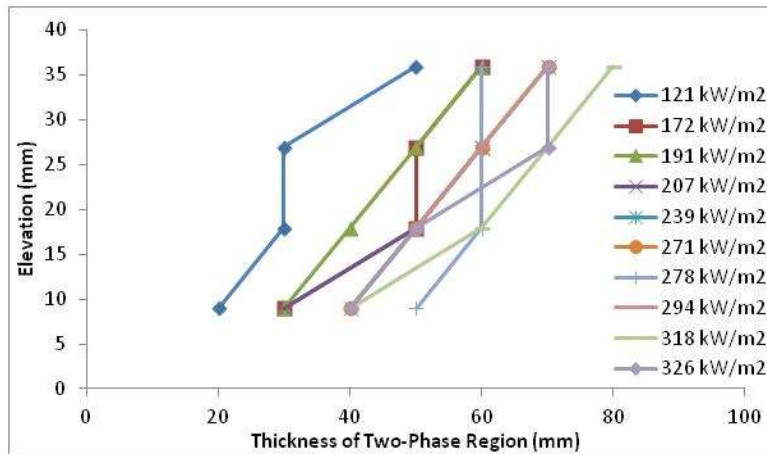


Figure 6. Minimum Thickness of Two-Phase Region vs. Elevation - 9.5 mm Shielding Balls

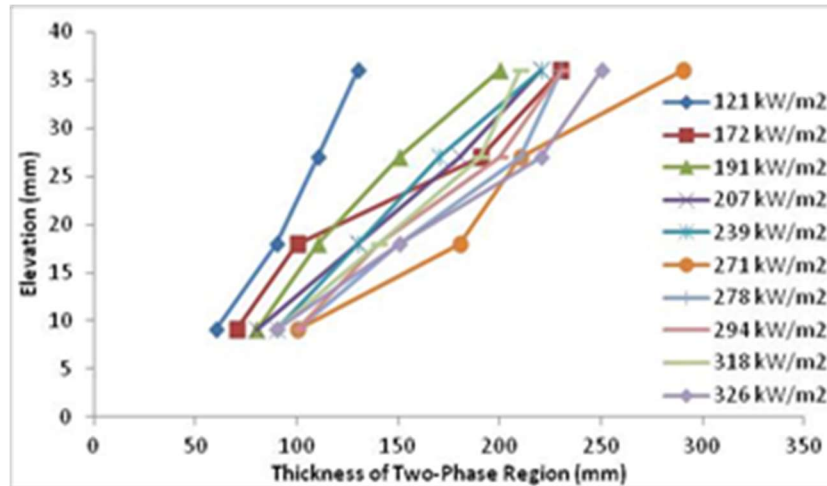


Figure 7. Maximum Thickness of Two-Phase Region vs. Elevation - 9.5 mm Shielding Balls

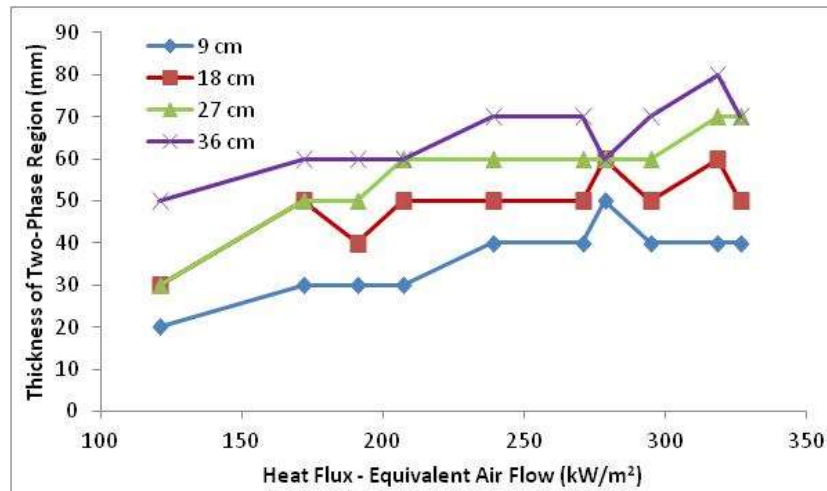


Figure 8. Minimum Thickness of Two-Phase Region vs. Equivalent Heat Flux - 9.5 mm Shielding Balls

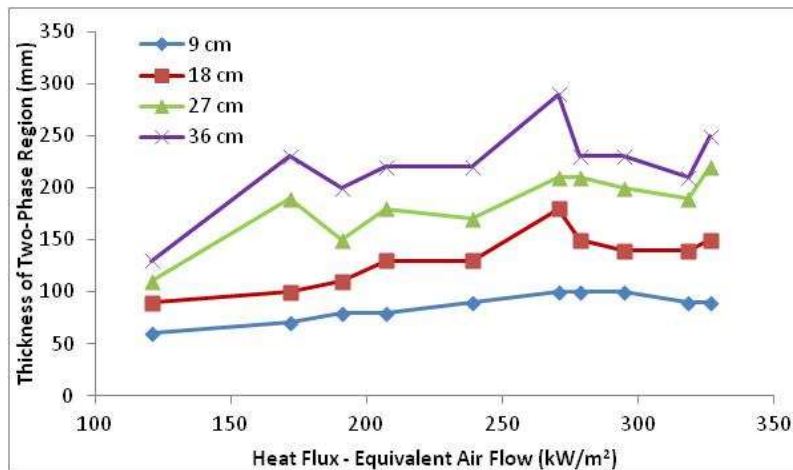


Figure 9. Maximum Thickness of Two-Phase Region vs. Equivalent Heat Flux - 9.5 mm Shielding Balls

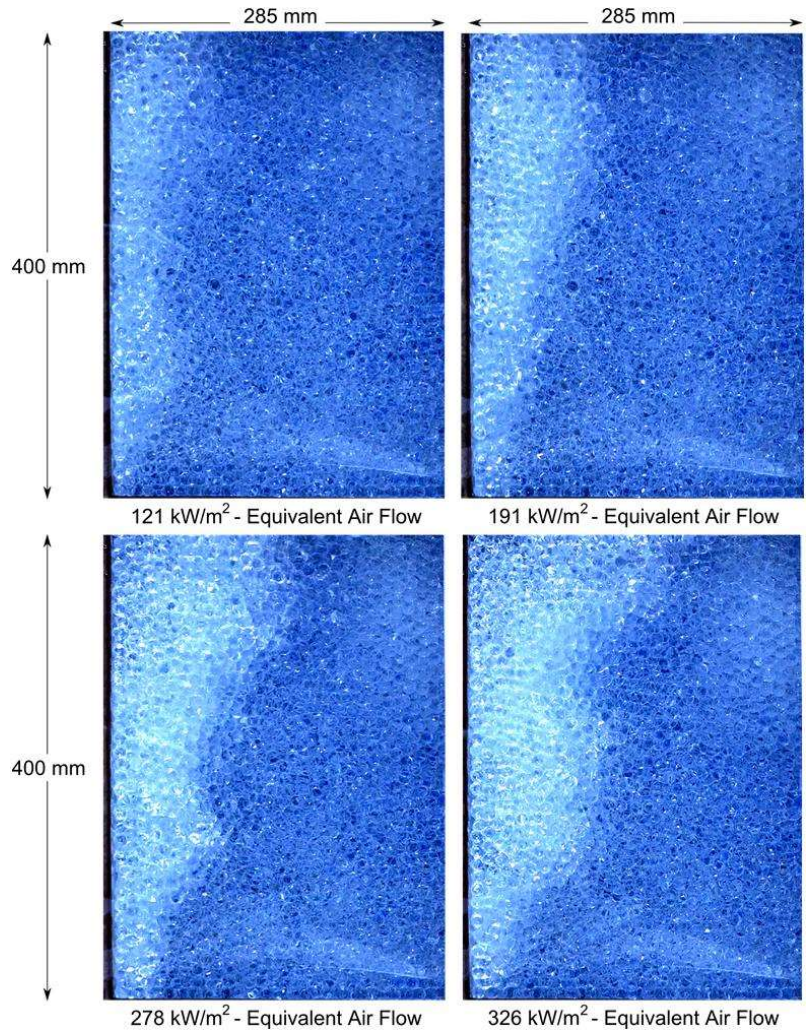


Figure 10. Tests with 11.1 mm Shielding Balls

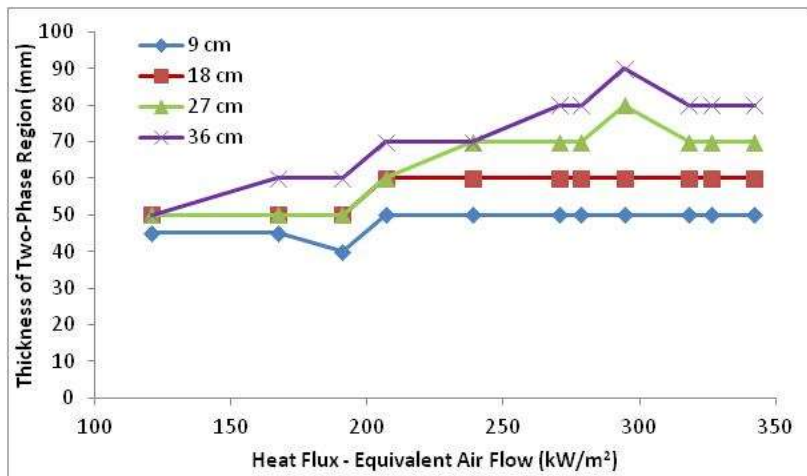


Figure 11. Minimum Thickness of Two-Phase Region vs. Equivalent Heat Flux – 11.1 mm Shielding Balls

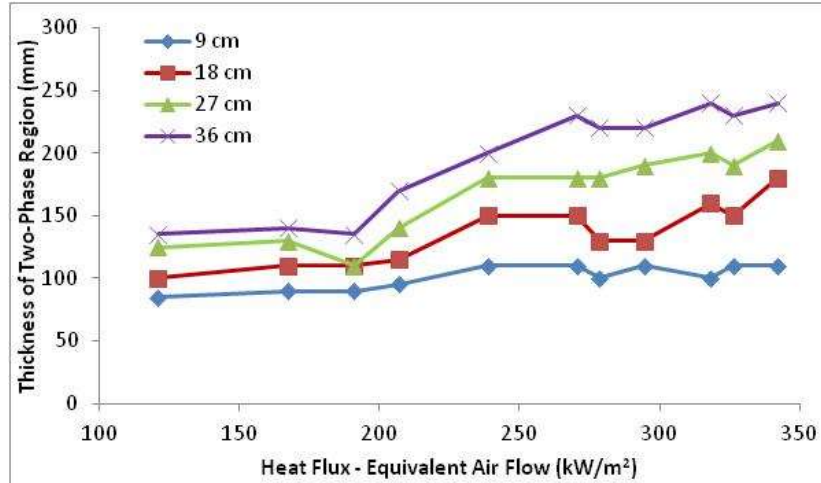


Figure 12. Maximum Thickness of Two-Phase Region vs. Equivalent Heat Flux – 11.1 mm Shielding Balls

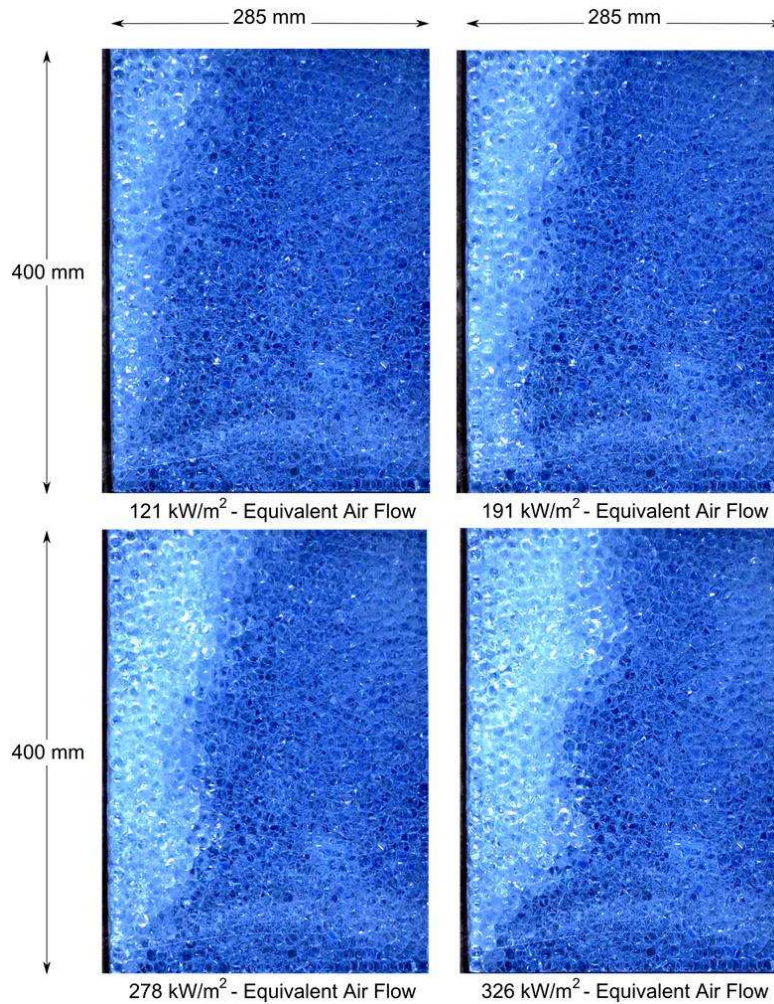


Figure 13. Tests with 12.7 mm Shielding Balls

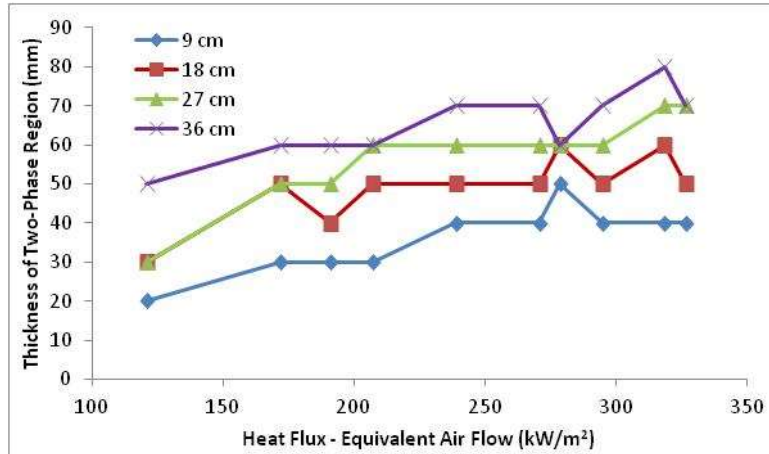


Figure 14. Minimum Thickness of Two-Phase Region vs. Equivalent Heat Flux - 12.7 mm Shielding Balls

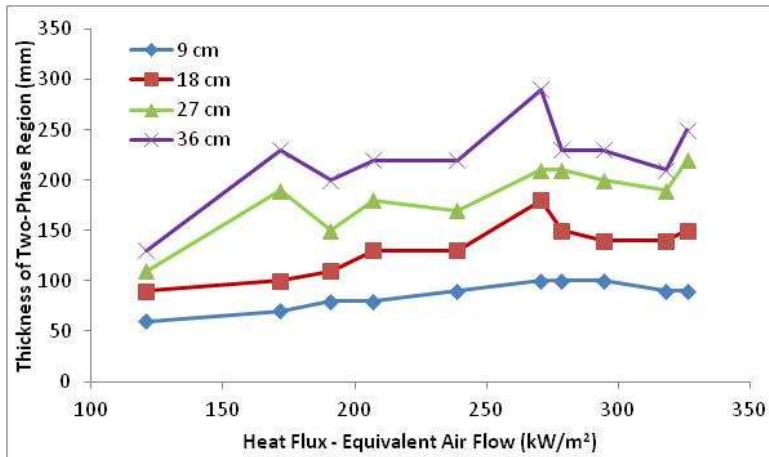


Figure 15. Maximum Thickness of Two-Phase Region vs. Equivalent Heat Flux – 12.7 mm Shielding Balls

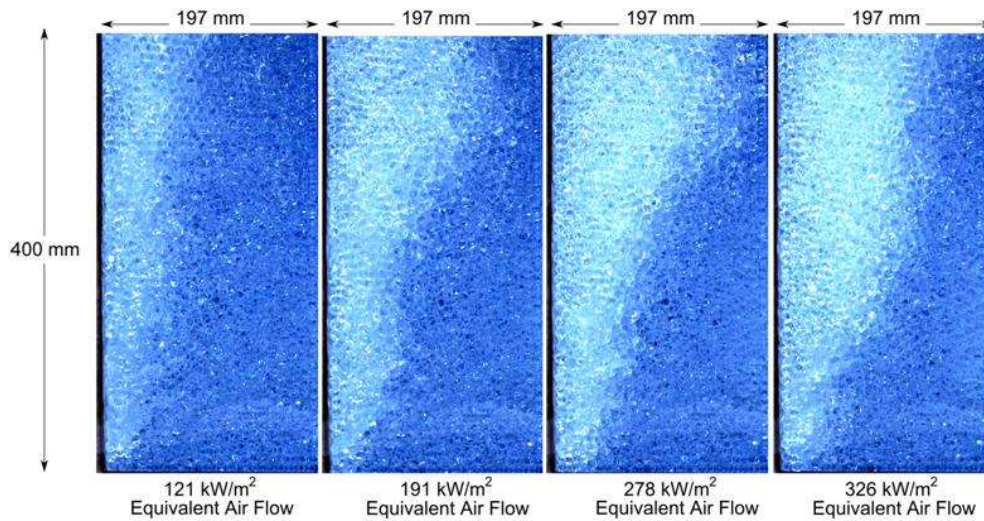


Figure 16. Tests with 9.5 mm Shielding Balls and Cavity Thickness Reduced to 197 mm

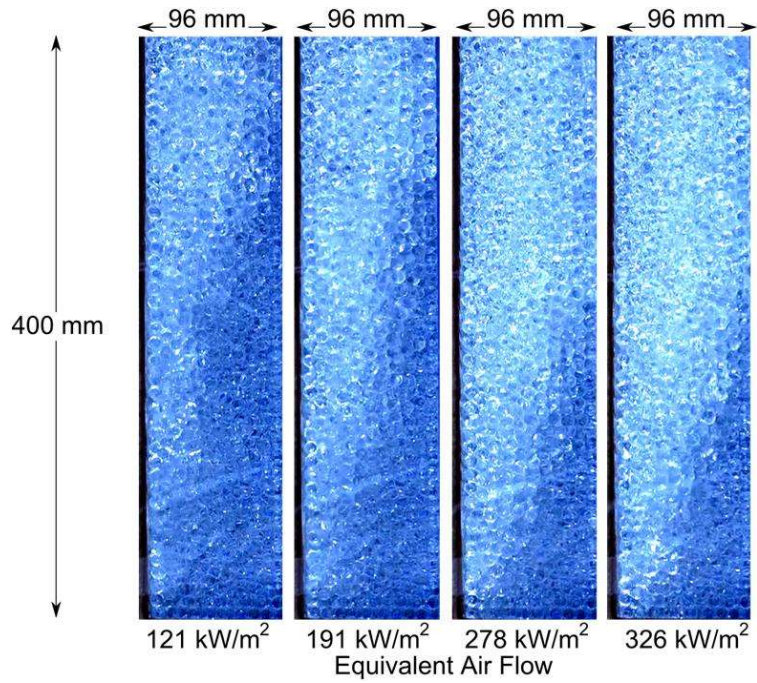


Figure 17. Tests with 9.5 mm Shielding Balls and Cavity Thickness Reduced to 96 mm

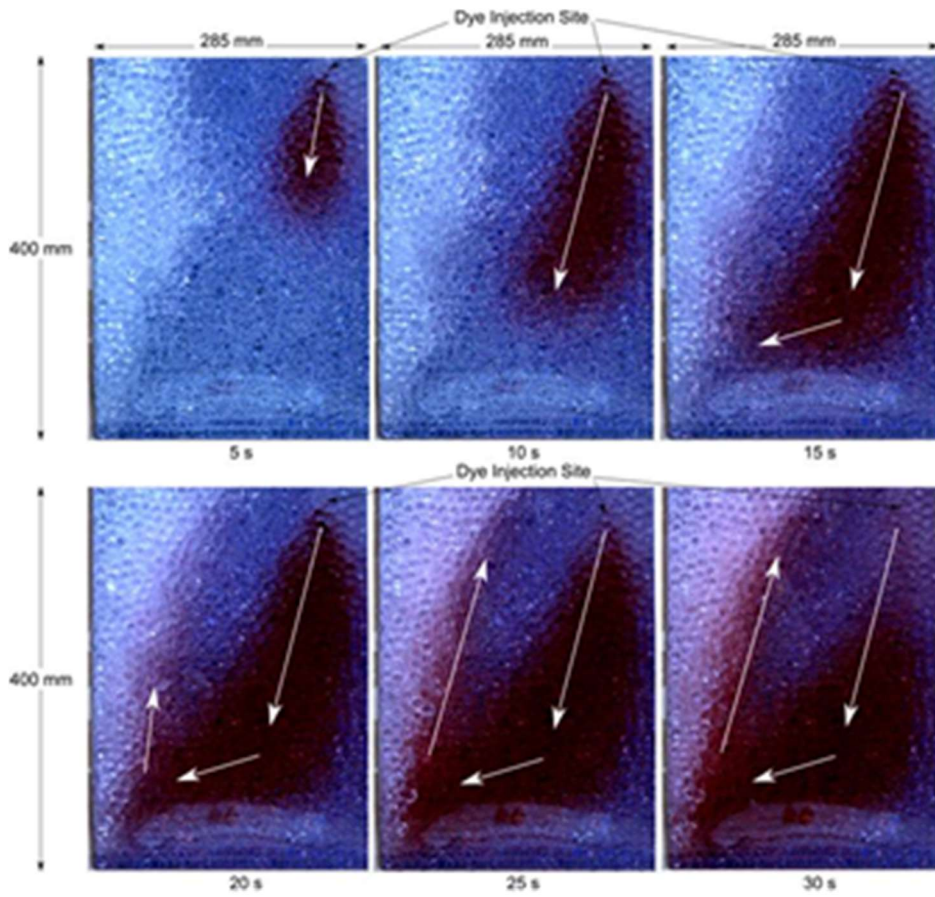


Figure 18. Flow Visualization Test

## 6. Critical Heat Flux in a CANDU End Shield – Influence of Shielding Ball Diameter

### 6.1. Preface

#### 6.1.1. Citation

The paper can be cited as follows:

J. Spencer, Critical heat flux in a CANDU end shield – Influence of shielding ball diameter, Nuclear Engineering and Technology, Volume 54, Issue 4, April 2022, Pages 1343-1354  
<https://doi.org/10.1016/j.net.2021.10.008>

#### 6.1.2. Contribution to Knowledge

The first objective of the paper presented in this section was to quantify the CHF, and its dependence on key variables. Specifically, following on the findings of the papers presented in Section 4 and 5, this objective was pursued by investigating the impact of shielding ball diameter and heating surface conditions on CHF. Additional objectives of the paper were mechanism identification and the progression toward a mechanistic correlation.

These objectives were approached through the performance of experiments using the same apparatus presented in Section 4. The only significant modification to the apparatus was the replacement of the shielding balls abutting the heating surface in the earlier test campaign with a series of sets of shielding balls having different diameters and material compositions. Tests were performed with non-metallic shielding balls were used to address the following questions, drawn from Table 5:

- What are the constituents of a mechanistic model of CHF in this geometry? Specifically, what is the effect of heat conduction through shielding balls on CHF?
  - The borosilicate glass comprising these balls has a much lower thermal conductivity than the carbon steel comprising CANDU-prototypic shielding balls. The finding that CHF is relatively insensitive to shielding ball thermal conductivity suggests that conduction of heat through the shielding balls need not be accounted for in a mechanistic model of CHF.
- Does the condition of the heating surface affect the CHF? If so, how?
  - The hypothesized deposition of iron oxide particles on the heating surface (after being transported from the shielding balls) was tested by first measuring the CHF with borosilicate shielding balls, with the heating surface cleaned of such particles. The heating surface remained free of such particles during testing, as no carbon steel shielding balls were present. Subsequently, CHF was measured with borosilicate shielding balls, with a heating surface fouled by iron oxide particles (deposited during an intervening test using carbon steel shielding balls). The impact of such deposits on CHF was observed, although quantification of the impact was subject to uncertainties deriving from uncontrolled and unmeasured evolution of the surface conditions during the tests. There was no overlap between the uncertainty bands of the ‘clean’ and ‘fouled’ data sets, provided that the ‘fouled’ data set excludes the result of the final test

in the series, carried out when it is hypothesized that turbulent near-wall conditions had removed some fraction of the iron oxide particles from the surface.

Tests were also performed using shielding balls of diameters ranging from 6.4 mm to 12.7 mm. The results of these tests permitted development of an empirical, best estimate correlation of CHF as a function of shielding ball diameter. The data presented in Section 4 was analysed to produce best estimate values (as opposed to the conservative ones presented previously) and, along with the data produced in the present experiments, yielded a correlation of CHF as a function of both elevation and shielding ball diameter. This correlation is additionally presented in non-dimensional form.

The conclusions drawn from the experimental results permitted suggestion of the form of a semi-mechanistic model of CHF in this geometry, accounting for elevation, spatially-varying heat flux distribution, and shielding ball diameter. The steps remaining to complete development of such a model are outlined. The proposed model would relate CHF to the local saturation of the porous medium, with the local saturation being determined by the distance between the location in question and the bottom of the plate, the heat flux distribution at lower elevations, and the shielding ball diameter. Progression to a more fully mechanistic model could be carried out through various means, including the mathematical characterization of the spreading of localized ‘patches’ of degraded heat transfer in the vicinity of the contact points between the calandria tubesheet and shielding balls.

Finally, the findings of these experiments are compared to related literature. Similarities to trends in analytical and experimental studies are identified [55][56].

The results presented in this paper constitute a significant progression toward the overarching objective of the thesis presented in Section 1.3: the generation of a model of critical heat flux on the surface of a calandria tubesheet facing the end shield cavity during IVR in a CANDU reactor, having the following characteristics:

1. Predictive ability across the range of all parameters relevant to the reactor scenario;
2. Empirical validation across a range of experimental data;
3. Identified and explained differences and similarities to knowledge base applicable to similar systems; and
4. To the extent practicable, formulation from well-established physical laws (i.e. a mechanistic model).

In addition, the best estimate correlation presented in this paper constitutes a significant advancement in the ability of safety analysts to predict CHF in the end shield cavity; a phenomenon previously assessed in a PIRT exercise to be both of high importance to severe accident outcomes, and having a high uncertainty [11].

### 6.1.3. Author’s Contribution to Paper

The author conceptualized the experimental techniques, and defined the conditions to be used. Performance of the experiments was led by the author, with assistance by Canadian Nuclear Laboratories (CNL) technologists and the supervisor of the high temperature fuel channel laboratory. Finally, analysis of the experimental data and preparation of the paper was carried out by the author.

## 6.2. Publication

### 6.2.1. Abstract

Experiments were performed to measure the critical heat flux (CHF) on a vertical surface abutting a coarse packed bed of spherical particles. This geometry is representative of a CANDU reactor calandria tubesheet facing the end shield cavity during the in-vessel retention (IVR) phase of a severe accident. Deionized light water was used as the working fluid. Low carbon steel shielding balls with diameters ranging from 6.4 - 12.7 mm were used, allowing for the development of an empirical correlation of CHF as a function of shielding ball diameter. Previously published data is used to develop a more comprehensive empirical correlation accounting for the impacts of both shielding ball diameter and heating surface height. Tests using borosilicate shielding balls demonstrated that the dependence of CHF on shielding ball thermal conductivity is insignificant. The deposition of iron oxide particles transported from shielding balls to the heating surface is verified to increase CHF non-trivially. The results presented in this paper improve the state of the knowledge base permitting quantitative prediction of CHF in the CANDU end shield, refining our ability to assess the feasibility of IVR. The findings clarify the mechanisms governing CHF in this scenario, permitting identification of potential future research directions.

Key Words: Severe Accident, IVR, CANDU, Boiling, Critical Heat Flux, Porous media

### 6.2.2. Introduction

In the event that an unmitigated severe accident were to occur in a CANDU pressurized heavy water reactor, decay heat from the fuel would drive the system through a series of increasingly-severely degraded core states. Eventually, the fuel and other in-core materials would form a terminal debris bed (TDB) at the bottom of the calandria vessel (CV) [1, 2, 3]. Decay heat generated by fission products in the TDB would result in a pool of liquid 'corium' surrounded by a solid crust (Figure 1). If this corium were held in the CV, accident progression would be halted, and high-uncertainty ex-vessel phenomena such as molten core-concrete interaction would be avoided. Assessment of the conditions under which in-vessel retention (IVR) can be sustained is required to predict the progression of CANDU reactors through severe accident states, and the resulting potential release of radioisotopes to the environment.

Successful IVR depends on the fulfilment of several conditions, one of which is the effective removal of heat from the stainless steel walls forming the shell of the CV. These boundaries are submerged in a large volume of light water during normal operation, providing a potential heat sink. If a threshold known as the critical heat flux (CHF) is exceeded, the heat transfer regime could progress from nucleate to film boiling, potentially resulting in loss of the integrity of the CV shell due to a dramatic temperature escalation.

Part of the CV shell is formed by the calandria tubesheet, which is oriented vertically, and abuts a packed bed of steel shielding balls in the reactor end shield cavity. The shielding ball specification provides a range of permissible diameters, with the restriction that the balls used in any given end shield must be uniform. Some study of the effect of shielding ball diameter on boiling behaviour has been carried out using unheated air barbotage experiments [4], but no CHF experiments measuring the effect of this parameter have been reported in literature. Previous heated experiments reported the dependence of CHF on heating surface height where exiting heat flux is uniform (determined indirectly

using a plate of fixed height by reducing the exiting heat flux at higher elevations), and also identified a dependence of CHF on surface conditions [5].

This paper presents the results of CHF experiments investigating the impact of shielding ball diameter, yielding an empirical correlation. A similar dependence on diameter is noted in a previously-published, analytically-derived correlation of CHF in a geometry where the porous medium is capillary in nature [6, 7]. The empirical correlation derived in the present paper is extended to account for heating surface height (with data drawn from previous work [5]). Trends in CHF are identified as a function of shielding ball thermal conductivity and boiling surface conditions. Finally, potential links to studies of related geometries are considered.

### 6.2.3. Literature

The knowledge base allowing for prediction of CHF in geometries resembling a CANDU end shield is relatively undeveloped, with few studies having been performed. Analytical work has included the development of a correlation for CHF on a vertical plate adjacent to a liquid-filled, close-packed porous medium [6, 7]. The derivation presented in these papers considered a scenario of Darcian flow and strong capillary forces. The problem is further simplified by calculating a single set of mixture transport properties that are a function of the local liquid saturation of the porous medium, rather than considering the liquid and vapour phases separately.

In the end shield while boiling is taking place, the particle Reynolds number ( $Re_p$ ) can be roughly approximated at  $10^4$ , a value far greater than the upper threshold for Darcian flow ( $Re_p \approx 10$ ). Furthermore, in contrast with the assumptions applied in References [6, 7], the large diameter of the shielding balls would result in inertial forces being larger than capillary forces (aside from locations very close to contact points). The relative importance of the buoyant and capillary forces can be quantified using the Bond (or Eötvös) number ( $Bo$ ). Considering the end shield scenario,  $Bo < 1$  (indicating capillary forces dominance) for particle (shielding ball) diameters below 2.5 mm. For the shielding ball diameters used in the experiments presented in this paper,  $Bo > 10$ . In spite of these limitations, Equation 1 (Reference [7]) is the most applicable correlation identified by the author in the literature.

$$q''_{CHF} = 2.716 \cdot 10^{-3} \frac{h_{lg} \sigma}{\nu_l} \left( \frac{\varepsilon K}{L^2} \right)^{\frac{1}{4}} \left( \frac{(\rho_l - \rho_g) g K}{\sigma} \right)^{\frac{1}{2}} \quad (1)$$

Here  $q''_{CHF}$  is critical heat flux,  $h_{lg}$  is latent heat of vaporisation,  $\rho_l$  is density of liquid,  $\rho_g$  is density of vapour,  $\sigma$  is surface tension,  $\nu_l$  is kinematic viscosity of liquid,  $\varepsilon$  is porosity of the medium,  $L$  is the height of the heating surface (exiting heat flux  $q''$  is uniform across all elevations between 0 and  $L$ ), and  $g$  is gravitational acceleration. The absolute permeability of the porous medium ( $K$ ) can be expressed using a range of correlations, including the Carman-Kozeny Equation (2).

$$K = \frac{\varepsilon^3}{189(1 - \varepsilon)^2} d^2 \quad (2)$$

It can be inferred from Equations 1 and 2 that for capillary porous media externally heated by a vertical wall, CHF varies with  $d^{3/2}$ , where  $d$  is the particle (or shielding ball) diameter.

Experimental investigations sharing some features with the problem of interest include a study of boiling behaviour on spheres embedded in porous media [8]. In this paper, it was determined that for porous media composed of spherical particles below 10 mm, CHF is largely determined by the flooding limit in the region above the sphere. As the particle size increases above 10 mm, CHF asymptotically approaches the value expected for a bare surface without a surrounding porous medium. Another relevant finding in this paper was that CHF is higher when the surface is oxidized rather than polished, across all particle sizes.

A series of experiments performed at Canadian Nuclear Laboratories (CNL) in 2014 measured CHF using an apparatus designed to represent a CANDU calandria tubesheet facing an end shield cavity filled with shielding balls and water [5]. A stepwise increase in heat flux was used to establish upper and lower bounds on CHF. The key finding of this study was an empirical correlation providing a conservative relationship between CHF and heated surface height (or elevation, with approximately uniform exiting heat flux below the elevation in question), where the shielding balls are 11.1 mm in diameter, and made of low carbon steel.

$$q''_{CHF}[kW/m^2] = -519[kW/m^3] \cdot L[m] + 539.6[kW/m^2], 0.058 \text{ m} < L < 0.398 \text{ m} \quad (3)$$

In addition, a trend was identified, whereby the measured value of CHF increased as the test campaign progressed. This was hypothesized to be a result of the deposition of iron oxide particles on the boiling surface, resulting in improved surface wetting.

A second series of experiments was performed at CNL to study the multiphase flow behaviour of liquid and gas in the end shield cavity, using an air barbotage approach [4]. Tests were performed with acrylic shielding balls having diameters of 9.5 mm, 11.1 mm, and 12.7 mm. The air injection rate was varied to simulate a superficial vapour velocity normal to the heating surface, corresponding to heat fluxes (hereinafter referred to as equivalent 'heat flux') between 121 kW/m<sup>2</sup> and 326 kW/m<sup>2</sup>. Key observations included:

- Helmholtz waves formed without shielding balls, with shielding balls of all diameters, and at all equivalent heat fluxes studied.
- Within the range of air injection studied, the thickness of the air-water region was not significantly impacted by the shielding ball diameter; however, it increased with equivalent heat flux.
- The thickness of the air-water region grew approximately linearly with elevation.
- Lateral entrainment of liquid into the air-water region was apparent.

#### 6.2.4. Experimental Apparatus and Procedure

The apparatus used for the experiments reported in Reference [5] was repurposed for the tests presented in this paper. The primary modification was that different shielding ball diameters and compositions were used. The heating plate is 0.6 m in height (the anticipated contact height between

the corium and the calandria tubesheet), 0.3 m in width, and is made of copper (Figure 2). Cartridge heaters and Type-K thermocouples were embedded in the plate, such that the boiling surface was undisturbed (Figure 3). The heating plate abutted a packed bed of shielding balls (slightly deeper than the top of the plate to minimize edge effects), filled with water at saturation temperature. The roughness of the boiling surface was less than 1.6  $\mu\text{m}$  RMS (63 micro-inch).

A make-up water system compensated water depleted through boiling, maintaining the level in the main tank within approximately 50 mm. Steam produced within the main tank was condensed and weighed in real time, providing a tertiary means of calculating heat flux. The primary and secondary means of calculating this value were through measurements of the electrical power supplied to the cartridge heaters, and measurements of the temperature gradient in the heating plate. A photograph of the test apparatus is shown in Figure 4.

The main tank was largely sealed from the atmosphere, and the water it contained was continuously sparged with argon in an effort to limit the rate of oxidation of the shielding balls. Low carbon steel shielding balls with three diameters were utilized to span the range allowable in CANDU 6 reactors (9.5 mm to 12.7 mm), and a smaller diameter (6.4 mm) was used to extend toward the better-studied range in which capillary forces become somewhat important. A fifth set of shielding balls was used, with thermal shock-resistant borosilicate balls 11.0 mm in diameter occupying the space within approximately 100 mm of the heating plate, and less expensive soda lime glass balls with the same diameter filling the remainder of the volume simulating the end shield cavity (see Figure 5).

Tests were carried out by increasing the heat supplied to the plate in a stepwise fashion, with a steady state attained at each level prior to the subsequent increase. Temperature transients (rapid increases) were observed through thermocouple measurements when CHF was exceeded. Following initiation of the temperature transient, heating was ceased, allowing nucleate boiling to be re-established. The lengthy campaign included tests with both uniform and spatially-varying heat flux; however, the purposes of the paper are fulfilled by the uniform heating cases. Extensive additional analysis is required before the results of the spatially-varying tests can be reported in a satisfactory manner.

Tests were carried out in ten series (Table 1), each of which was performed on a separate day. Prior to test series where the initial surface conditions were 'clean', the heating plate surface was lightly scrubbed with an alumina pad and thoroughly rinsed with acetone, followed by deionized water.

Table 1. Overview of Shielding Ball Variation Tests

Series Name	Ball Material	Ball Diameter	Surface Initial Conditions
ES-BP-1	Borosilicate	0.011 m	Clean
ES-BP-2	Steel	0.0111 m	Clean
ES-BP-3	Borosilicate	0.011 m	Oxides deposited
ES-BP-4	Steel	0.0127 m	Clean
ES-BP-5	Steel	0.0127 m	Oxides deposited
ES-BP-6	Steel	0.0127 m	Clean
ES-BP-7	Steel	0.095 m	Clean
ES-BP-8	Steel	0.0064 m	Clean
ES-BP-9	Steel	0.0127 m	Clean
ES-BP-10	N/A	N/A	Clean

A leak in the main water tank developed during test series ES-BP-4 and ES-BP-5. Results for these test series are not included in the analysis due to the potential influence of the leak and the high rate of make-up water addition.

### 6.2.5. Results

In the interest of simplicity, the primary method of calculating heat flux reported in this paper is via the electrical power supplied to the cartridge heaters. This approach provides a spatially-averaged value, ignoring edge effects. As expected, the heat flux exiting the plate is somewhat below the spatial average very close to the top and bottom of the plate, and higher near the middle (Figure 6).

The electrical measurements are further validated by comparison with the condensate measurements (Figure 7). The time average power calculated from these measurements is approximately 8 kW below the electrical power measurement (approximately 10% of the cases with the highest heat flux). This differential can be explained as a combination of thermal losses from the large outer surfaces of the main water tank, minor vapour leakage, and the addition of make-up water that is somewhat below the saturation temperature.

#### 6.2.5.1. Dependence of CHF on Shielding Ball Diameter

In each successful series, several tests were repeated with heat delivered in the most spatially uniform manner possible. The CHF for each test was taken to be the average of the highest heat flux at which nucleate boiling was sustained in a steady state, and the heat flux at which a temperature transient was observed. For such uniform heating cases, the trend of CHF falling with elevation observed in Reference [5] resulted in this temperature transient occurring near the top of the heating plate. The results of the tests performed with steel shielding balls are summarized in Table 2.

Table 2. Summary of Results of Tests with Steel Shielding Balls and Uniform Heating

Shielding Ball Diameter (m)	$q''_{CHF}$ (kW/m <sup>2</sup> )	Standard Deviation (kW/m <sup>2</sup> )	Sample Size	95% Confidence Interval (kW/m <sup>2</sup> )
0.0064	161.3	0.65	3	0.73
0.0095	294.8	2.97	3	3.36
0.0111	357.3	6.65	4	6.51
0.0127	462.4	5.02	6	4.01

A trend in the data presented in Table 2 is apparent, with CHF increasing with ball diameter. An empirical correlation in a power law form fitted to the data via a least squares method is defined in Equation 4.

$$q''_{CHF} \left[ \frac{W}{m^2} \right] = C_1 \cdot d^{1.49} [m], \quad 0.00635m \leq d \leq 0.0127m \quad (4)$$

$$C_1 = 3.03 \cdot 10^8, \quad R^2 = 0.997$$

Here,  $C_1$  is an empirical constant. The close similarity of the ball diameter dependence shown in Equation 4 to that implied by the analytically-derived Equation 1 justifies the formulation of Equation 5.

$$q''_{CHF} \left[ \frac{W}{m^2} \right] = C_2 \cdot d^{3/2} [m], \quad 0.00635m \leq d \leq 0.0127m \quad (5)$$

$$C_2 = 3.16 \cdot 10^8, \quad R^2 = 0.994$$

Here,  $C_2$  is an empirical constant. Equations 4 and 5 are specifically applicable to the experimental apparatus used in the experiments reported in this paper. The leading constant could be expected to change as a function of parameters including the heating surface conditions and the height of the heating plate. The data presented in Table 2 is compared to Equations 4 and 5 in Figure 8 (where the error bars represent the 95% confidence interval).

#### 6.2.5.2. Dependence of CHF on Heating Surface Height

The correspondence of test conditions between series ES-BP-2 and the experiments detailed in Reference [5] presents the opportunity to expand Equation 5 to account for the dependence of CHF on heating surface height where exiting heat flux is uniform (determined indirectly using a plate of fixed height by reducing the exiting heat flux at higher elevations).

Comparison of the experimental data taken from Reference [5] to that presented in this paper requires some adjustment to account for the evolution of surface conditions during and between the two test campaigns. It is also necessary to adjust for the fact that the data was treated in a conservative fashion in Reference [5] (assuming the minimum of the spatial and heat flux uncertainty ranges), whereas the intent in this paper is to derive a best estimate correlation.

Empirical adjustment for evolving surface conditions was made possible through comparison of tests with otherwise identical conditions performed in each campaign (steel shielding balls with a diameter of 11.1 mm, with heat delivered in a uniform manner). An increase in CHF of approximately 20% was measured between the first campaign [5] and the one reported here, which is inferred to be the result of an evolution of surface conditions. Comparison between the two campaigns is made possible by multiplying the previously-published values of CHF by a constant, such that the result is consistent with those produced in tests performed under equivalent conditions in the more recent test series.

The locations of dryout occurrence were taken in Reference [5] to be the minima of the spatial uncertainty bands. In this paper, the midpoints are used for both the experiments presented herein, and the data drawn from Reference [5]. Given the spatially-varying nature of the heat flux exiting the plate, the heat flux at this elevation was assessed using the finite element simulation results presented in Reference [5] (see Figure 9). In this paper, the CHF for tests from both campaigns are taken to be the average of the upper and lower bounds, established by the highest heat flux at which nucleate boiling was maintained, and the heat flux at which a temperature transient was observed.

After scaling of the results presented in Reference [5] as outlined above, an empirical fit results in Equation 6, shown in Figure 10. The range of heating surface heights over which the equation is considered applicable is defined by the highest and lowest elevations at which a temperature transient was detected in the tests considered.

$$q''_{CHF} \left[ \frac{W}{m^2} \right] = C_3 \cdot d^{3/2} [m] \cdot L^{-0.314} [m], \quad 0.00635m \leq d \leq 0.0127m, \quad (6)$$

$$0.144m \leq L \leq 0.516m, \quad C_3 = 2.63 \cdot 10^8, \quad R^2 = 0.977$$

Here,  $C_3$  is an empirical constant.

### 6.2.5.3. Dependence of CHF on Surface Fouling

In cases where low carbon steel shielding balls were used, oxidation on the ball surfaces led to suspension of iron oxide particles in the water, visible through the walls of the main tank. The deposition of some of these particles on the heating surface was apparent during qualitative post-test examination. The effect of this surface fouling was hypothesized to be an increase in CHF in Reference [5], through its impact on contact angle (increasing surface wetting relative to a clean surface). This hypothesis was tested through the use of borosilicate shielding balls.

In test series ES-BP-1, an initially-clean surface was used, and CHF was determined to be stable with time following initiation of heating in the test series, as shown in Figure 11 (where the error bars represent the highest heat fluxes at which nucleate boiling was sustained, and at which a temperature transient was observed). This result was consistent with the hypothesis in that no iron oxide particles were deposited on the surface during test operation. Prior to test ES-BP-3, a test series was run using steel balls, and care was taken to leave the deposits undisturbed on the heating surface while transitioning from one series to the next. This test series demonstrated a reduction in CHF with time, presumably as iron oxide particles were progressively removed from the heating surface via resuspension under turbulent near-wall conditions during boiling. Comparison of these two trends, along with the trend of an increase in CHF with time when steel shielding balls are present, supports the hypothesis that iron oxide particle deposition on the boiling surface increases CHF.

### 6.2.5.4. Dependence of CHF on Shielding Ball Thermal Conductivity

The direct contact between the shielding balls and the heating surface raises the possibility that the balls could act as heat-conducting fins, potentially increasing CHF. If heat transport via such fins during high heat flux nucleate boiling were an important factor, it could be expected that CHF would increase with the thermal conductivity of the material comprising the shielding balls.

In contrast with the relatively high thermal conductivity of the steel shielding balls (on the order of 50 W/m-K), that of the borosilicate shielding balls used in test campaigns ES-BP-1 and ES-BP-3 is low (on the order of 1 W/m-K). Test results using borosilicate shielding balls with an initially-fouled surface (ES-BP-3) and steel balls are compared in Figure 12. The error bars for each test represent the highest heat flux at which nucleate boiling was sustained, and the heat flux at which a temperature transient was observed. Equations 4 and 5 predict that the small difference in shielding ball diameter (resulting from limitations on material availability) would result in CHF for the steel shielding balls being 5 kW/m<sup>2</sup> (approximately 1.4%) higher than the borosilicate case. The x-axis in this figure represents the time delay between the start of each test series (comprising multiple tests) until the test in question; that is, the length of time over which rapid evolution of the surface would be expected. This surface aging process is not directly measured, but is hypothesized to be driven by the deposition and removal of iron oxide particles on the heating surface, following their production on the shielding balls. In spite of the

large difference in thermal conductivity of shielding ball material, the results of the initial tests in each series are within the measurement uncertainty. Subsequent measurements diverge, as would be expected from the understanding of the impact of iron oxide particulate deposition on the heating surface.

The absence of significant sensitivity of CHF to shielding ball thermal conductivity, and the implied relative unimportance of conduction through the shielding balls can be explained through several factors, including: the large ratio of the heating surface area in contact with liquid water versus the shielding balls, the thermal resistance at the interface between the shielding balls and the wall in comparison with the nucleate boiling heat transfer coefficient, and the modest difference in temperature between the wall and the shielding balls (less than 30 °C prior to dryout).

### 6.2.6. Discussion

When solved for particle diameters corresponding to the shielding balls used in the experiments reported in this paper, Equation 1 predicts values of CHF as high as about 3 MW/m<sup>2</sup> for a 0.6 m tall heating plate – a value well above that established for vertical walls in unobstructed pool boiling conditions. The CHF criterion applied in this correlation is the threshold at which liquid saturation in the porous medium adjacent to the heating surface reaches zero. This is equivalently expressed as the point at which the fraction of the pore volume occupied by liquid (liquid saturation –  $s$ ) is zero. Assuming the applicability of the dependence of  $s$  on elevation, ball diameter, and heat flux derived in References [6] and [7] to externally-heated coarse porous media, these observations suggest that  $s > 0$  when dryout of the surface occurs, and that the determining mechanism of CHF is to be found at the heating surface, rather than in the far field of the porous medium. This result is supported by the finding of the present study that CHF is dependent on surface fouling. It also parallels the observation in Reference [8] that, below a threshold particle diameter and value of CHF, the key mechanism was a flooding limit. Above this threshold particle diameter, the dominant mechanism migrated to the heating surface itself, with the value of CHF asymptotically approaching that of an unobstructed surface as particle diameter increased.

The dependence of CHF on shielding ball diameter expressed in Equation 4 ( $d^{1.4908}$ ) and Equations 1 and 2 ( $d^{3/2}$ ) is nearly identical. This is in spite of the fact that the derivation of Equation 1 relies on two assumptions believed to be inapplicable to the case: that capillary forces are important in the porous medium in question, and that a Darcian flow regime is present. It is also notable that this similarity persists in spite of the use of the assumption that dryout occurs at the point where liquid saturation of the porous medium reaches zero, in the derivation of Equation 1.

Recognizing that the shielding ball dependence expressed in Equations 1 and 5 is identical, Equation 5 can be re-expressed in the form of Equation 1, using the thermophysical quantities relevant to the experiments presented in this paper and Reference [5]. However, the  $L^{1/2}$  dependence of CHF implied by these equations does not match the relevant data. This shortcoming can be addressed through the addition of a dimensionless heating surface height term, such that the resulting dependence on  $L$  is consistent with Equation 6.

$$q''_{CHF} \left[ \frac{W}{m^2} \right] = C_4 \frac{h_{lg} \sigma}{\nu_l} \left( \frac{\varepsilon K}{L^2} \right)^{\frac{1}{4}} \left( \frac{(\rho_l - \rho_g) g K}{\sigma} \right)^{\frac{1}{2}} \left( \frac{(\rho_l - \rho_g) g L^2}{\sigma} \right)^{0.093}, \quad (7)$$

$$0.00635m \leq d \leq 0.0127m, 0.144m \leq L \leq 0.516m, C_4 = 1.40 \cdot 10^{-4}, \\ R^2 = 0.977$$

Here,  $C_4$  is an empirical constant that could be expected to vary with surface conditions. Equation 7 is equivalent to the empirically-derived Equation 6, given applicable values of the thermophysical properties, and the use of the Carman-Kozeny equation for permeability. Further investigation would be required to determine the applicability of this correlation to conditions deviating significantly from those reflected in the experiments presented in this paper and Reference [5].

Equation 7 can be re-expressed in terms of the permeability Bond number ( $Bo_k$  – Equation 8) and the length-scale Bond number ( $Bo_L$  – Equation 9), as shown in Equation 10. The length-scale Bond number follows an approach commonly used in pool boiling CHF studies to non-dimensionalize the characteristic heater length, with the same grouping of parameters as the Taylor wavelength.

$$Bo_k = \frac{(\rho_l - \rho_g) g K}{\sigma} \quad (8)$$

$$Bo_L = \frac{(\rho_l - \rho_g) g L^2}{\sigma} \quad (9)$$

$$q''_{CHF} \left[ \frac{W}{m^2} \right] = C_4 \frac{h_{lg} \sigma}{\nu_l} \varepsilon^{\frac{1}{4}} Bo_k^{\frac{3}{4}} Bo_L^{-0.157}, \quad (10)$$

Conversion of Equation 10 into dimensionless form using the Kutateladze number ( $Ku$  – Equation 11) and the Ohnesorge number ( $Oh$  – Equation 12, defined using the same grouping as the Taylor wavelength) simplifies comparison to a broad range of published results of CHF in pool boiling situations.

$$Ku = \frac{q''_{CHF} / \rho_g h_{lg}}{\left[ \sigma g (\rho_l - \rho_g) / \rho_g^2 \right]^{\frac{1}{4}}} \quad (11)$$

$$Oh_L = \nu_l \left[ g (\rho_l - \rho_g) \rho_l^2 / \sigma^3 \right]^{\frac{1}{4}} \quad (12)$$

$$Ku = \frac{C_4 \varepsilon^{\frac{1}{4}} Bo_k^{\frac{3}{4}} Bo_L^{-0.157}}{Oh_L \left[ \rho_g / \rho_l \right]^{\frac{1}{2}}} \quad (13)$$

The limits of applicability for Equation 13 are summarized in Table 3. In calculating  $Bo_k$ , the Carman-Kozeny Equation (2) is used. Equations 7 and 13 have been defined such that they result in identical predictions to Equations 5 and 6, for an equivalent set of conditions. Comparisons of Equations 7 and 13 to the relevant experimental data is thus provided by Figures 8 and 10.

Table 3. Limits of Applicability of Summary of Results of Tests with Steel Shielding Balls and Uniform Heating

Shielding Ball Diameter (m)	Heating Surface Height (m)	$Bo_k$	$Bo_L$	$Ku$
0.00635 (min)	0.516 (max)	0.00636 (min)	42500 (max)	0.0248
0.0127 (max)	0.144 (min)	0.0127 (max)	3310 (min)	0.0623

For comparison, in his foundational work on CHF, Kutateladze found a range of  $0.13 \leq Ku \leq 0.19$ , with a recommended value of 0.16 [9], for upward-facing surfaces. Comparable values are found for unobstructed vertical surfaces; for example, Monde et al. [10] found a range  $0.132 \leq Ku \leq 0.148$  using a copper heater in water. It is apparent that the shielding balls reduce  $Ku$  and CHF, relative to the unobstructed case.

It is hypothesized that CHF at any location of a given liquid and surface system is a function of two key variables: liquid saturation of the porous medium and shielding ball diameter. It is expected that the saturation is a function of upstream (i.e. lower elevation) heat flux, elevation, and shielding ball diameter. While determination of the functions  $q''_{CHF}(s,d)$ , and  $s(q'',L,d)$  is outside of the scope of this paper, it is expected that they could be established through future work. This would yield a semi-mechanistic correlation of CHF in a CANDU end shield as a function of elevation, spatially-varying heat flux distribution, and shielding ball diameter. It is anticipated that it would be possible to determine  $s(q'',L,d)$  through experiments similar to those presented in Reference [5]. Once this function is formulated, it would be possible to determine  $q''_{CHF}(s,d)$  by calculating the upstream heat flux. This would permit the inference of the liquid saturation at the location of dryout for the experimental results presented in this paper and Reference [5], and comparison of  $s$  to the heat flux experienced at these locations when dryout occurred.

In consideration of the broader topic of CHF in externally-heated porous media, the results of this paper suggest that further work investigating the transition from capillary (Equation 1) to coarse porous media (Equations 5 and 6) may be useful. Potential approaches could include experiments using particles with smaller diameters, modification of existing CHF models for unobstructed vertical surfaces to account for the influence of a porous medium, and analytical efforts to remove the assumptions inapplicable to coarse media applied in the derivation of Equation 1. These suggested extensions are not required for

the objective of this paper and, hence, not pursued as part of this work, because the shielding balls are of a fixed range of diameters.

The qualitative observation that shielding ball thermal conductivity does not have a significant impact on CHF is consistent with physical reasoning, and does not call for further investigation. In contrast, the verification of the trend that iron oxide deposition increases CHF suggests that further investigation of the impact of surface conditions on CHF in this geometry is of potential importance. Subjects of interest would include the impact of roughness, contact angle (and its dependence on the presence of oxides), and the state of the calandria tubesheet in operating CANDU reactors. Development of the impact of these parameters would justify modification of the leading constant in Equation 6 ( $C_3$ ), and would allow for prediction of CHF under a range of surface conditions.

### 6.2.7. Summary

This paper presents the results of a series of tests measuring CHF in a geometry representative of a CANDU calandria tubesheet abutting a shielding ball-filled end shield cavity. CHF is correlated to shielding ball diameter. The relationship between the two variables is effectively identical to a previously-published correlation derived for a capillary porous medium externally heated by a vertical wall. The previously-published correlation is modified such that it agrees with the results of both the experiments presented in this paper, and previously-published experiments investigating the impact of heating surface height.

The experimental data verifies that the impact of shielding ball thermal conductivity on CHF is minimal. This supports the contention that heat transfer from the boiling surface via a ‘fin effect’ is insignificant. The impact of the deposition of iron oxide particulate on the heating surface is verified to be significant, with CHF increasing as the deposition process progresses.

Finally, suggestions are made for future investigations with the potential to verify the hypotheses presented in this paper, and improve the ability to quantify the dependence of CHF on key variables. Such future efforts could clarify the relation of this system’s behaviour to the more established knowledge base pertaining to capillary porous media.

### 6.2.8. Nomenclature

#### Acronyms

BC	Boiling Crisis
CANDU	CANada Deuterium Uranium
CHF	Critical Heat Flux
CNL	Canadian Nuclear Laboratories
FP	Fission Product
IVR	In-Vessel Retention
RMS	Root Mean Squared
TDB	Terminal Debris Bed

Variables

$C$	Empirically-derived constant, units vary by instance – $[W/m^3]$ or $[W/m^4]$
$d$	Diameter (of shielding balls) [m]
$Bo$	Bond number
$g$	Gravitational acceleration $[m/s^2]$
$h$	Latent heat of phase change $[J/kg]$
$q''$	Heat flux $[W/m^2]$
$K$	Absolute permeability $[m^2]$
$Ku$	Kutateladze number
$L$	Length of heated plate [m]
$Oh$	Ohnesorge number
$Re$	Reynolds number
$s$	Liquid saturation of the porous medium
$\epsilon$	Porosity
$\nu$	Kinematic viscosity $[m^2/s]$
$\rho$	Density $[kg/m^3]$

Subscripts

$1,2,3,4$	Differentiators of empirically-derived constants
$CHF$	Critical Heat Flux
$g$	Gas
$k$	Permeability
$l$	Liquid
$L$	Length
$p$	Particle

### 6.2.9. References

1. J.C. Luxat, Thermal-hydraulic aspects of progression to severe accidents in CANDU reactors, *Nucl. Technol.* 167(1) (2009) 187-210.
2. T. Nitheanandan, M.J. Brown, Backup and ultimate heat sinks in CANDU reactors for prolonged SBO accidents, *Nucl. Eng. Technol.* 45(5) (2013) 589-596.
3. F. Zhou, D.R. Novog, Mechanistic modelling of station blackout accidents for a generic 900 MW CANDU plant using the modified RELAP/SCDAPSIM/MOD3.6 code, *Nucl. Eng. Des.* 335 (2018) 21-93.
4. J. Spencer, Results of air barbotage experiments simulating two-phase flow in a CANDU end Shield during in-vessel retention, *ASME J. Nucl. Rad. Sci.* 3(2) (2017) 1-10.
5. J. Spencer, Measurement of critical heat flux in a CANDU end shield consisting of a vertical surface abutting a packed bed of steel shielding balls, *CNL Nucl. Rev.* 6(1) (2017) 79-90.
6. C.Y. Wang, C. Beckermann, A two-phase mixture model of liquid-gas flow and heat transfer in porous media. Part II: Application to pressure-driven flow adjacent to a vertical heated plate, *Int. J. Heat Mass Trans.* 36(11) (1993) 2759-2768.
7. C.Y. Wang, C. Beckermann, Boundary-layer analysis of buoyancy-driven two-phase flow in capillary porous media, *J. Heat Transfer*, 117 (1995) 1082-1087.
8. V.X. Tung, V.K. Dhir, Experimental study of boiling heat transfer from a sphere embedded in a liquid-saturated porous medium, *J. Heat Transfer*, 112 (1990) 736-743.
9. Kutateladze, S.S., Hydromechanical model of the crisis of boiling under conditions of free convection, *J. Tech. Phys. USSR.* 20(11) (1950) 1389-1392.
10. M. Monde, H. Kusada, H. Uehara, Critical heat flux during natural convection boiling in vertical rectangular channels submerged in saturated liquid, *ASME J. Heat Transfer*, 104 (1982) 300-303.

6.2.10. Figures

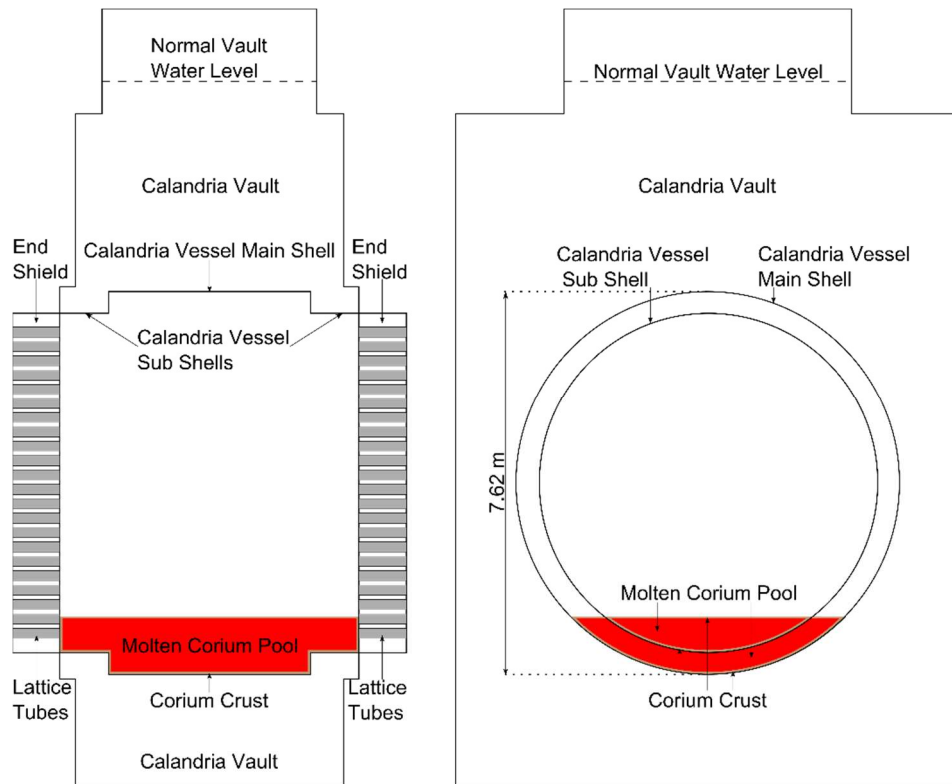


Figure 1: CANDU Reactor during In-Vessel Retention



Figure 2: Heating Plate Assembled with Stainless Steel Housing (Left), and Installed in Apparatus during Test Preparations (Right) [5]

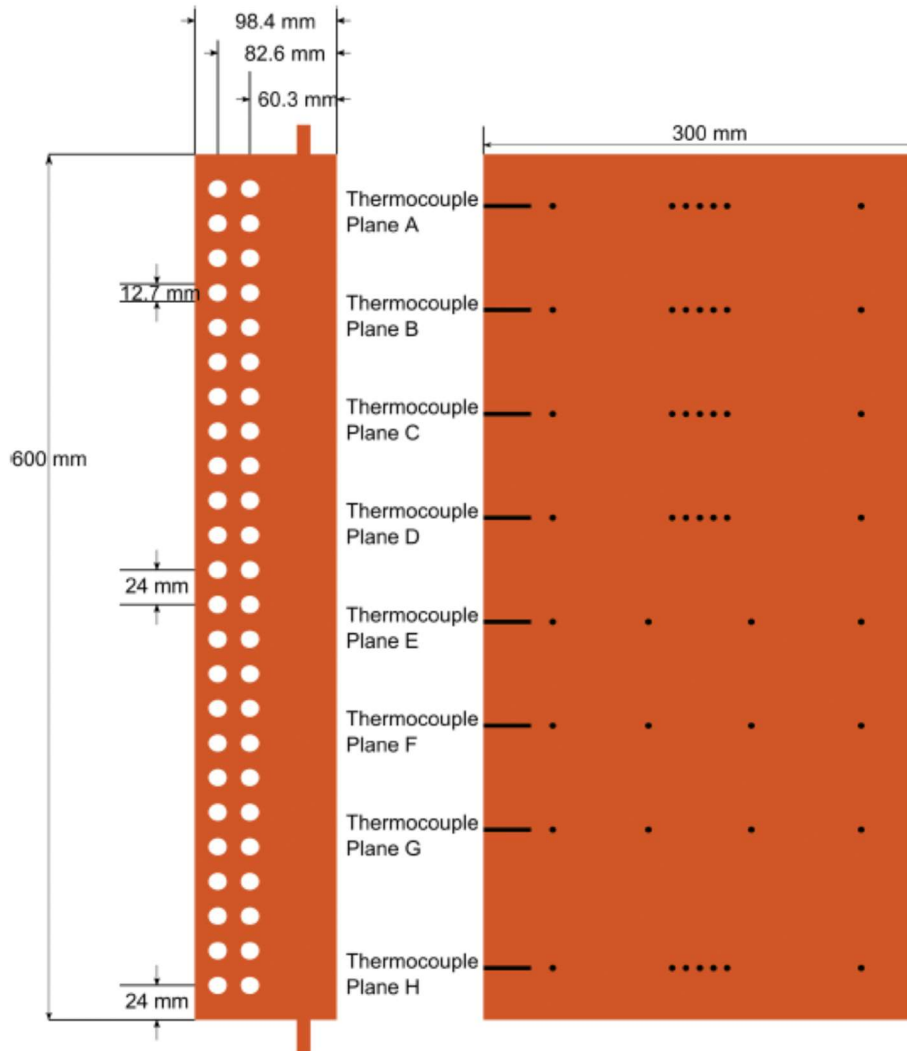


Figure 3: Heating Plate Geometry: Cross Section (L) and View from Rear (R) [5]

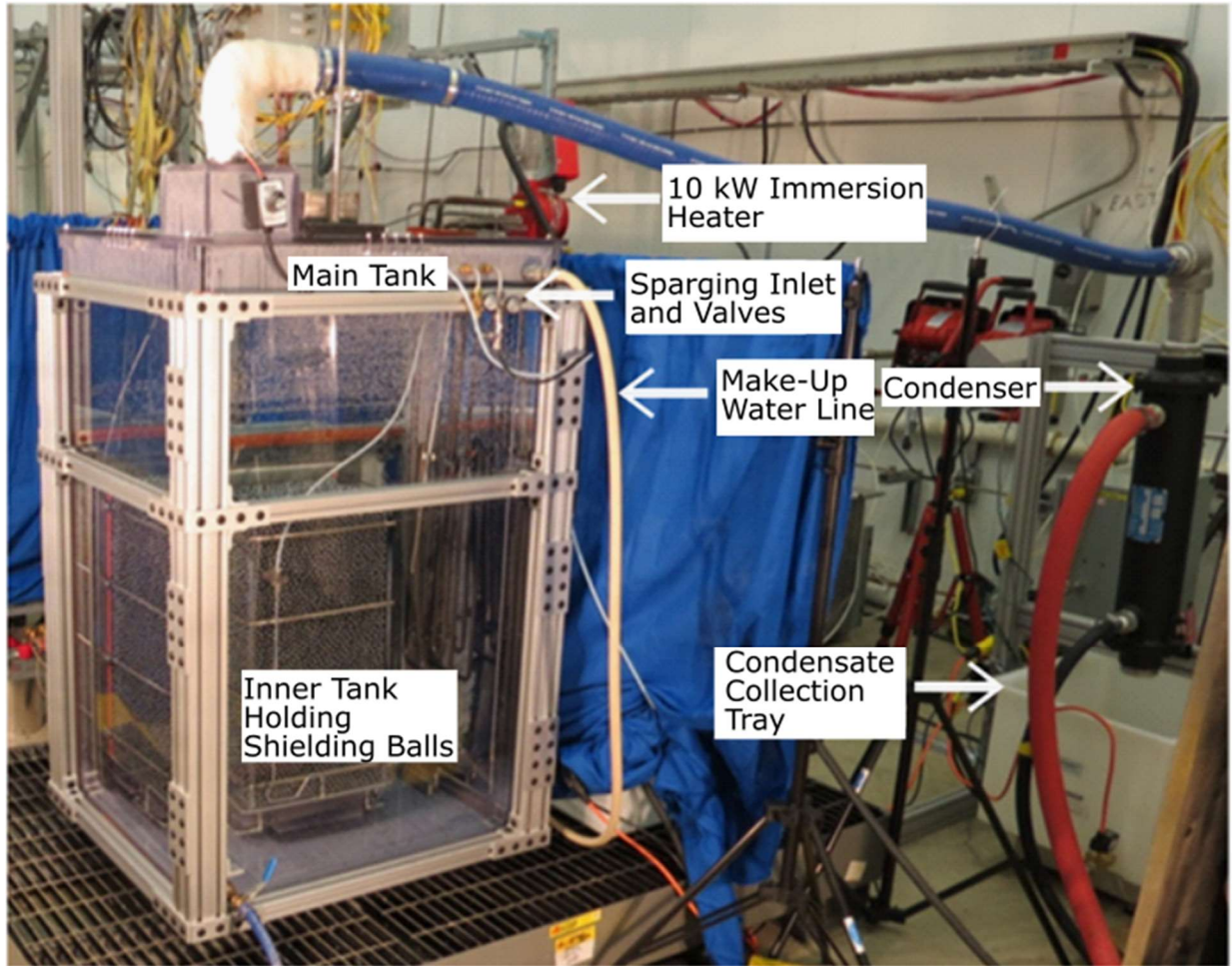


Figure 4: Experimental Apparatus [5]

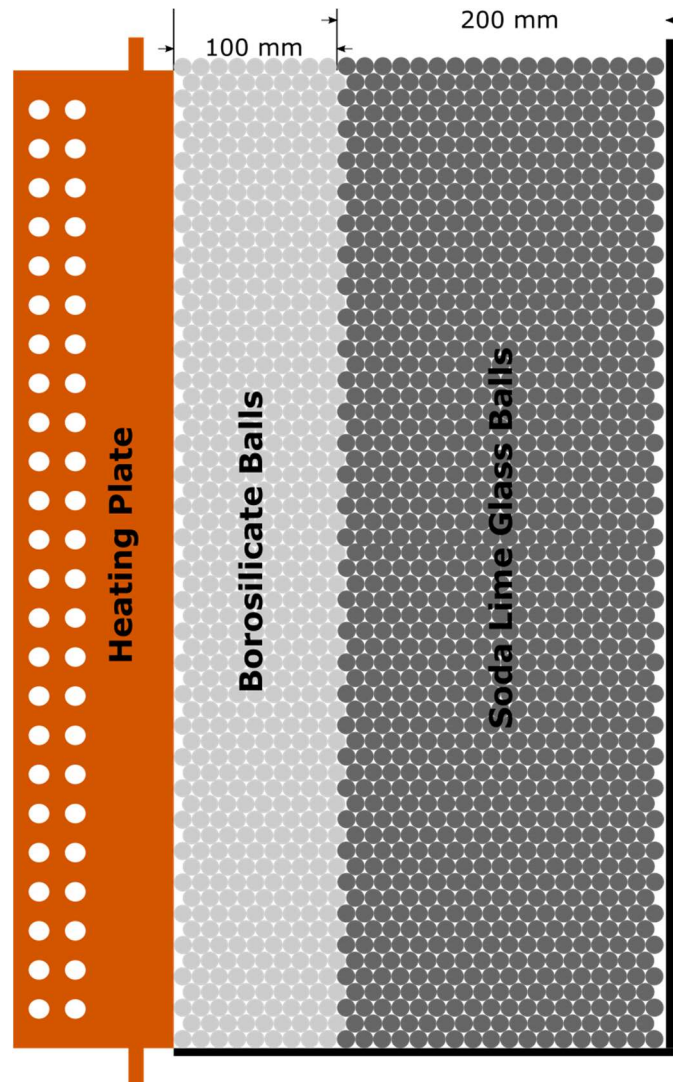


Figure 5: Configuration of Borosilicate and Soda Lime Glass Shielding Balls

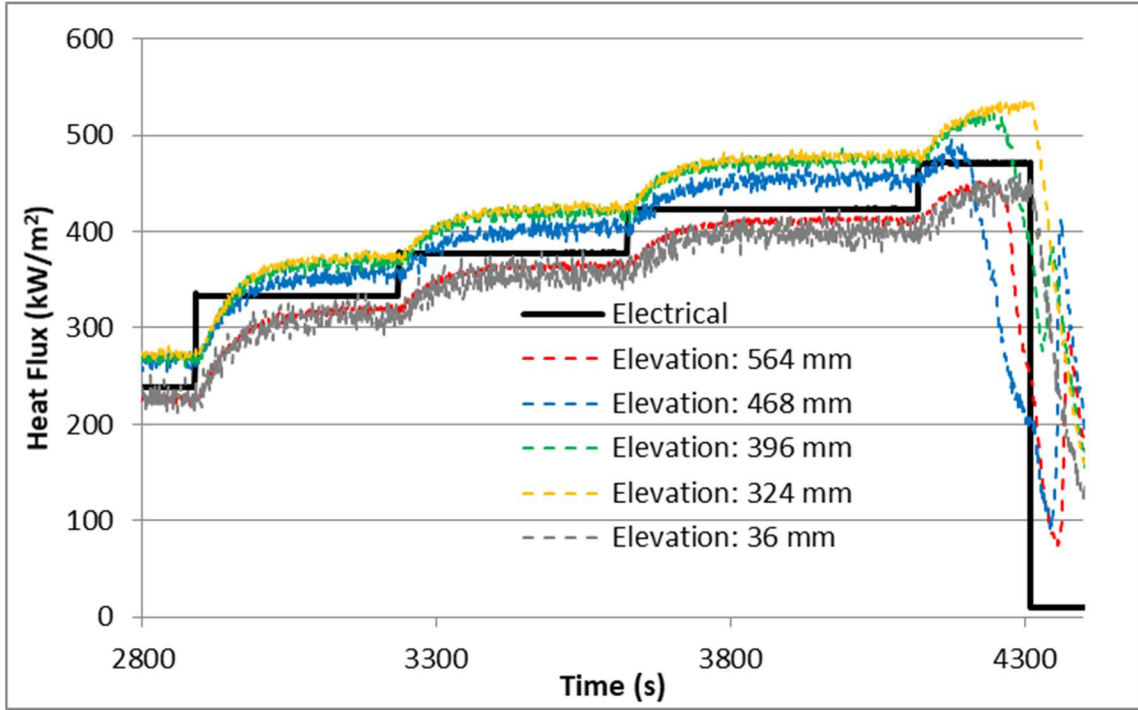


Figure 6: Heat Flux Calculated via Electrical Power, and Temperature Gradient at Various Elevations: Test ES-BP-9-1

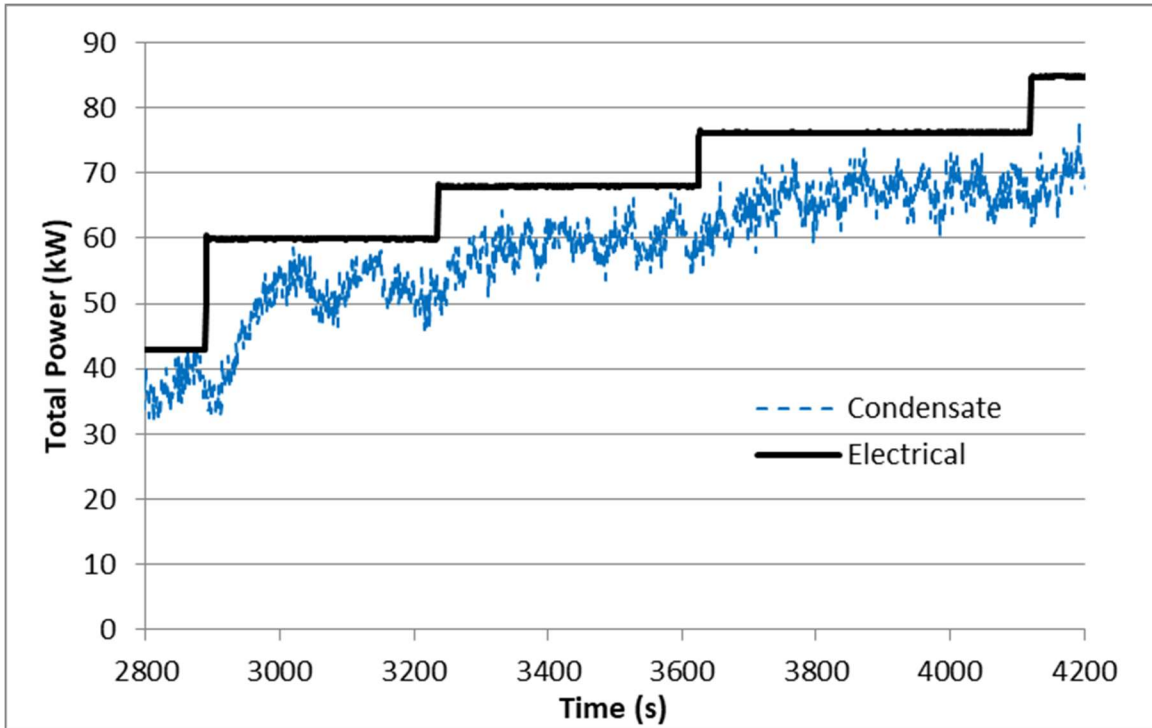


Figure 7: Total Power Calculated via Electrical Power, and Condensate Measurements: Test ES-BP-9-1

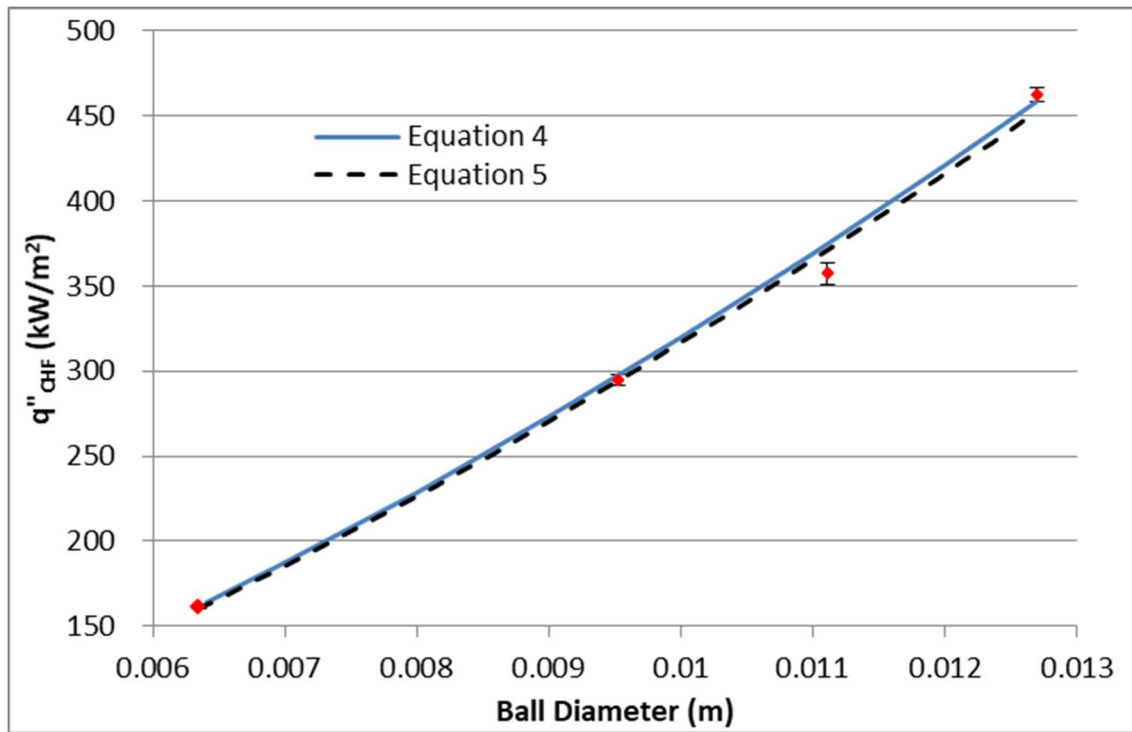


Figure 8: Critical Heat Flux as a Function of Shielding Ball Diameter

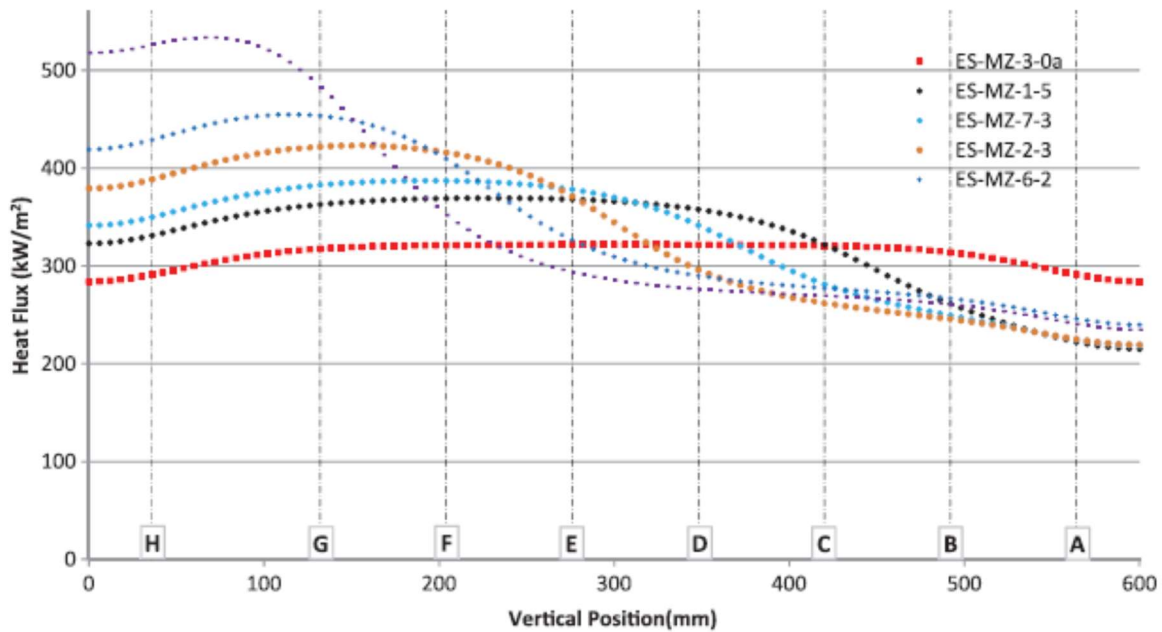


Figure 9 Heat Flux as a Function of Elevation during Nucleate Boiling, as Predicted using Finite Element Simulations [5]

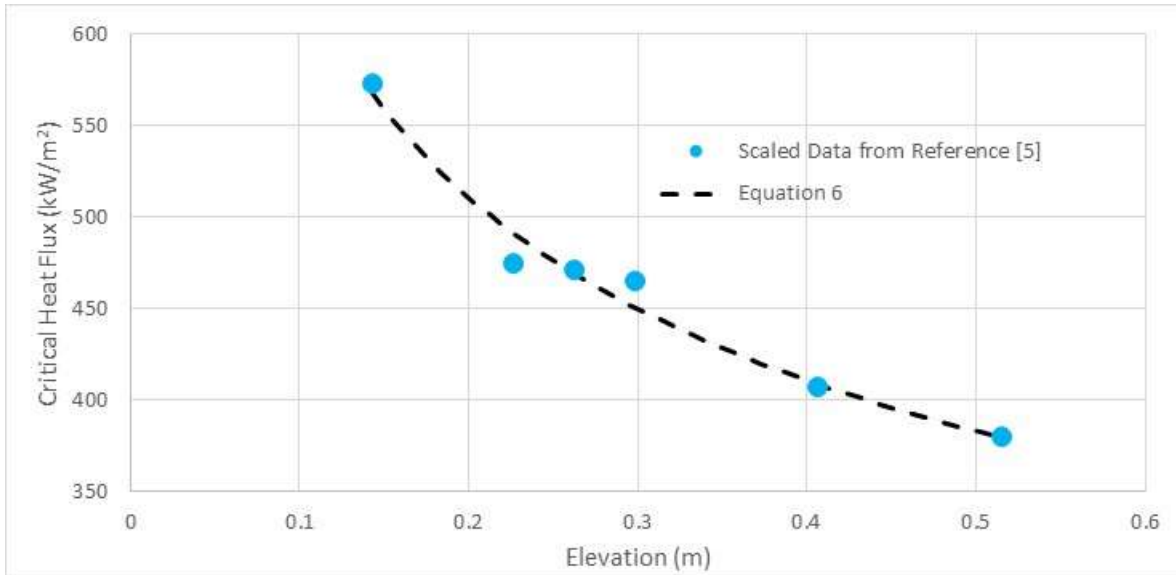


Figure 10: Wall Elevation Data Scaled from Reference [5], Compared to Equations 6 (Evaluated at a Shielding Ball Diameter of 0.0111 m)

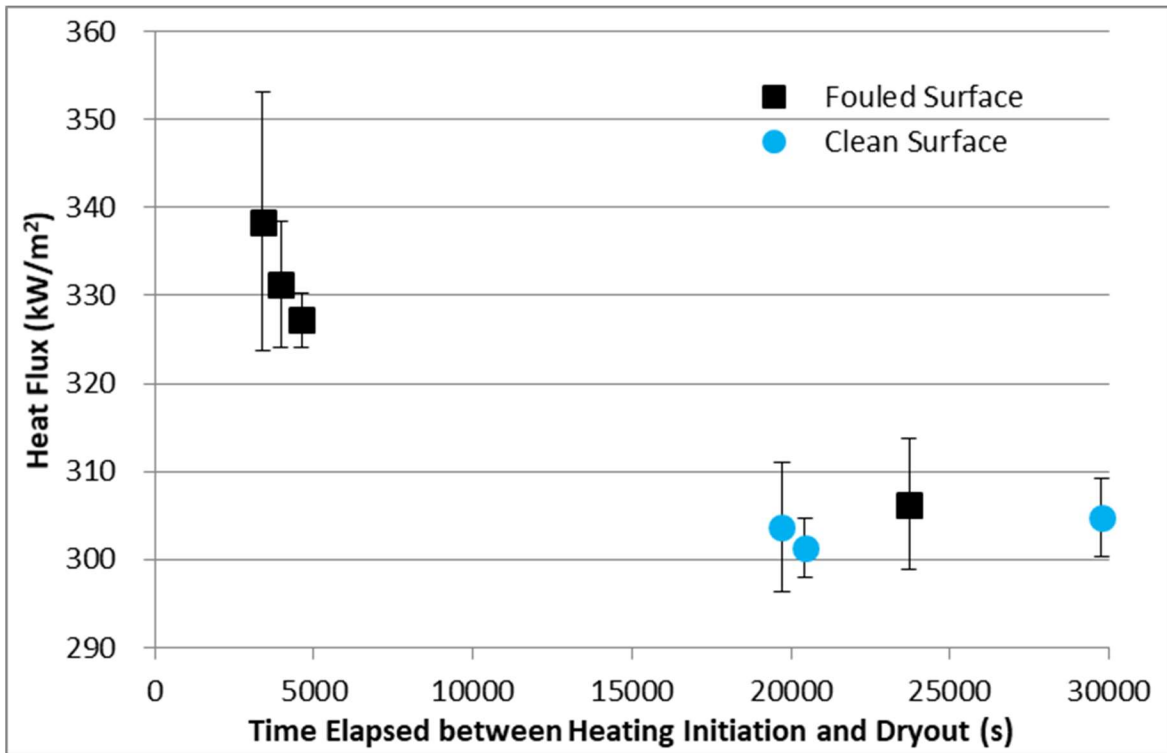


Figure 11 Dependence of CHF on Surface Conditions: Test Series ES-BP-1 (Initially Clean) vs. Test Series ES-BP-3 (Initially Fouled), Tests Performed Using Borosilicate Shielding Balls

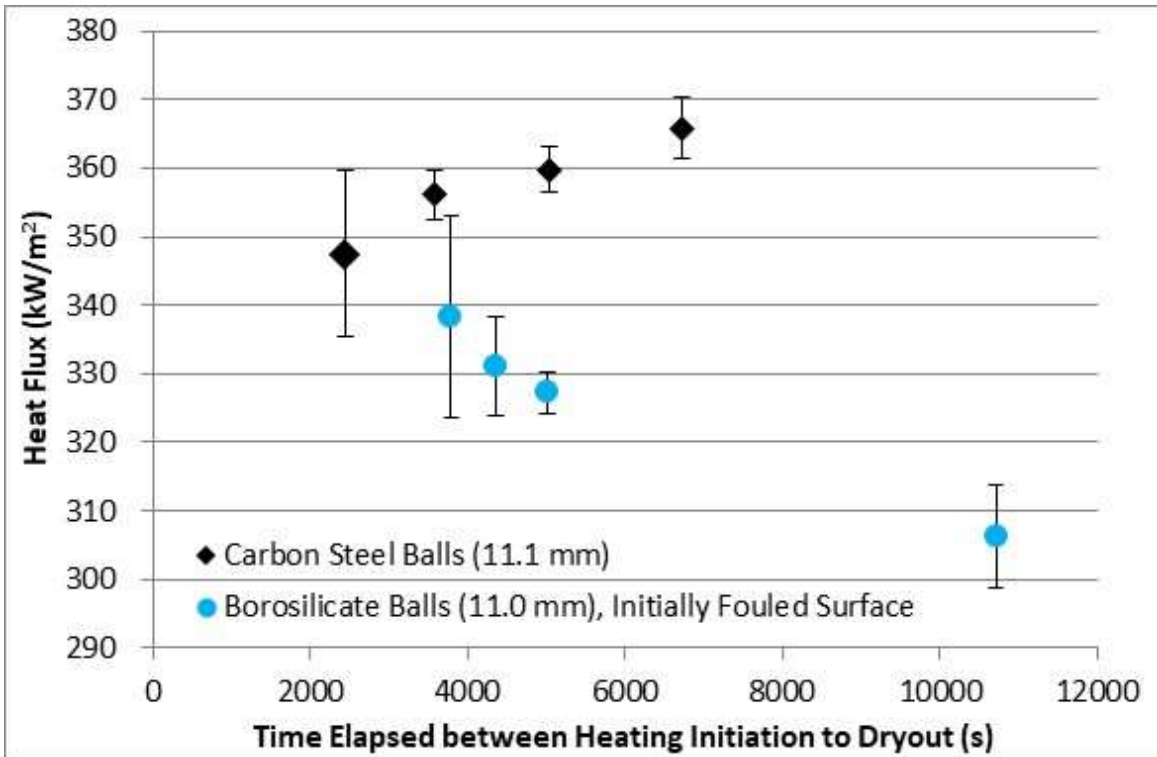


Figure 12: Comparison of CHF with High and Low Shielding Ball Thermal Conductivity

## 7. Conclusions

### 7.1. Summary of Work and Contributions to Knowledge

Critical heat flux on the surface of the calandria tubesheet facing the end shield cavity is a phenomenon with the potential to decisively impact IVR; which itself represents an important bifurcation point in the progression of a severe accident. At the outset of the work presented in this thesis, the knowledge base permitting prediction of the CHF in this location was very poor. This was reflected in a PIRT exercise predating work on this thesis, which found CHF in the end shield to be a phenomenon with both high importance and a high uncertainty [11]. This undesirable situation has been ameliorated through progress toward the overarching objective of this thesis outlined in Section 1.3: the generation of a model of critical heat flux on the surface of a calandria tubesheet facing the end shield cavity during IVR in a CANDU reactor, having the following characteristics:

1. Predictive ability across the range of all parameters relevant to the reactor scenario;
2. Empirical validation across a range of experimental data;
3. Identified and explained differences and similarities to knowledge base applicable to similar systems; and
4. To the extent practicable, formulation from well-established physical laws (i.e. a mechanistic model).

A series of six subordinate objectives are summarized in Table 5. Significant progress has been made in addressing these, including an empirical correlation of CHF accounting for two key variables.

Section 4 presents the results of a series of experiments quantifying the CHF and its dependence on elevation (or heating surface height). In addition, this section presented qualitative observations, and a comparison of the results to literature pertaining to related phenomena. The experiments were performed using an apparatus designed to represent the key features of the system as faithfully as was practicable, with a thick copper block holding embedded cartridge heaters representing the calandria tubesheet to the full height of the anticipated contact between the corium crust and the calandria tubesheet in the reactor case. The heat delivered to each cartridge heater was varied, to produce a spatially-dependent exiting heat flux distribution, permitting simulation of a plates of various heights. A conservatively-derived, empirical correlation of CHF as a function of elevation was presented (Section 4, Equation 5), constituting an output of significant utility for safety analysis.

$$q''_{CHF} \left[ \frac{kW}{m^2} \right] = -519.4 \left[ \frac{kW}{m^3} \right] z [m] + 539.6 \left[ \frac{kW}{m^2} \right] \text{ for } 0.058 m < z < 0.398 m \quad \begin{array}{l} \text{(Section 4,} \\ \text{Equation 5)} \end{array}$$

The value of CHF was observed to increase throughout the test campaign. Qualitative observation led to the hypothesis that iron oxide particles produced on the shielding balls become suspended in water and deposited on the heating surface, affecting CHF. This hypothesis is further explored in Section 6.

Section 5 presents an investigation into the hydrodynamics of the end shield cavity during IVR, using the air barbotage technique. Air was injected through a perforated plate representing the calandria tubesheet, into a simulated end shield cavity. A range of parameters were varied, and visual observations of the system were made. The primary observations are summarized below:

- Helmholtz waves form without shielding balls, with shielding balls of all diameters, and at all equivalent heat fluxes studied (a noted commonality with related literature [45]);
- Within the range studied, shielding ball diameter does not significantly impact the thickness of the two-phase region;
- The thickness of the two-phase region grows approximately linearly with elevation;
- At a given elevation, the thickness of the two-phase region grows with equivalent heat flux; and
- Lateral entrainment of water into the two-phase region was observed.

The findings presented in Section 5 constitute a first step toward a detailed understanding of the previously-unexamined hydrodynamic conditions in a CANDU end shield during IVR. Future lines of enquiry are suggested, including the use of x-ray densitometry to quantify the liquid and gas phase distribution within the two-phase region [71].

Section 6 presents the results of a series of experiments quantifying CHF and its dependence on shielding ball diameter. The impact of heating surface conditions, and thermal conductivity of shielding balls are also explored. The experiments were performed using the same apparatus presented in Section 4, but varying the characteristics of the shielding balls abutting the heating surface. The results permitted development of an empirical, best estimate correlation of CHF as a function of shielding ball diameter (Section 6, Equation 5). The exponential relation between CHF and shielding ball diameter was found to be similar to that predicted by an analytically-derived formulation for a related scenario [55][56].

$$q''_{CHF} \left[ \frac{W}{m^2} \right] = C_2 \cdot d^{3/2} [m], \quad 0.00635m \leq d \leq 0.0127m \quad (\text{Section 6, Equation 5})$$

$$C_2 = 3.16 \cdot 10^8, \quad R^2 = 0.994$$

This was combined with the data presented in Section 4 to produce a best estimate correlation of CHF as a function of both elevation and shielding ball diameter, in both dimensional (Section 6, Equation 6) and dimensionless (Section 6, Equation 13) form.

$$q''_{CHF} \left[ \frac{W}{m^2} \right] = C_3 \cdot d^{3/2} [m] \cdot L^{-0.314} [m], \quad 0.00635m \leq d \leq 0.0127m, \quad (\text{Section 6, Equation 6})$$

$$0.144m \leq L \leq 0.516m, \quad C_3 = 2.63 \cdot 10^8, \quad R^2 = 0.977$$

$$Ku = \frac{C_4 \varepsilon^{1/4} Bo_k^{3/4} Bo_L^{-0.157}}{Oh_L \left[ \rho_g / \rho_l \right]^{1/2}} \quad (\text{Section 6, Equation 13})$$

This constitutes a significant advancement in the ability of safety analysts to predict CHF in the end shield cavity.

Additional findings included:

- Observations supporting the hypothesis that iron oxide particle deposition on the boiling surface increases CHF; and
- Measurements of CHF indicating the absence of significant sensitivity of CHF to shielding ball thermal conductivity.

The observations made in Section 6, along with those in Sections 4 and 5 were used to suggest the form of a semi-mechanistic model of CHF in this geometry, accounting for elevation, spatially-varying heat flux distribution, and shielding ball diameter.

Insight into the mechanism of CHF can be drawn from the following observations:

- The dependence of CHF on heating surface conditions indicates that liquid is delivered to the heating surface up to the highest observed value of CHF. This implies that the near-wall liquid-phase saturation is greater than zero at CHF in the range of relevant parameters studied.
- The dependence of CHF on elevation indicates that near-wall hydrodynamic conditions (including liquid-phase saturation and velocity) are also important.

These observations suggest that the mechanism of CHF is to be found in the immediate vicinity of the heating surface. The heat flux at which this mechanism manifests is a function of near-field hydrodynamics, which are influenced by far-field parameters including ‘upstream’ vapour generation and the characteristics of the packed bed of shielding balls.

These insights suggest two hypotheses regarding the mechanism of CHF:

1. The mechanism of CHF may be the formation and expansion of ‘hot spots’ formed at or near the points of contact between the shielding balls and the heating surface.
  - The ‘hot spots’ would be regions where heat transfer has degraded due to the flow restriction between the heating surface and shielding ball surfaces or in the stagnation or recirculation regions immediately downstream.
  - These ‘hot spots’ may achieve a steady state under some conditions, with heat being conducted parallel to the surface to regions exhibiting a higher heat transfer coefficient. ‘Hot spot’ expansion would then occur following a change of conditions, such as local hydrodynamics or heat flux exiting the heating surface.
  - The associated CHF criterion would presumably be a function of factors including: near-wall liquid-phase saturation and velocity, shielding ball diameter, heating surface conditions, and the thermal conductivity and thickness of the heating plate (the calandria tubesheet in the reactor case).
2. The near wall hydrodynamic conditions may exhibit nontrivial periodic variations coupled to the Helmholtz waves observed at the limit of the liquid-vapour plume, impacting the CHF criterion. If this is the case:
  - Steady state analyses of the near-wall hydrodynamic conditions and heat transfer within the heating plate may be insufficient to adequately represent the CHF criterion.
  - The thermal diffusivity of the heating plate material may be important, in addition to its thermal conductivity and thickness.

The value of the work presented in this thesis can be evaluated from multiple perspectives:

1. Progress toward the overarching objective of the thesis (see Section 1.3)
  - As summarized in Table 5, six subordinate objectives were identified whose completion would result in achievement of the overarching objective. Significant progress was made toward completion of five of these.
  - As a consequence of the results presented in the thesis, it was possible to identify a concrete set of steps to completion of the overarching objective. These steps are outlined in Section 6.2.6, and discussed in Section 7.3.
2. Improvement in the ability of safety analysts to assess IVR in CANDU reactors (Section 7.2)
  - Introduction of the first predictive capability for CHF on the surface of the calandria tubesheet during IVR (addressing a high importance, high uncertainty item identified in a pre-existing CANDU PIRT exercise [11])
  - Quantification of the sensitivity of CHF to two key parameters (heating surface height, and shielding ball diameter)
3. Contributions to more broadly-defined subjects, in particular externally-heated porous media.
  - A surprising similarity is noted between the empirically-derived dependence of CHF on shielding ball diameter, and predictions for capillary porous media [55],[56]. Pending clarification of the source of this agreement, this observation may constitute a step toward extension of the range of applicability of existing correlations of CHF in externally-heated porous media.
  - Other differences and similarities are noted, including the dependence of CHF on heating surface height, and the conclusion that CHF in this geometry with a coarse packed bed is not a function of a flooding limit (consistent with observations for hot spheres embedded in porous media [59]).

The contents of this thesis represent significant progress in ameliorating the previously poor state of understanding of CHF on the surface of a calandria tubesheet facing the end shield cavity.

## 7.2. Recommendations for Safety Analysis

As noted in Section 7.1, end shield CHF constituted a significant gap in the knowledge base pertaining to CANDU severe accidents prior to the work presented in this thesis. In the interest of addressing this shortcoming, it is specifically recommended that Equation 6 from Section 6 be used in safety analyses. It is expected that this correlation is more representative of the reactor case than any alternatives currently available in the knowledge base; however, there are three primary sources of potential scaling distortion that should be considered by analysts:

1. Surface conditions:
  - Provided that oxide particle deposition is significant in the reactor case, the copper plate used in the experiments (when fouled) would present minimal distortion of the CHF relative to the reactor's stainless steel 304L calandria tubesheet.
  - The maximal heat fluxes exiting the calandria tubesheet would be established only after a lengthy period of boiling in the end shields, while the TDB temperature increases following moderator depletion. It is anticipated that in most scenarios, significant oxide formation and particle deposition on the calandria tubesheet would occur in the

intervening period. Following this fouling process, it is anticipated that the CHF would be significantly higher on the calandria tubesheet surface than on the relatively clean copper heating surface represented by Equation 6 of Section 6. An illustration of this effect can be found in Figure 7 of Section 4, where an increase of approximately 18% in the CHF was observed between the test with the cleanest and most fouled surfaces.

2. Lattice tubes:

- It is anticipated that the presence of the lattice tubes would impact CHF via local hydrodynamics, due to both the influence of these obstructions on liquid-phase saturation and velocity, and the generation of vapour on the surface of the lattice tubes. In addition, the porosity of the packed bed in the immediate vicinity of the lattice tube – calandria tubesheet junction may be reduced. The results presented in this thesis did not quantify the net impact of these factors; however, it is the judgement of the author that CHF would not be drastically affected.
- It can be assumed that the heat flux exiting the calandria tubesheet would be distorted in the immediate vicinity of the lattice tube – calandria tubesheet junction. The impact of steep heat flux gradients on CHF in this geometry is not well-understood. In addition, the knowledge base is at present devoid of predictions of these localized distortions.

3. Macroscopic heat flux spatial distribution:

- In the reactor case, it is anticipated that there would be significant variation with elevation, with the maximum value located somewhat above the midpoint between the bottom and top of the region of contact with the corium crust [19]. Given the assumption of uniform upstream heat flux utilized in Equation 6 of Section 6, it is anticipated that the correlation would under-predict CHF below the elevation of maximum heat flux, and over-predict it above. The non-conservative distortion is judged by the author to be modest, such that safety analysis would only be impacted in the event that margins to CHF are relatively small.

These sources of potential scaling distortions are the subject of recommendations for future work, discussed in Section 7.3.

### 7.3. Recommendations for Future Work

While the work presented in this thesis constitutes a significant advancement toward the overarching objective of the thesis, recommendations for future work are proposed to further this progress. The first steps recommended are those outlined in Section 6.2.6:

1. Quantify the function  $s(q'', L, d)$

- This can be accomplished through air barbotage experiments such as those presented in Section 5, with the volumetric ratio of liquid and air quantified using either x-ray or gamma ray densitometry. Such work has begun [71], but is not yet completed.
- Heated experiments could also be performed, substituting borosilicate shielding balls (as in Section 6), to avoid the challenge of photon attenuation via carbon steel shielding balls. This approach could be taken as a means of quantifying distortions resulting from the use of air barbotage experiments as presented in Section 5 and Reference [71].

2. Quantify the function  $q''_{CHF}(s,d)$ 
  - Using the function  $s(q'',L,d)$ , the data presented in Sections 4 and 6 could be utilized to calculate the local heat flux and saturation at the position where dryout occurred. This could then be used to quantify  $q''_{CHF}(s,d)$ , for a given set of surface conditions.
3. Subsequently, further investigations may be called for to clarify the dependence of  $q''_{CHF}(s,d)$  on surface conditions of relevance to the calandria tubesheet during IVR.
  - It is recommended that this include the performance of experiments using a stainless steel heating surface, with a wall thickness at least on the order of the shielding ball diameter.
  - The effect of surface roughness, fouling by oxides produced on the shielding balls, and contact angle should be quantified through surface treatments and characterization.

Completion of steps 1 and 2 would yield a semi-mechanistic correlation of CHF in a CANDU end shield as a function of elevation, spatially-varying heat flux distribution, and shielding ball diameter. Completion of step 3 would reduce the uncertainty of predictions of this correlation. It is recommended that steps 1 and 2 be pursued in future work. Once a semi-mechanistic model has been developed, the importance of further uncertainty reduction can be assessed, and a decision on the pursuit of step 3 can be made.

As noted in Section 7.1, advancement from this semi-mechanistic correlation to a more fully mechanistic model of CHF may be possible through the proposal and characterization of a calandria tubesheet-centred mechanism, with the hot spot spreading model constituting a strong candidate.

It is expected that a hot spot spreading model would present testable hypotheses, including the effects of wall thickness and thermal properties. Application of a hot spot spreading model to the calandria tubesheet would necessarily require inclusion of the local saturation. It is thus recommended that establishment of a semi-mechanistic model correlating CHF to local void fraction be prioritized before significant effort is expended in developing a more fully mechanistic model. A potential avenue of progress that could be developed with relatively modest effort would begin with recognition that the relationship of CHF (or  $Ku$ ) to dimensionless parameters is likely a function of the mechanism of CHF. It is possible that these relationships are consistent with those evident in different geometries, provided that the mechanism of CHF remains unchanged. If this is true, further insight into the mechanism of CHF could be drawn through comparison of the dimensionless parameters found in Equation 13 of Section 6 to a broad range of correlations pertaining to more extensively-studied geometries for which a mechanism of CHF has been established.

The following steps are recommended to address the scaling distortions potentially affecting safety analyses, discussed in Section 7.2:

1. Surface conditions:
  - As discussed in Section 7.2, the state of the calandria tubesheet surface in most accident scenarios is likely well represented by the experiments forming the basis of Equation 6 of Section 6. To the extent that further work is required, the final step of the semi-mechanistic model development path outlined above would likely suffice.
2. Lattice tubes:
  - Adequate quantification of the impact of lattice tubes would likely require an experiment representing both the geometry of the calandria tubesheet – lattice tube

system and a heat flux distribution that is reasonably representative of the reactor case. Such experimental efforts should be preceded by analytical efforts quantifying the heat flux distribution in the immediate vicinity of the calandria tubesheet – lattice tube junction.

3. Macroscopic heat flux distribution:

- The establishment of a semi-mechanistic model through the process outlined above would address the effect of spatial heat flux distribution on CHF.
- Alternatively, it is expected that a purely empirical correlation between CHF and spatially-varying upstream heat flux could be established through further analysis of the non-uniform test cases summarized in Table 3 of Section 4.

Finally, it is recommended that CHF experiments be performed using an apparatus similar to that utilized in Sections 4 and 6, studying the dependence of CHF on shielding ball diameter from the range of capillary porous media to the coarse porous media that are the focus of this thesis. Such research would present an opportunity to investigate the effect on CHF trends of the magnitude of capillary forces relative to viscous and inertial forces. In addition, it would present the opportunity for direct comparison to existing literature regarding externally heated capillary porous media.

## 8. Works Cited

- [1] E. Bush, D.S. Lemmen, editors, “Canada’s Changing Climate Report”, Government of Canada, Ottawa, Ontario, 2019.
- [2] International Energy Agency, “Energy Technology Perspectives 2020”, Revised February 2021.
- [3] T. Nitheanandan, M.J. Brown, “A Historical Review of Nuclear Contribution to the Ontario Energy Mix”, The 19<sup>th</sup> Pacific Basin Nuclear Conference, Vancouver, British Columbia, Canada, August 24-28, 2014.
- [4] World Nuclear Association, “The Harmony Programme”, <https://world-nuclear.org/our-association/what-we-do/the-harmony-programme.aspx>, updated March 12, 2019.
- [5] J. Garland, “The Essential CANDU, A Textbook on the CANDU Nuclear Power Plant Technology” (Chapter 2 – Genealogy of CANDU Reactors), University Network of Excellence in Nuclear Engineering (UNENE) ISBN 0-9730040, September 2016.
- [6] International Atomic Energy Agency, “INES the International Nuclear and Radiological Event Scale User’s Manual – 2008 Edition”, Emended Version, IAEA Vienna, Austria, March 2013.
- [7] D. Smyth, “An objective nuclear accident magnitude scale for quantification of severe and catastrophic events”, DOI:10.1063/PT.4.0509, Physics Today, 12 December 2011.
- [8] J.C. Luxat, “Thermalhydraulic Aspects of Progression to Severe Accidents in CANDU Reactors”, Nuclear Technology, Vol. 167, No. 1, pp 187-210, July 2009.
- [9] C. Blahnik, M.J. Brown, J.C. Luxat, T. Nitheanandan, S.M. Petoukhov, “Perspective on Analyses of Core Damage in CANDU Reactors”, 24<sup>th</sup> Nuclear Simulation Symposium, Ottawa, Ontario, Canada, October 14-16, 2012.
- [10] T. Nitheanandan and M.J. Brown, “Backup and Ultimate Heat Sinks in CANDU Reactors for Prolonged SBO Accidents”, Nuclear Engineering and Technology, Vol. 45 No. 5, 2013 October
- [11] T. Nitheanandan, “Severe Accident R&D for Enhanced CANDU 6 Reactors”, 18<sup>th</sup> Pacific Basin Nuclear Conference (PBNC 2012), BEXCO, Busan, Korea, March 18-23, 2012.
- [12] S. Nijhawan, “Unmet Challenges to Successfully Mitigating Severe Accidents in Multi Unit CANDU Reactors”, Proceedings of the 28<sup>th</sup> International Conference on Nuclear Engineering ICONE28, Anaheim, California, USA, August 2-6, 2020.
- [13] S. Nijhawan, Y. Song, “Simulation of Severe Accident Progression using ROSHNI – a New Integrated Simulation Code for PHWR Severe Accidents”, Proceedings of the 28<sup>th</sup> International Conference on Nuclear Engineering ICONE28, Anaheim, California, USA, August 2-6, 2020.
- [14] E.M. Lessard, G. Young, M. Britt, N. Yashinskie, M. Dickerson, “Calandria Tube Buckling during a Reactor Core Collapse”, 41<sup>st</sup> Annual Conference of the Canadian Nuclear Society and 46<sup>th</sup> Annual CNS/CAN Student Conference, June 5 – 8, 2022.

- [15] C. Song, E. Lessard, J. Spencer, “Finite Element Analysis of Calandria Tube Failure during a Reactor Core Collapse”, 41<sup>st</sup> Annual Conference of the Canadian Nuclear Society and 46<sup>th</sup> Annual CNS/CAN Student Conference, June 5 – 8, 2022.
- [16] T.G. Theofanous, C. Liu, S. Additon, S. Angelini, O. Kymalainen and T. Salmassi, “In-vessel coolability and retention of a core melt”, Nuclear Engineering and Design 169 (1997) 1-48
- [17] O. Kymalainen, H. Tuomisto and T.G. Theofanous, “In-vessel retention of corium at the Loviisa plant”, Nuclear Engineering and Design 169 (1997) 109-130
- [18] D.L. Luxat and J.C. Luxat, Calandria vessel integrity under severe accident loads, Trans. SMiRT 19, Paper #J07/2, Toronto, ON, Canada, 2007 August
- [19] R. David, “Computational Fluid Dynamics Study of a Corium Pool in a CANDU Calandria”, CNL Nuclear Review, 6, 2, 175 (2017); <https://pubs.cnl.ca/doi/10.12943/CNR.2016.00044>.
- [20] S.V. Prasad, A.K. Nayak, P.P. Kulkarni, P.K. Vijayan, and K.K. Vaze, Study on heat removal capability of calandria vault water from molten corium in calandria vessel during severe accident of a PHWR, Nuc. Eng. Design, Vol. 284, pp. 130-142, 2015.
- [21] S.V. Prasad and A.K. Nayak, In-calandria retention of corium in PHWR: experimental investigation and remaining issues, J. Nuc. Eng. Radiation Sci., 2017 January, doi: 10.1115/1.4035691
- [22] R. David, “Calculation of Heat Fluxes Exiting a CANDU Calandria During In-Vessel Retention”, Nuclear Technology (2019), 205:11, 1488-1494, DOI: 10.1080/00295450.2019.1597581.
- [23] R. David, “Heat transfer at the step of a CANDU calandria during a severe accident”, Kerntechnik 86 (2021) 5, 338-342.
- [24] J.T. Rogers, D.A. Meneley, C. Blahnik, V.G. Snell, and S. Nijhawan, Coolability of severely degraded CANDU cores, Heat and Mass Transfer in Severe Nuclear Reactor Accidents, pp. 317-334, Kusadasi, Turkey, 1995 May
- [25] S. Nicolici, D. Dupleac, and I. Prisecaru, Numerical analysis of debris melting phenomena during late phase CANDU 6 severe accident, Nuc. Eng. Design, Vol. 254, pp. 272-279, 2013
- [26] J. Spencer, A.D. Quastel, “Freezing Plug Formation in PHWR Calandria Vessel Penetrations”, The 9<sup>th</sup> European Review Meeting on Severe Accident Research (ERMSAR2019), Prague, Czech Republic, March 18-20, 2019.
- [27] Tong, L. S., and Y. S. Tang. Boiling Heat Transfer and Two-Phase Flow. 2nd ed. New York, NY: Francis & Taylor, 1997.
- [28] Y. Y. Hsu, On the Size Range of Active Nucleation Cavities on a Heating Surface”, J. Heat Transfer. Aug 1962, 84(3): 207-213.
- [29] W.M. Rohsenow, J.R. Hartnett, & Y.I. Cho (1998). Handbook of Heat Transfer (3rd Edition). McGraw Hill.
- [30] T.G. Theofanous, J.P. Tu, A.T. Dinh, T.N. Dinh, The boiling crisis phenomenon part I: nucleation and nucleate boiling heat transfer, Exp. Therm. Fluid Sci. 26 (2002) 775–792.

- [31] T.G. Theofanous, J.P. Tu, A.T. Dinh, T.N. Dinh, The boiling crisis phenomenon part II: nucleation and nucleate boiling heat transfer, *Exp. Therm. Fluid Sci.* 26 (2002) 793–810.
- [32] Incropera, De Witt., *Fundamentals of Heat and Mass Transfer*, 3rd ed., John Wiley & Sons, 1990.
- [33] Zuber, N., *Hydrodynamic Aspects of Boiling Heat Transfer*, PhD Thesis, Dept. Of Eng., UCLA
- [34] G. Taylor, The Instability of Liquid Surfaces when Accelerated in a Direction Perpendicular to their Planes. I. *Proceedings of the Royal Society of London. Series A, Mathematical and Physical Sciences*, Vol. 201, No. 1065. (Mar. 22, 1950), pp. 192-196.
- [35] Lamb, H., *Hydrodynamics*, 6th ed., Dover Publications, Inc., 1945.
- [36] Lienhard, J.H., and Dhir, V.K., 1973, *Extended Hydrodynamic Theory of the Peak and Minimum Heat Fluxes*, NASA CR-2270.
- [37] Haramura, Y., and Katto, Y., 1983, “New Hydrodynamic Model of Critical Heat Flux Applicable Widely to both Pool and Forced Convection Boiling on Submerged Bodies in Saturated Liquids,” *Int. J. Heat Mass Transf.*, 26, pp. 379–399.
- [38] Y. Katto, S. Yokoya, Behavior of a vapor mass in saturated nucleate and transition pool boiling, *Heat Transfer – Japan.*, Res. 5(2), 45-65 (1965).
- [39] W. M. Rohsenow, P. Griffith, Correlation of Maximum Heat Flux Data for Boiling of Saturated Liquids, *Chem. Eng. Prog. Symp. Series (52)*: 47-49, 1956.
- [40] V.K. Dhir, S.P. Liaw, Framework for a Unified Model for Nucleate and Transition Pool Boiling, *J. Heat Transfer (111)*: 389-399, 1983.
- [41] N.I. Kolev, How accurately can we predict nucleate boiling? *Exp. Therm. Fluid Sci.* 10 (1995) 370–378.
- [42] Kandlikar, S.G, A Theoretical Model to Predict Pool Boiling CHF Incorporating Effects of Contact Angles and Orientation, December 2001, *Journal of Heat Transfer*, vol 123, pp. 1071-1079
- [43] Kandlikar, S.G., Steinke, M.E., 2002. Contact angles and interface behavior during rapid evaporation of liquid on a heated surface. *International Journal of Heat and Mass Transfer* 45, 3771–3780.
- [44] I.L. Pioro, W. Rohsenow, S.S. Doerffer, Nucleate pool-boiling heat transfer II: assessment of prediction methods, *International Journal of Heat and Mass Transfer* 47 (2004) 5045-5057.
- [45] A.H. Howard, I. Mudawar, Orientation effects on pool boiling critical heat flux (CHF) and modeling of CHF for near-vertical surfaces, *Int. J. Heat Mass Transfer* 42 (1999) 1665–1688.
- [46] S.H. Yang, W.P. Baek, S.H. Change, Pool boiling critical heat flux of water on small plates: effects of surface orientation and size, *International Communications in Heat and Mass Transfer*.
- [47] I.P. Vishnev, Effect of orienting the hot surface with respect to the gravitational field on the critical nucleate boiling of a liquid, *Journal of Engineering Physics*, 24 (1974), 43-48.

- [48] J. Yang, F. B. Cheung, J. L. Rempe, K. Y. Suh and S. B. Kim, "Correlations of Nucleate Boiling Heat Transfer and Critical Heat Flux for External Reactor Vessel Cooling," Proceedings ASME Summer Heat Transfer Conference, Paper No. HT2005-72334, San Francisco, CA, July 2005, 2005.
- [49] T.G. Theofanous, S. Syri, T. Salmassi, O. Kymalainen, H. Tuomisto, Critical Heat Flux Through Curved, Downward Facing Thick Walls, Nucl. Eng. Des. 151 (1994) 247–258.
- [50] Y. Katto, T. Hirao, Critical heat flux of counter-flow boiling in a uniformly heated vertical tube with a closed bottom, International Journal of Heat and Mass Transfer (1991) vol. 34, 993–1001.
- [51] Kulkarni, P. P. Rashid, M. Kulenovic, R. Nayak, A. K., Experimental investigation of coolability behaviour of irregularly shaped particulate debris bed, Nuclear Engineering and Design, 2010, VOL 240; NUMBER 10, pages 3067-3077
- [52] W. van Antwerpen, P.G. Rousseau, C.G. du Toit, Multi-sphere Unit Cell model to calculate the effective thermal conductivity in packed pebble beds of mono-sized spheres, Nuclear Engineering and Design, Volume 247, June 2012, Pages 183–201
- [53] E.M. Parmentier, "Two-phase natural convection adjacent to a vertical heated surface in a permeable medium", Int. J. Heat Mass Transfer, 22, pp. 849-855, 1979.
- [54] P. Cheng and A.K. Verma, "The effect of subcooled liquid on film boiling about a vertical heated surface in a porous medium", Int. J. Heat Mass Transfer, 24, pp. 1151-1160, 1981.
- [55] C.Y. Wang and C. Beckermann, "A two-phase mixture model of liquid-gas flow and heat transfer in porous media. Part II: Application to pressure-driven boiling flow adjacent to a vertical heated plate", Int. J. Heat Mass Transfer 36, pp. 2759-2768, 1993.
- [56] C.Y. Wang and C. Beckermann, "Boundary-layer analysis of buoyancy-driven two-phase flow in capillary porous media", J. Heat Transfer, 117, pp. 1082-1087, 1995.
- [57] V.E. Schrock, R.T. Fernandes and K. Kesavan, "Heat transfer from cylinders embedded in a liquid filled porous medium", Heat Transfer, Proc. Int. Heat Transfer Conf, Vol. 7, Pap. CT3.6., 1970.
- [58] S. Fukusako, T. Komoriya and N. Seki, "An experimental study of transition and film boiling heat transfer in liquid-saturated porous bed", J. Heat Transfer 108, pp. 117-124, 1986.
- [59] V.X. Tung and V.K. Dhir, "Experimental study of boiling heat transfer from a sphere embedded in a liquid-saturated porous medium", J. Heat Transfer, 112, pp. 736-743, 1990.
- [60] J. L. Lage, B. V. Antohe, "Darcy's Experiments and the Deviation to Nonlinear Flow Regime", ASME Journal of Fluids Engineering, September 2000, Vol. 122, pp 619-625.
- [61] KTA, Reactor Core Design of High-Temperature Gas-Cooled Reactors Part 3: Loss of Pressure through Friction in Pebble Bed Cores, (March 1981), Technical Report 3102.3, Nuclear Safety Standards Commission / KTA (Federal Republic of Germany)
- [62] R.P. Larkins, R.R. White and D.W. Jeffrey. Two-phase concurrent flow in packed beds. AIChE J. 7: 231 (1961).

- [63] Kandlikar, S.G., 2002. Fundamental issues related to flow boiling in mini-channels and micro-channels. *Exp. Thermal Fluid Sci.* 26, 389–407.
- [64] T.G. Theofanous, A.T. Dinh, *Nucleation Phenomena in Boiling, Multiphase Science and Technology*, Vol. 15, No. 1-4, pp. 349-363, 2003.
- [65] T.G. Theofanous, A.T. Dinh, High heat flux boiling and burnout as microphysical phenomena: mounting evidence and opportunities. *Multiphase Sci Technol.* 2004;18:1–26.
- [66] N. Zuber, Hierarchical, Two-Tiered Scaling Analysis, An Integrated Structure and Scaling Methodology for Severe Accident Technical Issue Resolution: Appendix D, U.S. Nuclear Regulatory Commission, Washington, D.C. 20555, NUREG/CR-5809, 1991 November
- [67] I.I. Gogonin, Influence of the Thickness of a Wall and of its Thermophysical Characteristics on the Critical Heat Flux in Boiling, *Journal of Engineering Physics and Thermophysics*, Vol. 82, No. 6, 2009
- [68] S.S. Kutateladze and V.N. Moskvicheva, “Hydrodynamics of a Two-Component Layer as Related to the Theory of Crises in the Process of Boiling”, *Soviet Technical Physics*, Vol. 4, No. 12, 1960 June
- [69] S. Narayanaswamy, “Bubble Dynamics in Barbotage and Boiling”, Thesis (Masters of Science), University of Manitoba, 1973 February
- [70] P.Y.J. Chan, “Bubble Dynamics in Combined Constant-Flow and Constant-Pressure Barbotage”, Thesis (Masters of Science), University of Manitoba, 1985 September
- [71] K. Stoev, J. Spencer, “Determination of Void Fraction by X-ray Radiography”, *Advances in X-ray Analysis*, Volume 65, Proceedings of the 2021 Denver X-ray Conference